TECHNISCHE UNIVERSITÄT MÜNCHEN

Lehrstuhl für Radiochemie

Q-value effects in the synthesis of superheavy elements

Reimar Graeger

Vollständiger Abdruck der von der Fakultät für Chemie
der Technischen Universität München zur Erlangung des akademischen Grades eines

Doktors der Naturwissenschaften (Dr. rer. nat.)

genehmigten Dissertation.

Vorsitzender:	Univ.-Prof. Dr. K. Köhler
Prüfer der Dissertation:	
	1. Univ.-Prof. Dr. A. Türler
	2. Univ.-Prof. Dr. R. Krücken
	3. Priv.-Doz. Dr. A. Yakushev

Die Dissertation wurde am 14.06.2010 bei der Technischen Universität München eingereicht und durch die Fakultät für Chemie am 02.07.2010 angenommen.

Abstract

Superheavy elements (Z$\gtrsim$104) only exist due to nuclear shell effects, which stabilize them against spontaneous fission (SF). Theoretical calculations predict these shell stabilization effects to reach a maximum at the closures of the next spherical proton and neutron shells, which are anticipated in the region between Z=114 and Z=126 and at N=184. More recent calculations, that also consider deformed nuclear shapes extended this picture and predicted deformed shell closures at Z=108 and at N=162, creating a region of enhanced stability around ^{270}Hs, confirmed in recent Hs chemistry experiments by measuring the decay of ^{270}Hs for the first time.

Recently, the formation of deformed doubly-magic ^{270}Hs in the $4n$ evaporation channel in the fusion reactions ^{248}Cm(^{26}Mg, $4n$), ^{244}Pu(^{30}Si, $4n$), ^{238}U(^{36}S, $4n$), and ^{226}Ra(^{48}Ca, $4n$) was studied theoretically using a two-parameter Smoluchowski equation. Simple entrance channel arguments make compound nucleus (CN) formation appear favorable for systems with larger mass asymmetry. However, due to a lower reaction Q value, the reactions ^{238}U(^{36}S, $4n$)^{270}Hs and ^{226}Ra(^{48}Ca, $4n$)^{270}Hs are predicted to have higher cross sections compared to the reactions ^{248}Cm(^{26}Mg, $4n$)^{270}Hs and ^{244}Pu(^{30}Si, $4n$)^{270}Hs.

The aim of the research done in the framework of this thesis was to study the influence of the reaction (B-Q)-value on the yield of SHE produced in nuclear fusion reactions. Therefore the most promising reactions ^{36}S+^{238}U and ^{48}Ca+^{226}Ra have been investigated and compared with the already measured reaction ^{26}Mg+^{248}Cm. The reaction ^{36}S+^{238}U was investigated at two beam energies. One correlated decay chain attributed to ^{270}Hs was found at E*=51 MeV resulting in a cross section of $0.8^{+2.6}_{-0.7}$ pb. The reaction ^{48}Ca + ^{226}Ra was investigated at three beam energies. Six correlated decay chains attributed to ^{270}Hs were detected at E*=40 MeV corresponding to a cross section of $8.3^{+6.7}_{-3.7}$ pb.

Since all reactions result in the same CN (^{274}Hs), the exit channel is nearly identical for them at the same excitation energy and could not explain possible differences in cross sections. Hence, the entrance channel and in particular the fusion probability, depending on the (B-Q)-value and the reaction asymmetry have a major impact on the production cross section. For intermediate energies (E*≈40 MeV) the fusion probability is mainly influenced by the (B-Q)-value and therefore the reaction ^{48}Ca + ^{226}Ra, whose fusion probability is already saturated for such energies in contrast to both other reactions provides largest measured $4n$ cross sections. At high excitation (E*≈50 MeV) the fusion probability of all three reactions is saturated and hence the most asymmetric reaction ^{26}Mg + ^{248}Cm with the largest saturation level provides largest production cross section. The slightly better (B-Q)-value of the reaction ^{36}S + ^{238}U compared with ^{26}Mg + ^{248}Cm is not affecting the cross section at all, in contrast to theoretical calculations.

Zusammenfassung

Superschwere Elemente ($Z \geq 104$) existieren nur durch Kernschaleneffekte, welche sie gegen Spontanspaltung stabilisieren. Theoretische Berechnungen sagen ein Maximum diese Stabilisierungseffekte für die nächste geschlossenen Protonen- und Neutronenschale voraus, welche in der Region zwischen Z=114 und Z=126 und für N=184 angenommen wird. Aktuellere Berechnungen, welche auch Kerndeformationen berücksichtigen erweitern dieses Bild und sagen deformierte Schalenabschlüsse für Z=108 und N=162 voraus. Um ^{270}Hs bildet sich somit eine Region erhöhter Stabilität, was kürzlich in Hs Chemieexperimenten durch die erstmalige Messung des Zerfalls von ^{270}Hs nachgewiesen wurde.

Kürzlich wurde die Bildung des deformierten doppelt magischen ^{270}Hs im $4n$ Kanal der Fusionreaktionen ^{248}Cm(^{26}Mg, $4n$), ^{244}Pu(^{30}Si, $4n$), ^{238}U(^{36}S, $4n$), und ^{226}Ra(^{48}Ca, $4n$) theoretisch mithilfe einer zwei-Parameter Smoluchowskigleichung studiert. Einfache Eingangskanalargumente bevorzugen die CN Bildung für Systeme grosser Massenasymmetrie. Aufgrund niedriger Reaktions-Q-Werte, sollen die Reaktionen $^{238}\mathrm{U}(^{36}\mathrm{S}, 4n)^{270}\mathrm{Hs}$ und $^{226}\mathrm{Ra}(^{48}\mathrm{Ca}, 4n)^{270}\mathrm{Hs}$ höhere Wirkunsquerschnitte im Vergleich zu den Reaktionen $^{248}\mathrm{Cm}(^{26}\mathrm{Mg}, 4n)^{270}\mathrm{Hs}$ und $^{244}\mathrm{Pu}(^{30}\mathrm{Si}, 4n)^{270}\mathrm{Hs}$ aufweisen.

Das Ziel der Forschung im Rahmen dieser Dissertation war das Studium des Einflusses des Reaktions (B-Q)-Werts auf den Ertrag an SHE in Fusionsreaktionen. Es wurden die erfolgversprechendsten Reaktionen $^{36}\mathrm{S} + {}^{238}\mathrm{U}$ und $^{48}\mathrm{Ca} + {}^{226}\mathrm{Ra}$ untersucht und mit der schon gemessenen Reaktion $^{26}\mathrm{Mg} + {}^{248}\mathrm{Cm}$ verglichen. Die Reaktion $^{36}\mathrm{S} + {}^{238}\mathrm{U}$ wurde bei zwei Strahlenergien untersucht. Eine Zerfallskette von ^{270}Hs wurde gefunden bei E*=51 MeV, womit sich ein Wirkungsquerschnitt von $0.8^{+2.6}_{-0.7}$ pb ergab. Die Reaktion $^{48}\mathrm{Ca} + {}^{226}\mathrm{Ra}$ wurde bei drei Strahlenergien untersucht. Sechs Zerfallsketten von ^{270}Hs wurden gefunden bei E*=40 MeV. Der Wirkungsquerschnitt beträgt $8.3^{+6.7}_{-3.7}$ pb.

Alle Reaktionen ergeben denselben CN (^{274}Hs), der Ausgangkanal ist somit fast identisch bei gleichen Anregungsenergien und erklärt keine Querschnitteunterschiede. Daher hat der Eingangskanal und besonders die Fusionswahrscheinlichkeit, abhängig vom (B-Q)-Wert den grössten Einfluss auf den Produktionsquerschnitt. Bei mittleren Energien (E*≈40 MeV) ist die Fusionswahrscheinlichkeit hauptsächlich vom (B-Q)-Wert abhängig, daher hat die Reaktion $^{48}\mathrm{Ca}+{}^{226}\mathrm{Ra}$ den höchsten gemessenen $4n$ Querschnitt, da die Fusionswahrscheinlichkeit bei solchen Energien bereits gesättigt ist, im Gegensatz zu den anderen beiden Reaktionen. Bei höheren Anregungsenergien (E*≈50 MeV) ist die Fusionswahrscheinlichkeit von allen drei Reaktionen gesättigt, daher weist die asymmetrischte Reaktion $^{26}\mathrm{Mg} + {}^{248}\mathrm{Cm}$ den grössten Querschnitt auf. Der wenig günstigere (B-Q)-Wert der Reaktion $^{36}\mathrm{S} + {}^{238}\mathrm{U}$ verglichen mit $^{26}\mathrm{Mg} + {}^{248}\mathrm{Cm}$ beeinflusst den Querschnitt nicht, im Gegensatz zu theoretischen Berechnungen.

Acknowledgements

This thesis was conducted in the frame of research at the Institut für Radiochemie at the Technische Univerversität München from March 2007 until April 2010 under the kind guidance of Prof. Dr. A. Türler and PD Dr. A. Yakushev.

It is a pleasure to thank those who made this thesis possible. This thesis would not have been possible without the support, hard work, and endless efforts of a large number of persons. I want to thank all of you, my colleagues, my friends, and my family, who helped and inspired me during my conferral of a doctorate.

In the first place, I owe my deepest and sincerest gratitude to my mentor, PD Dr. A. Yakushev. I would like to record my thankfulness to him for his neverending effort, advice, and guidance from the very early stage of this research as well as giving me extraordinary experiences through out the work. During the last three years and the plenty time we spent at experiments, conferences, or invitations of his wife and him, I became acquainted with him. He has an admirable personality which I am very appreciative of, always honest, helpful, loyal, and sacrificially careing. Above all, he provided me unflinching encouragement, always ready to help, patiently answering my rudimentary questions, supporting me in every possible way. His truly scientist intuition has made him as a constant oasis of ideas and passions in science. He taught me everything I know about the "superheavies", sharing a small part of his huge knowledge to me. I am indebted to him more than he knows.

I gratefully acknowledge Prof. Dr. A Türler for his confidence he has placed in me and allowing me to participate such an important and exciting research field. To work with him during the last three years was always enlightened. His firm support helped me with any problem I was confronted. I deeply appreciate his kind cordiality, which allowes us to enjoy many interesting friendly discussions. One could not wish for a better and friendlier supervisor.

Many thanks go to the group Kernchemie at GSI, where we spend so much time on our experiments. All members of the group were very helpful and working very professionally. Because of the friendly atmosphere in the group, we spent extraordinary pleasant times during our experiments. In particular, I would like to acknowledge Dr. M. Schädel, who always granted me his time even for answering some of my questions, Dr. Ch. Düllmann, who helped me with many problems and found always time to support me, Dipl.-Ing. E. Jäger, who has particular skills in handling delicate equipments, J. Krier and E. Schimpf, who can construct them, Dr. A. Semchenkov, who could answer lots of my questions, and B. Schausten, the good soul of the group.

For their help and support beside the group Kernchemie, concerning the TUM Hs chemistry experiment, I want to thank first of all J. Dvorak from LBNL, who has helped so much with the experimental setup; M. Chelnokov, V. Chepigin, A. Kuznetsov and O. Petrushkin from FLNR; J. Even, D. Hild, J. V. Kratz and J. Runke from Universität Mainz; D. Ackermann, F. P. Hes̈sberger and J. Khuyagbaatar from the SHIP group at GSI; J. P. Omtvedt and F. Samadani from Oslo university; K. Nishio from JAEA; Q. Zhi from IMP; D. Rudolph from Lund university; H. Nitsche from LBNL and A. Hübner, B. Kindler, B. Lommel from GSI target laboratory.

Many thanks go to the group of the DGFRS at FLNR in Dubna, Russia, who invited us two times for an experiment, which was a main part of this thesis. In particular, I would like to acknowledge Prof. Dr. Yu. Oganessian, member of RAS, who gave me the chance to participate these exciting experiments and Dr. V. Utyonkov, who supported and helped me in so many ways during the experiment but also in the time after. I am indepted to him and I really enjoyed the work with him. But also I want to thank all others of the DGFRS group, F. Abdullin, A. Poliakov, R. Sagaidak, I. Shirokovski, Y. Tsyganov, A. Voinov and V. Krashonkin.

I benefited from an extraordinary team of coworkers, which I had an opportunity to meet every day at Institut für Radiochemie. I am grateful for giving me such a pleasant time when working together. It will be difficult to ever find again a group of people, which posses not only high professional skills, but which are at the same time so caring, so human. I deeply appreciate the conditions, which they prepared for my research. Many thanks goes to members of our small group of superheavy elements, in particular to A. Gorshkov, who helped me to make things clear and who was a great friend. Most time I spend with my collegues Ch. Barkhausen, A. Klaschwitz, F. Ried, S. Lehenberger and B. Rohrmoser. I had a great time with these fantastic collegues, who became real good friends. I appreciate the openness of all scientific coworkers at the RCM, which shared with me the beauty of radiochemistry, showed me its broadness and usefulness. I would like to thank for extensive support from our workshop, because without their fast and yet precise work no experiments would be possible. I acknowledge I. Kaul for her help with administrative tasks. I owe my gratitude to the members of the group of radiation safety, who helped us every time with all our concerns in a very friendly manner.

I would like to thank the staff and crew of the GSI UNILAC for providing stable and intense ^{36}S beams. This project was supported by BMBF Projects No. 06MP247I and 06MZ223I.

Finally I deeply acknowledge my family and in particular, my father, my mother and my sister, who helped and supported me over the years so much. I am so grateful to them, more than they know.

Reimar Graeger

Contents

Chapter 1

Introduction

1.1 Motivation

1.1.1 History of the synthesis of heaviest elements

Since the birth of civilization a great dream of mankind was to change and manipulate arbitrarily the matter surrounding us. As an example I would like to mention the desire of the ancient alchemists to turn lead to gold. Without knowing and understanding the fundamentals of nature, these ambitions were of course not successful.

Nowadays we know that all molecules are composed of atoms. In the latter, the negatively charged electron shells surround the positively charged nucleus consisting of electrically neutral neutrons and positively charged protons. Beside the attractive nuclear force binding the nucleons inside of the nucleus, the electrostatic force between the protons acts repulsive, reducing the binding energy of the nucleons. After reaching the maximum binding energy in the iron/nickel region of the nuclear chart, this repulsion is destabilizing the nucleus successively with increasing proton number until an end of stability is reached in the lead region (Z=82). Similar to the electron shells in atoms, closed nucleon shells with magic numbers of protons or neutrons in nuclei bring additional stabilization. Nuclei with larger proton numbers as lead decay towards the lead region, increasing their stability due to shell stabilizations.
The heaviest nuclei found in nature in weighable quantities are the primordial, quasistable uranium and thorium isotopes ^{238}U, ^{235}U, and ^{232}Th synthesized in supernova explosions billions of years ago and their decay products. These isotopes only exist to-

day because of their very long half-lives comparable with the age of the earth. Heavier nuclei can only be synthesized artificially using nuclear reactions. Below an overview about the exciting history of their synthesis based on [1] is presented.

The starting point of the synthesis of heavier elements than uranium was the production of ^{239}Np via neutron capture of ^{238}U followed by a β^- - decay:

$$
\begin{aligned}
{}^{238}_{92}\mathrm{U} + {}^{1}_{0}\mathrm{n} &\rightarrow {}^{239}_{92}\mathrm{U} + \gamma \\
{}^{239}_{92}\mathrm{U} &\xrightarrow[\mathrm{t}_{1/2}=23.5\ \mathrm{min}]{\beta^-} {}^{239}_{93}\mathrm{Np}
\end{aligned}
$$

This experiment was performed by E. M. McMillan *et al.* in 1939/1940 at the University of California at Berkeley. This type of reaction corresponds to the astrophysical s-process (slow-process) due to the orders of magnitude lower neutron flux, which can be achieved on earth, with respect to the r-process (rapid-process). However, a limit of this technique is reached, if the neutron absorption is in equilibrium with the decay of the reaction products, which just means, that even heavier elements cannot be synthesized due to the immediate decay of the mother nucleus.

For the separation or isolation of the new element, chemical techniques have been used, separating the target material from the sample and measuring the half-life of the remaining activity. The same technique was also used for all experiments, up to the synthesis of element 100.

In the year 1940, another synthesis technique was introduced to produce even heavier elements, the nuclear fusion reaction. Instead of successive neutron absorption followed by β^- - decay, the desired nuclei is directly produced by the nuclear fusion reaction of two lighter nuclei, a so called target nucleus which is bombarded by a so called projectile nucleus. Due to the electrostatic repulsion originating from the presence of the positively charged protons, a sufficiently high projectile energy is necessary to overcome the barrier, which is the case when the repulsive Coulomb force is in equilibrium with the attractive nuclear force. This type of nuclear reaction was applied for the first time to produce plutonium (^{238}Pu) by the bombardment of ^{238}U with ^{2}H followed by two neutron emission and a β^- - decay with a half-life of 2.12 days:

$$
\begin{aligned}
{}^{238}_{92}\mathrm{U} + {}^{2}_{1}\mathrm{H} &\rightarrow {}^{238}_{93}\mathrm{Np} + 2{}^{1}_{0}\mathrm{n} \\
{}^{238}_{93}\mathrm{Np} &\xrightarrow[\mathrm{t}_{1/2}=2.12\ \mathrm{days}]{\beta^-} {}^{238}_{94}\mathrm{Pu}
\end{aligned}
$$

This experiment was performed by G. T. Seaborg *et al.* using the 60-inch cyclotron at Berkeley University to accelerate the deuterons.

During 1941, ^{239}Pu was identified for the first time after β^- - decay of ^{239}Np. When the potential of ^{239}Pu as a source of nuclear energy and hence its application in nuclear weapons was realized, the possibility of producing large quantities of that isotope was studied after the first experiments. This was performed in 1941 using neutrons from the bombardment of a beryllium target by deuterons delivered by the 60-inch cyclotron. During a two day bombardment, 0.5 μg of ^{239}Pu have been produced, used to demonstrate, that the probability of fission induced by thermal neutrons is about 50% larger than that for ^{235}U.

Due to the fact, that the aforementioned technique is only able to produce minor quantities, other approaches were searched leading to the breeding of ^{239}Pu in nuclear reactors, like the U.S. plant at Savannah river. With these facilities it was possible to gain macroscopic amounts of material, enough to build nuclear weapons.

Later during the war, a few experiments were conducted to produce even heavier elements by neutron absorption of ^{239}Pu, but without success, due to the limited instrumentation.

However in summer 1944, the new elements americium and curium were synthesized for the first time. $^{241}_{95}$Am was produced by two neutron absorption of ^{239}Pu followed by a β^- - decay:

$$^{239}_{94}\mathrm{Pu} + {}^{1}_{0}\mathrm{n} \rightarrow {}^{240}_{94}\mathrm{Pu} + \gamma$$
$$^{240}_{94}\mathrm{Pu} + {}^{1}_{0}\mathrm{n} \rightarrow {}^{241}_{94}\mathrm{Pu} + \gamma$$
$$^{241}_{94}\mathrm{Pu} \xrightarrow[\mathrm{t_{1/2}=14.4\ years}]{\beta^-} {}^{241}_{95}\mathrm{Am}$$

$^{242}_{96}$Cm was produced by the nuclear fusion of ^{239}Pu and ^{4}He delivered by the 60-inch cyclotron.

$$^{239}_{94}\mathrm{Pu} + {}^{4}_{2}\mathrm{He} \rightarrow {}^{242}_{96}\mathrm{Cm} + {}^{1}_{0}\mathrm{n}$$

Another way of producing $^{242}_{96}$Cm was the further neutron absorption of $^{241}_{95}$Am:

$$^{241}_{95}\mathrm{Am} + {}^{1}_{0}\mathrm{n} \rightarrow {}^{242}_{95}\mathrm{Am} + \gamma$$
$$^{242}_{95}\mathrm{Am} \xrightarrow[\mathrm{t_{1/2}=16.0\ hours}]{\beta-} {}^{242}_{96}\mathrm{Cm}$$

Due to very similar chemical properties of americium and curium, these elements could only be separated chemically in fall of 1945 and fall of 1947, respectively.

The next step in the direction of producing even heavier elements was the synthesis of the elements 97 and 98, berkelium and californium, respectively. The only available tools at that time were the aforementioned neutron and helium bombardment of the target material. Hence, it was necessary to produce a sufficient amount of Am and Cm target material, at least a few mg. After the successful production of enough $^{241}_{95}$Am in a high-flux reactor, element 97 was synthesized by Thompson, Ghiorso, and Seaborg in December 1949 for the first time by the bombardment of $^{241}_{95}$Am with 35 MeV helium ions delivered by the 60 inch cyclotron:

$$^{241}_{95}\mathrm{Am} + {}^{4}_{2}\mathrm{He} \rightarrow {}^{243}_{97}\mathrm{Bk} + 2\,{}^{1}_{0}\mathrm{n}$$

Californium, element 98, was produced the first time in spring 1950 by Street, Ghiorso, and Seaborg in Berkeley, using a similar production reaction and chemical separation and detection concepts:

$$^{242}_{96}\mathrm{Cm} + {}^{4}_{2}\mathrm{He} \rightarrow {}^{245}_{98}\mathrm{Cf} + {}^{1}_{0}\mathrm{n}$$

The next two elements, einsteinium and fermium were unexpectedly discovered in the debris from the first thermonuclear explosion in the Pacific, by airplanes equipped with filters, flying after the explosion through the cloud and collecting the activity.

During the evaluation of the sample, new very neutron rich uranium and plutonium isotopes up to ^{246}Pu were found leading to the conclusion, that the ^{238}U from the bomb was exposed to an integrated neutron flux of $1 \cdot 10^{24}$ to $4 \cdot 10^{24}$ neutrons, being provided in a few nanoseconds. Beside this, also at that time unknown activities have been found in the sample, identified as the new elements 99 and 100, einsteinium and fermium, respectively, produced via successive neutron capture and β^{-}-decay. This was actually a simulation of the r-process.

With element 100, the ending point of heaviest element synthesis by successive neutron capture was reached due to the decreasing half-life with increasing atomic number and the limited neutron flux which could be reached even by high-flux reactors. It was also speculated that heavier elements could not be synthesized due to a region of beta-delayed fission, that would prevent multiple beta decays from reaching elements with higher atomic number.

From element 101, mendelevium, on, all new elements have been synthesized by nuclear fusion evaporation reactions. Apart from that, also new separation and detection techniques have been introduced because of the very low production yield, demanding highly efficient methods, dealing with only one atom at a time.

One of the new techniques was the recoil method, which is used until today as a standard approach for the production of superheavy elements (SHE). It is characterized by depositing the target material on a foil and bombarding it with the projectiles. The fusion evaporation products are recoiling out of the rear side of the target, due to the momentum of the projectiles. These recoils are caught by a foil, which is removed after a certain time and analyzed or transported with a gas/aerosol jet to a separation and detection unit.

In 1955, mendelevium was synthesized and its decay detected for the first time using the following fusion evaporation reaction:

$$^{253}_{99}\mathrm{Es} + ^{4}_{2}\mathrm{He} \rightarrow ^{256}_{101}\mathrm{Md} + ^{1}_{0}\mathrm{n}$$

The experiment was performed again at the Berkeley 60-inch cyclotron. The identification of element 101 was a little bit more complicated than for previous new elements, due to the decay properties of the isotope $^{256}_{101}\mathrm{Md}$ by electron capture followed by spontaneous fission of the daughter nuclide $^{256}_{100}\mathrm{Fm}$. But because of the high quality of the chemical separation, mendelevium could be unambiguously identified.

In 1958, element 102, nobelium, was also produced by a fusion evaporation reaction using the first time projectiles heavier than He, $^{12}\mathrm{C}$ in this case. This was necessary, because fusion reactions dealing with helium projectiles to produce nobelium would need fermium targets, which cannot be made due to the short half-life of fermium. The carbon ions were delivered using the new Berkeley Heavy Ion Linear Accelerator (HILAC). In this experiment, only the daughter nuclide of Nobelium could be identified due to the short half life of the mother:

$$^{244}_{96}\mathrm{Cm} + ^{12}_{6}\mathrm{C} \rightarrow ^{252}_{102}\mathrm{No} + 4^{1}_{0}\mathrm{n}$$
$$^{252}_{102}\mathrm{No} \xrightarrow[\mathrm{t}_{1/2}\sim 3\ \mathrm{s}]{\alpha} ^{250}_{100}\mathrm{Fm}$$

Parallel to the Berkeley group, G. N. Flerov *et al.* of the Dubna group, could clearly identify an alpha-decaying nobelium isotope ($^{252}\mathrm{No}$) produced in the complete fusion reaction of $^{239}\mathrm{Pu}$ with $^{16}\mathrm{O}$ ions.

The next discovered element was element 103, lawrencium, which was produced by the bombardment of a californium target which consisted of a mixture of the isotopes $^{249}_{98}\mathrm{Cf}$ to $^{252}_{98}\mathrm{Cf}$ with heavy ion beams of $^{10}_{5}\mathrm{B}$ and $^{11}_{5}\mathrm{B}$, again at the HILAC in Berkeley.

With the first synthesis of element 103, all actinide elements were explored. The next step to even heavier nuclei led to the group of transactinide elements, the so-called superheavy elements, starting from element 104. Due to the decreasing half-lives of the nuclei with increasing proton numbers, which are down to the range of seconds for the heaviest actinide elements, offline chemical separation techniques could not be applied anymore. This problem could be overcome by the development of chemical online separation methods, which was attempted for the confirmation of element 104, rutherfordium, produced in the hot fusion reaction:

$$^{22}_{10}\mathrm{Ne} + {}^{242}_{94}\mathrm{Pu} \rightarrow {}^{259}_{104}\mathrm{Rf} + 5{}^{1}_{0}\mathrm{n}$$

Meanwhile the Berkeley group established pure physical identification techniques, by measuring the decay of the produced nuclei in detail, to establish a link to already known elements. The first successful application of this method was done during the synthesis of element 106, seaborgium, by using the hot fusion reaction:

$$^{18}_{6}\mathrm{O} + {}^{249}_{98}\mathrm{Cf} \rightarrow {}^{263}_{106}\mathrm{Sg} + 4{}^{1}_{0}\mathrm{n}$$

The produced evaporation residues (EVR), recoiling from the target were caught by NaCl aerosol clusters and transported by a capillary to the Vertical Wheel, where they were deposited on. After a certain time, the wheel moved into the next position. During the collection and the next 7 steps, the α particles, emitted from the sample were measured using silicon detectors, during the collection from one side and during the next steps from both sides, to identify correlated decay chains. In addition, a so called daughter mode existed, waiting for the decay of the grand daughter.

Since the nuclear fusion reactions, which have been used to produce elements up to seaborgium, were all hot fusion reactions, the excitation energies of the compound nuclei (CN) were quite high (usually 40-50 MeV) corresponding to projectile energies as high as to overcome the Coulomb barrier. This affects the effective yield of the surviving evaporation residues, due to the competition of neutron evaporation and fission during each of the 4-5 neutron evaporation steps. These are necessary to cool down the highly excited CN to the ground state.

A different approach has been proposed by Yuri Oganessian in from Dubna, the so called cold fusion. A cold fusion reaction is characterized by a small excitation energy (10-20 MeV) of the CN, close to the Coulomb barrier. This is caused by the nuclear structure of the target nuclei. The typical cold fusion targets are lead ($^{208}_{82}$Pb) and bismuth ($^{209}_{93}$Bi) with $^{208}_{82}$Pb having closed proton and neutron shells and $^{209}_{93}$Bi having the same configuration plus one proton.

Due to these closed shells, the binding energy of these nuclei is very high resulting in a very low Q-value, which causes the low excitation energy at near-barrier energies and so the emission of one or two neutrons is sufficient to de-excite the CN:

$$^{\mathrm{A}}_{\mathrm{Z}}\mathrm{X} + {}^{208}_{92}\mathrm{Pb} \rightarrow {}^{208+\mathrm{A}}_{82+\mathrm{Z}}\mathrm{N} + 1^{1}_{0}\mathrm{n}$$
$$Q = E_N + E_n - E_{Pb} - E_X$$

On the other side, due to an increased symmetry of cold fusion reaction, capture cross section and compound nucleus formation probability are decreased. However, the reduced capture cross section and compound nucleus formation probability due to the increased symmetry is overcompensated by the increased survival probability. Hence, losses due to fission during the de-excitation process is significantly reduced.

Because of the higher symmetry of cold fusion reactions, compared with hot fusion reactions, the produced evaporation residues are more neutron-deficient than those produced in hot fusion reactions. Due to the relatively high ratio of proton number and neutron number, these nuclei decay predominantly by alpha decay with rather short half-lives. In 1973 this reaction type has been first successfully used in Dubna to produce fermium in the cold fusion reaction $^{40}_{18}$Ar+$^{208}_{82}$Pb. In the next years several attempts have been made to produce the superheavy elements 104, 105, 106, 107, 108, 109, 110, 111, and 112 in cold fusion reactions, using $^{50}_{22}$Ti-, $^{54}_{24}$Cr-, $^{58}_{26}$Fe-, $^{62}_{28}$Ni and $^{70}_{30}$Zn-beams with $^{209}_{83}$Bi- or $^{208}_{82}$Pb-targets. The remarkable point with these combinations is the fact, that nearly all these projectiles differ by one α-particle, hence all products of these reactions, produced in 1n channel should have the same decay properties from element 105 on and result in the long living isotope $^{246}_{98}$Cf with a half-life of 35.4h and an α-energy of 6.75 MeV.

Because of the short half-lives of cold fusion products, it is necessary to use a pure physical detection system for the unambiguous identification and confirmation of these fusion evaporation products.

This approach of using cold fusion reactions in combination with a highly sensitive and efficient physical separation and detection system has been used very successfully by the SHIP-group at the GSI in Darmstadt. The main challenge at that point was to deal with the dramatic decrease of cross sections with increasing proton number of the fusion product. While ^{254}No can be produced with a cross section of 2 μb using the cold fusion reaction ^{48}Ca + ^{208}Pb, the cross section to produce ^{261}Sg, which contains just four protons more, in the reaction ^{54}Cr + ^{208}Pb decreases down to about 2 nb, which corresponds to 3 orders of magnitude! With a simple linear interpolation, it can be seen, that the cross section to produce even heavier elements will be of the order of several pb or even fb!

Due to the very high cross sections of transfer- and deeply inelastic reactions, which are of the order of mb or several tens to hundreds of μb, compared with the aforementioned evaporation residue cross sections and due to the successive decrease of half-lives with increasing proton number, a very fast and efficient separation technique is required in order to go further with the exploration of the heaviest elements.

One possible option to reach these goals is the use of separators, gas-filled or kinematic separators. In the beginning of the seventies, the group of Sigurd Hofmann installed the velocity separator SHIP (Separator for Heavy Ion reaction Products) at the GSI, which was completed and first tested in 1975. The basic concept of SHIP is that of a double Wien filter, named after the physicist Wilhelm Wien, separating the different nuclei with static magnetic and electric dipole fields due to their different velocities.

1.1.2 History of the investigation of the doubly magic nucleus ^{270}Hs and perspectives for SHE synthesis

Superheavy elements with proton numbers Z$\gtrsim$104 exist only due to nuclear shell effects, which stabilize them against spontaneous fission (SF). Theoretical calculations predict these shell stabilization effects to reach a maximum at the closures of the next spherical proton and neutron shells, which are anticipated in the region between Z=114 and Z=126 and at N=184 [2,3,4,5]. These effects were long thought to give rise to a so-called "island of stability" in the midst of a sea of nuclear instability, far away from any nuclei found in nature. More recent calculations based on the macroscopic-microscopic model as well as self-consistent mean-field calculations that also consider deformed nuclear shapes extended this picture and predicted deformed shell closures at Z=108 and at N=162 [6], creating a region of enhanced stability halfway between the heaviest nuclides found on earth and the predicted island of stability.

In 2003 the new director of the Institut für Radiochemie (TU München) Andreas Türler founded a new group for superheavy element research with Alexander Yakushev as group leader and leading scientist. The first point of major interest was the exploration of neutron rich Hs isotopes near the predicted neutron shell closure N=162 and to verify the theoretical calculations, which predicted an enhanced stability of nuclei in the region Z=108 and N=162. Hence, a precise and detailed investigation of the decay properties

of ^{270}Hs was necessary.
This was done by studying the decay properties of the nuclides ^{269,270,271}Hs and their daughters formed in complete nuclear fusion reactions using an improved chemical separation and detection system. In former experiments, it has been proven, that Hs chemistry is very pure and effective [7]. An overall efficiency of around 55% for the separation and detection of ^{269}Hs was reached, which is for hot fusion reactions much larger than the values of any other separation technique, like that of kinematic separators.
In two experimental campaigns in 2004 and 2005 the excitation function of the complete nuclear fusion reaction $^{248}\mathrm{Cm}(^{26}\mathrm{Mg}, xn)^{274-\mathrm{x}}\mathrm{Hs}$ and its EVR decay properties have been investigated at 5 different beam energies [8]. In total 26 linked nuclear decay chains originating from Hs nuclei have been found. Based on 12 decay chains originating from ^{269}Hs, the decay properties of ^{269}Hs and its daughters were updated and their assignment reevaluated. All measured decay properties are summarized in table 1.2. In these experiments, the decays of ^{270}Hs and ^{271}Hs were measured for the first time.

The Q_α-values, deduced from the measured E_α-energies and their systematics in the framework of all known Hs isotopes and neighboring elements, verified the deformed shell closure at Z=108 and N=162.
The second major result of these experiments was the measurement of the excitation functions for the 3-5n evaporation channels. It is not very common to do so in superheavy element synthesis reactions dealing with cross sections of the order of picobarns.

1.2 Stability of SHE

The stability of a nucleus, or how tightly a nucleus is bound, depends on the binding energy of its constituents, the protons and neutrons, bound inside of the nuclear potential of the nucleus. The binding is caused by the short ranged attractive nuclear force between the nucleons. Beside this, the positively charged protons repel each other due to the Coulomb force, decreasing the binding energy. Due to this opposite effect, a certain proton-to-neutron ratio is favored providing the largest binding energy for a certain number of nucleons and hence the strongest bonding, making the nucleus stable against β-decay. Most of the β-stable nuclei have binding energies around 7-8 MeV per nucleon and an approximately constant density of 0.17 nucleons/fm^3 [9]. Only very light and very heavy nuclei differ significantly in their binding energies.
Besides β-decay, heavy nuclei decay also by α-particle emission or by spontaneous fission.

The half-life and, hence, the dominant decay mode depends on the increase of binding energy which is gained through the decay. In case of spontaneous fission, the half-life depends on the height of the fission barrier. Especially for superheavy elements all decay-modes are very important and partially dominant.

1.2.1 Liquid drop model

The liquid drop model (LDM) is a semi-classical model which describes the mass and binding energy of a nucleus and is based on the fact, that nuclei have approximately the same nuclear density and that the binding energy per nucleon is for most nuclei in the energy range of 7 to 8 MeV. It was developed in the 1930s after the measurement of a sufficient number of atomic masses. As the name implies this model is deduced by the picture of a water drop, due to the aforementioned experimental observations on which the model is based. The analogies between a nucleus and a water drop are the well-defined surface, the incompressibility, and the attractive short-range force binding the system.

Taking this model as a base, von Weizsäcker [10] developed and later on Bethe and Bacher [11] improved a semi-classical formula to calculate the nuclear binding energy and hence the mass of a given nucleus. It is called the Bethe-Weizsäcker-formula. The mass of a nucleus is equal to the sum of the masses of all constituents, N neutrons and Z protons reduced by the binding energy:

$$M(N,Z) = NM_n + ZM_p - E_B \tag{1.1}$$

E_B denotes the binding energy and is described in the frame of the Bethe-Weizsäcker-formular as:

$$E_B = a_v \cdot A - a_s \cdot A^{\frac{2}{3}} - a_c \cdot \frac{Z^2}{A^{\frac{1}{3}}} - a_a \cdot \frac{(A - 2 \cdot Z)^2}{A} + \delta(A,Z) \tag{1.2}$$

1. Volume term
   This term is proportional to the volume of the nucleus and hence to its number of nucleons. Due to the constant nuclear density, a maximum of the number of binding partners of each nucleon exists, resulting in a saturation of the binding energy per nucleon. Hence, the binding energy for the whole nucleus is proportional to the number of constituents and proportional to A.

2. Surface term

Not all nucleons are able to perform the maximal possible number of bondings to other nucleons. Especially nucleons at the surface of a nucleus have less binding partners, than they could have. The surface term, like all following terms, is a correction term of the volume term.

3. Coulomb term
   Due to the electrostatic repulsion of the protons inside of the nucleus the nucleus itself is less bound. Since the electro-magnetic force has infinite range in contrast to the nuclear force which has only a range of a few fm (the nuclear force decreases to negligibly small values for ranges of more than 2 fm), the size of a nucleus is limited. The Coulomb term takes this into account and considers the nucleus as a sphere of uniform charge density.

4. Asymmetry term
   The asymmetry term describes the fact, that a nucleus is most stable for a certain proton to neutron ratio. This is caused by the Pauli principle, which says that two fermions cannot occupy the same state. The implication is that one of these fermions has to occupy a state with a higher energy. Hence, an almost equal ratio of protons and neutrons is energetically preferred.

5. Pairing term
   The pairing term includes the fact, that two protons or two neutrons in the same state but with opposite spin are bound as a pair, providing more stability to the whole nucleus. As a consequence, this term results in a more strongly bound nucleus in the case of even numbers of protons and neutrons, compared with a nucleus with odd-proton number and even neutron number and vice versa. But this odd-even configuration is more strongly bound than a nucleus with odd proton and neutron numbers. This is due to the aforementioned fact, that an even-even nucleus has only paired nucleons, while an odd-even nucleus has one unpaired and an odd-odd nucleus has two unpaired nucleons, decreasing the binding energy. One implication of this systematics is the existence of only a few stable odd-odd nuclei in nature.

The masses and binding energies of nuclei are well reproduced by the Bethe-Weizsäcker-formular, which is based on the LDM. But at certain proton and neutron numbers (2, 8, 20, 28, 50, 82, 126), the experimental binding energies are larger than the predictions of the LDM and hence these nuclei are more strongly bound. These numbers are called magic numbers. Also, if we examine the proton and neutron separation energies, which define the energy which is necessary to remove the least bound proton or neutron, respectively, an increase can be measured at these magic numbers. These facts indicate a kind of nuclear shell structure, analog to the atomic shell structure of the electrons.

1.2.2 Nuclear shell model

The LDM itself is a phenomenological model which describes the nucleus as a whole and hence it is only able to describe the collective behavior of the nucleus. For characterizing the single particle behavior of protons and neutrons, bound inside of the nucleus, as well as collective properties near the magic numbers, a completely new model was developed. The magic numbers were first of all explained by Mayer [12, 13] who performed calculations on the energies of single particle spectra applying a square and a harmonic oscillator well potential. The resulting energy levels from the calculations with the harmonic-oscillator potential can be found in Figure 1.1 on the left side. Unfortunately, these calculations failed for higher magic numbers. Hence, Mayer [14] and independently Haxel, Jensen, and Suess [15] proposed that a strong spin-orbital interaction should be added. The model was called nuclear shell model due to some analogies to the atomic shell model. In this model, a non-central mean field potential is established by all nucleons, in which all nucleons are arranged. Bound states and orbitals are formed which can be occupied by a certain number of nucleons. Due to the Pauli principle the nucleons are moving in these orbitals without collisions.

The mean potential can be approximated by a square well, an harmonic-oscillator well potential, or an even more realistic Wood-Saxon potential including an angular moment dependence (ℓ^2 dependent term) and a strong spin-orbit-coupling ($\vec{l} \cdot \vec{s}$ dependent term). These two terms split the energy levels, calculated by solving the Hamiltonian of the mean potential, according to their angular momentum ($\vec{\ell}$) and to their total angular momentum ($\vec{j} = \vec{l} + \vec{s}$) as can be seen in Figure 1.1. This energy splitting increases with increasing angular momentum. With these two extensions, an excitation spectrum can be calculated, reproducing the experimentally observed shell closures, the magic numbers. A shell is defined as an energy range in the state space with a high density of states, followed on both, the high and low energy side by an energy range without any states. If such a shell is completely filled with nucleons, the next added nucleon has to be configured in a state in the next higher energetic shell. Due to the energy gap in between these shells, the last added nucleon is less bound than the other nucleons,

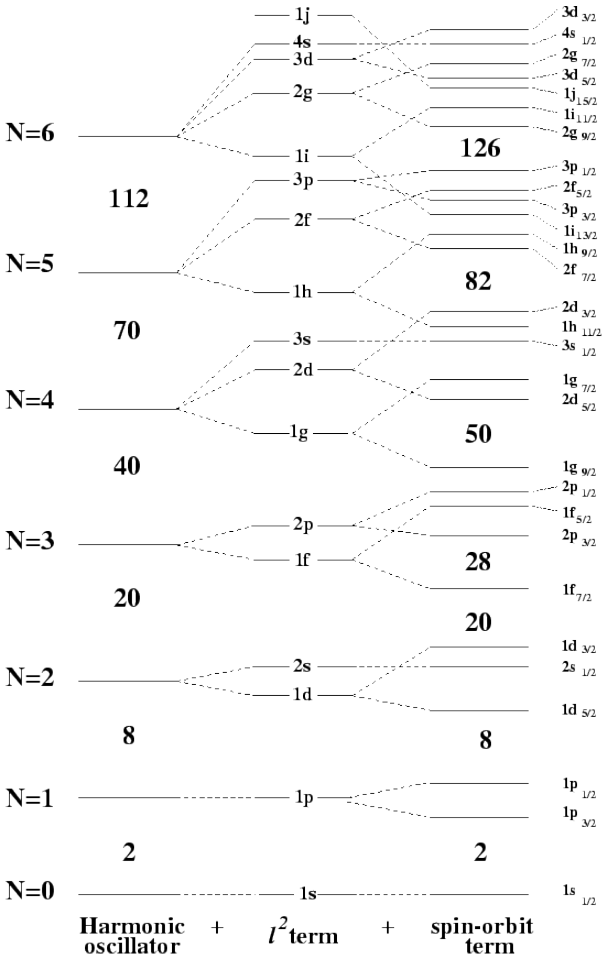

Figure 1.1: Energy levels according to the nuclear shell model.

reproducing the experimentally determined proton and neutron separation energies and therefore the shell structure of the nucleus.

The nuclear spin is calculated by summing up all individual spins of the nucleons. Because of the pairing energy, causing protons and neutrons to get bound in pairs with total spin equal to zero, due to the anti alignment of their spins, only unpaired nucleons contribute to the total nuclear spin. Hence, filled shells have no influence on the nuclear spin, the total angular momentum, and the parity of the nucleus. Nucleons outside of closed shells are so called valence nucleons.

It is worth to note, that nuclei with closed shells are not the most strongly bound nuclei, but compared with different nuclei around that nucleus on the nuclide chart, they are more strongly bound and thus more stable. Due to this fact, the shell structure plays an outstanding role in the stability of superheavy elements.

The shell model itself is only valid for spherical nuclei, hence nuclei near closed shells, due to the residual interaction of the nuclear force. Nuclei between closed shells get more and more deformed due to this residual interaction, which takes place mostly between the protons and the neutrons. To describe the single particle spectra of these nuclei, Nilsson published in 1955 an approach to deal with nucleons in strongly deformed nuclei. The deduced model is the so called Nilssons model. To take the deformation into account, he used a modified harmonic oscillator potential. Hence, the single particle orbital angular momentum and total angular momentum are no longer good quantum numbers in the Nilsson model. Instead, the projection of the total angular momentum onto the symmetry axis and the parity are good quantum numbers. A schematic diagram displaying the energy of single-particle states against the deformation of the nucleus, also called Nilsson diagram, is shown in Figure 1.2.

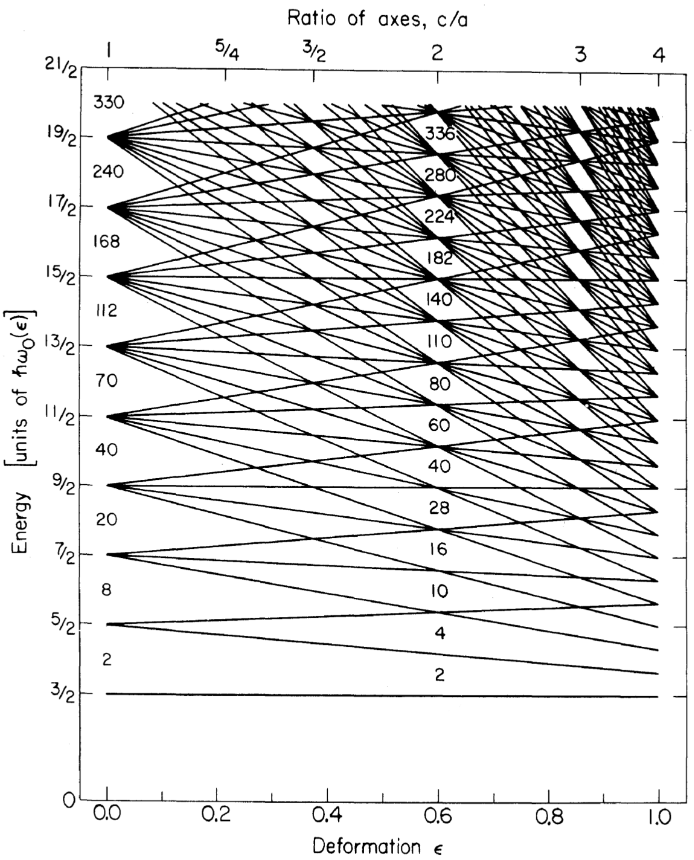

Figure 1.2: Energy levels of a harmonic-oscillator potential for prolate spheroidal deformations. The low density locations are present also at nonzero deformations, suggesting existence of stabilized deformed nuclei. Adapted from [16,17].

As can be seen, the shell closures, regions with small level density, are not only visible at zero-deformation and change with the deformation of the nucleus.

The Nilsson diagram of energy levels of the more realistic folded-Yukawa single-particle potential for nuclei heavier than lead can be found in Figure 1.3. At zero-deformation, the closed proton (Z=82) and neutron shell (N=126) of ^{208}Pb can be found in the lower energy part of that plot. The next closed spherical (zero-deformation) proton and neutron shell closures can be found at Z=114 and N=184. Other shell closures are located at nonzero deformation as for nuclei close to ^{270}Hs where gaps are revealed at Z=108 and N=162 implying enhanced stability of this deformed nucleus. Another deformed neutron shell closure can be found at N=152. A detailed introduction on the predictions for closed shells can be found in Section 1.4.

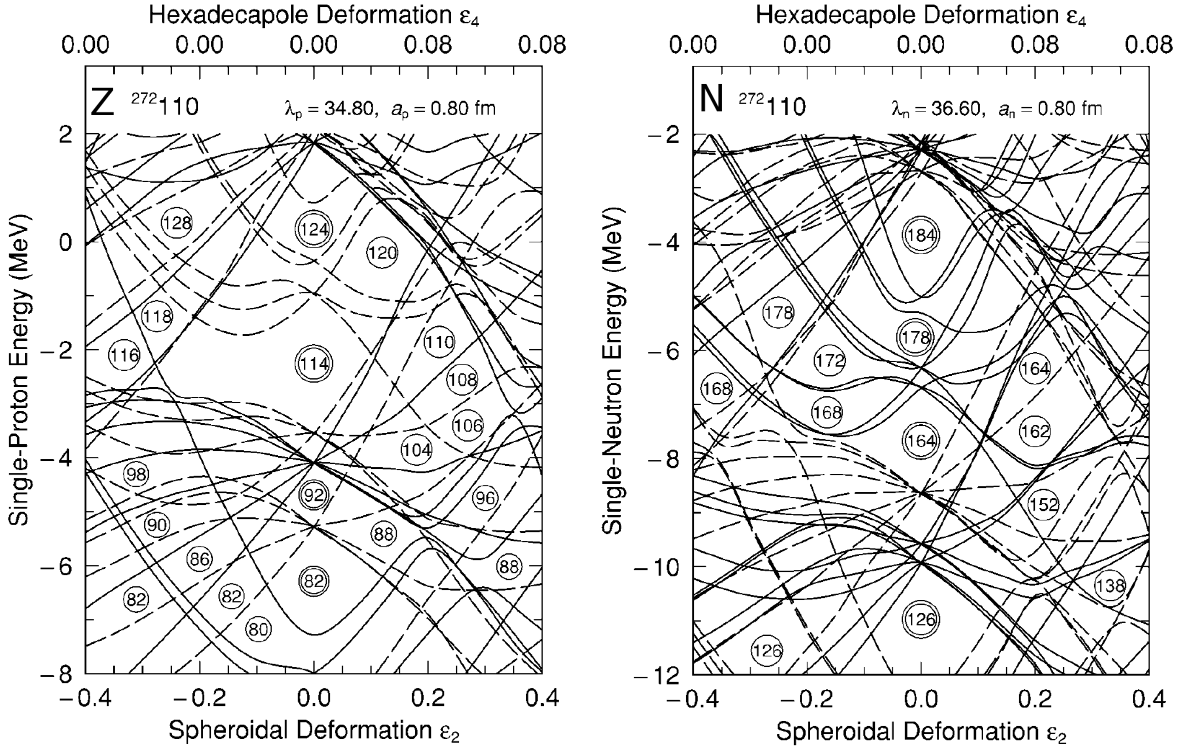

Figure 1.3: Proton and neutron folded-Yukawa single-particle level diagram for the nucleus ^{272}Ds plotted versus spheroidal and hexadecapole deformation. Gaps at $Z = 108$ and $N = 162$ suggest increased stability of deformed ^{270}Hs. Adapted from [18].

1.2.3 Strutinski method and the stability of SHE

While the LDM describes the collective properties of most nuclei quite well, it deviates relatively strongly for nuclei near closed shells. Hence, it is important for extrapolating global nuclear properties, like masses and binding energies, especially for superheavy elements, to introduce a correction to the LDM, which represents the shell structure. This method was introduced by Strutinski in 1967 [19, 20]. His approach is called a macroscopic-microscopic calculation. It divides the total energy of a nucleus in two parts, one macroscopic and one microscopic term. While the former is deduced from the LDM and represents the total energy of that nucleus in the semi-classical approach, the latter includes shell effects as well as a pairing correction to that energy:

$$E = \underbrace{E_{LDM}}_{Macroscopic} + \underbrace{\sum_{p,n}(\delta S + \delta P)}_{Microscopic} \tag{1.3}$$

Especially the shell correction energy is lowering the ground state energy and thus the ground state mass at and near closed shells by up to several MeV. Hence, the deviations of experimental and calculated masses disappear by introducing these corrections. These effects are absolutely essential for the properties and the synthesis of SHE. Calculating the barrier against spontaneous fission of a heavy nucleus with the LDM, results in nuclei with proton numbers higher than Z=100 having a half-life against spontaneous fission of less than one second. This happens due to the fact, that the fission barrier B_f decreases rapidly with increasing fissility parameter Z^2/A in the framework of the LDM of fission of heavy nuclei [21]. Taking also the shell corrections into account in the framework of the microscopic theory of the nucleus, closed proton and neutron shells increase the binding energy in nuclei beyond the limits defined by the LDM.

Ignoring the influence of the moment of inertia of the nucleus, its fission barrier is composed by the LDM fission barrier and the shell corrections. Fission barrier calculations [22] taking into account shell effects, predict also heavier than Z=102 systems to be bound due to an increase of the fission barrier, which has been proven experimentally during the last decades. Hence, the shell corrections term is the most dominant and solely responsible for the stability of SHE and their decay properties. Figure 1.4 illustrates shell effects in masses of transuranium nuclei, which are the difference between the experimental and within the LDM calculated mass values. The shell corrections are negative and decrease with increasing atomic number Z, down to about -5 MeV for the heaviest even-even nuclei (^{260}Sg and ^{264}Hs) included in that plot. In general, the shell corrections decrease the mass of a nucleus and hence enlarge the mass defect, and the binding energy.

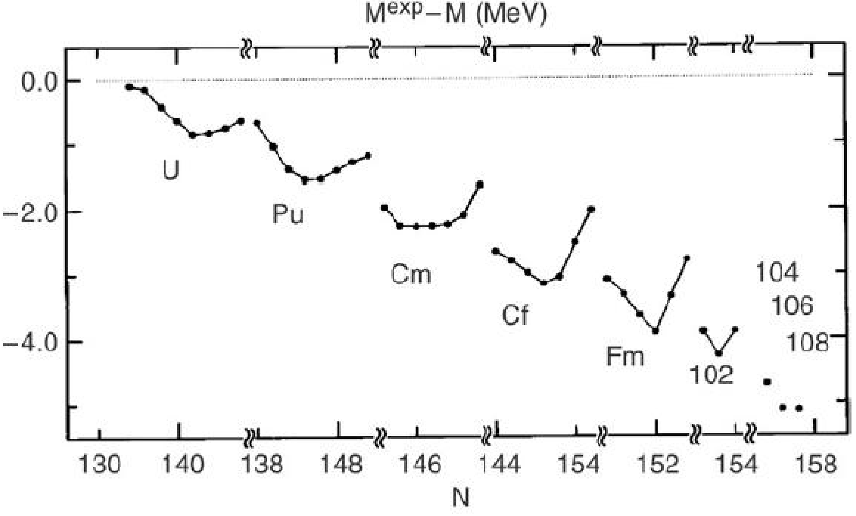

Figure 1.4: Shell effects in the masses of nuclei. Adopted from [22].

Examining the results for Cf, Fm, and No isotopes, the effect of the known deformed shell closure at neutron number N=152 can clearly be seen. Similarly clear and large shell effects on further properties of heaviest elements can be found in the α-decay energy- (Q_α) as well as in the α-decay half-life ($T_{1/2\alpha}$) or in fission barrier- (B_f) systematics. Exceptionally large effects occur in spontaneous-fission half-lives ($T_{1/2SF}$), of up to 15 orders of magnitude. This can be understood very clearly by comparing the measured spontaneous fission half-lives with those deduced from the LDM (Figure 1.5).

Therefore, SHE only exist due to nuclear shell effects enhancing the nuclear stability.

1.3 Synthesis of SHE

1.3.1 Introduction

As described in the Introduction, all elements heavier than plutonium have to be synthesized and cannot be found in nature. In the universe, presumably elements up to

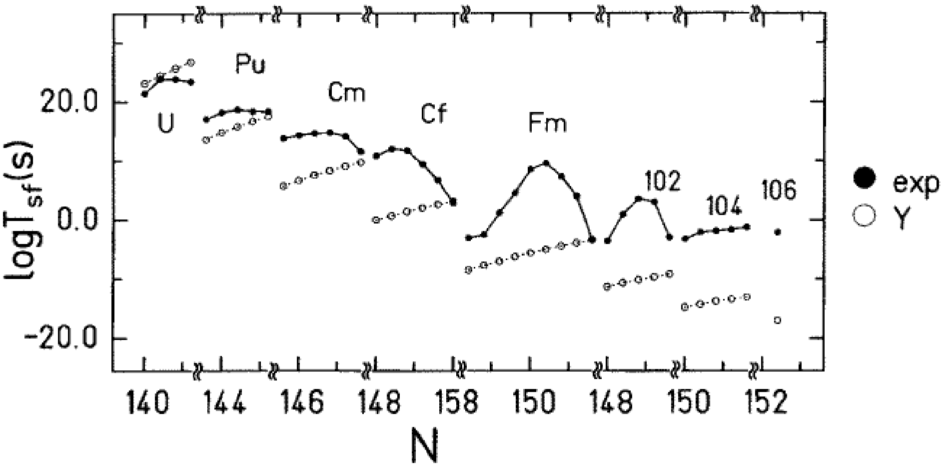

Figure 1.5: Comparison of the measured spontaneous fission half-lives for even-even nuclei with those expected in a simple droplet model approach. Adapted from [23].

Fm can be found in the remains of supernova explosions, produced due to the extremely high neutron flux, by neutron capture followed by β^--decay. Heavier elements, like superheavy elements can so far only be produced in nuclear fusion reactions, fusing two lighter nuclei to a heavy or even superheavy element or in nuclear transfer reactions of two very heavy nuclei.

All fusion reactions can be grouped in two different kinds of reactions, cold and hot fusion, according to the excitation energy of the compound nucleus (CN) at a projectile energy close to the Coulomb barrier (B-Q value). In addition, the term warm fusion is sometimes used to describe reactions using ^{48}Ca as projectiles, with typical excitation energies at the barrier of 25-35 MeV.

In the last 70 years, various approaches have been chosen to formulate models, which theoretically describe the processes taking place during the fusion process itself. All these approaches consider the fusion process as a multi stage process, with 2 to 3 reaction stages, depending on the model used.

The first model [24] used a two stage process, an entrance channel and an exit channel. The entrance channel describes the approach of the projectile to the target nucleus, the overcoming of the Coulomb barrier and the fusion of both nuclei to a highly excited CN. The exit channel describes the de-excitation process by particle and γ emission to the evaporation residue nucleus.

Later these were improved by taking three reaction stages into account instead of two. While in the exit channel, the de-excitation step remains as it was, the entrance channel

is divided in two separate steps, the approach of both nuclei on the one hand and their fusion or reseparation on the other hand.
In this work I concentrate on the latter model, because of its increased precision. This model is used for example by V. Zagrebaev who formulated a standard approach taking this model as a basis [25, 26].

1.3.2 Theory of the complete fusion of heavy nuclei

In his approach Zagrebaev uses three reaction stages to describe the production cross section of a cold residual nucleus, which is formed by light particle, and γ-emission from an excited CN, which has been produced before in the fusion reaction of two heavy nuclei A_1 and A_2:

$$A_1 + A_2 \rightarrow C \rightarrow B + n, p, \alpha, \gamma \tag{1.4}$$

The cross section at center of mass energies close to the Coulomb barrier in the entrance channel is decomposed over partial waves:

$$\sigma_{EVR}^{A_1+A_2\rightarrow B}(E) = \frac{\pi\hbar^2}{2\mu E}\sum_{\ell=0}^{\infty}(2\ell+1)T(E,\ell)\cdot P_{CN}(E,\ell)\cdot P_{EVR}(E^*,\ell) \tag{1.5}$$

This approach consists of three different parts, each characterizing one stage of the reaction:

1. T(E,ℓ) denotes the probability, that the colliding nuclei overcome the potential barrier in the entrance channel (Coulomb barrier) and reach the point of contact $R_{contact} = R_1 + R_2$, where R_1 and R_2 are the radii of the nuclei. This contact point is as a rule by 2 or 3 fm smaller than the radius defining the Coulomb barrier.

2. P_{CN}(E,ℓ) terms the probability, that the nuclear system will develop from a contact configuration of two touching nuclei into a spherical or nearly spherical form of the compound mononucleus. This evolution process is always in competition with the separation in two fragments without forming the CN at all and thus $P_{CN} < 1$. This reseparation process without having formed an CN is called quasi-fission, in contrast to fusion-fission.

3. $P_{EVR}(E^*, \ell)$ or $W_{survival}$ is the probability to produce the cold evaporation residue

B in the process of de-excitation of the CN by emission of light particles (n,p,α) and γ's. The initial excitation energy is E^{*}=$E_{c.m.}$-Q with:

$$Q = M(C) \cdot c^2 - M(A_1) \cdot c^2 - M(A_2) \cdot c^2 \tag{1.6}$$

M(C), M(A_1) and M(A_2) are the masses of the CN, A_1 and A_2.

The process of the fusion reaction leading to the creation of a SHE is schematically shown in Figure 1.6.

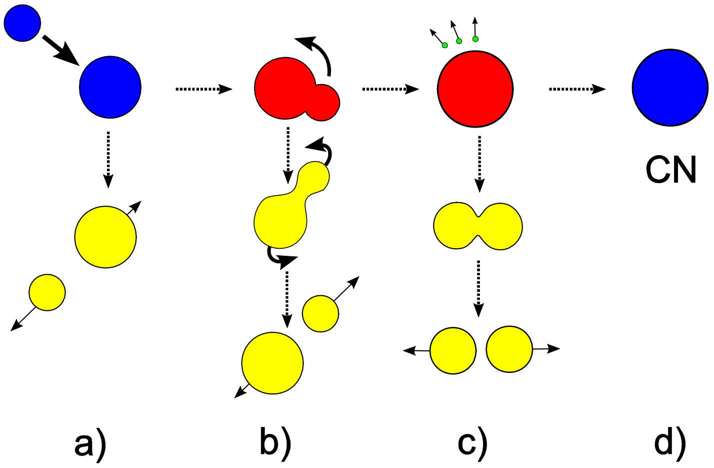

Figure 1.6: Schematic drawing of the fusion reaction towards creation of SHE. Letters under the figure describe different stages: a) collision and possible elastic scattering, b) inelastic scattering and quasi-fission, c) cooling of the excited CN with subsequent neutron evaporations or fission of the CN and d) CN survival. Adopted from [27].

Besides the production cross section, characterizing the formation of the cold evaporation residue, there are two different but also very important cross sections, characterizing parts of the production cross section:

1. $\sigma_{capture}(E)$ is the capture cross section, which describes the fraction of nuclei getting to the contact configuration:

$$\sigma_{capture}(E) = \frac{\pi\hbar^2}{2\mu E}\sum_{\ell=0}^{\infty}(2\ell+1)T(E,\ell) \tag{1.7}$$

2. $\sigma_{fusion}(E)$ is the fusion cross section, which describes the fraction of nuclei, getting to the CN configuration:

$$\sigma_{fusion}(E) = \frac{\pi\hbar^2}{2\mu E} \sum_{\ell=0}^{\infty} (2\ell+1) T(E,\ell) \cdot P_{CN}(E,\ell) \tag{1.8}$$

Capture cross section

The barrier penatrability T(E,ℓ) for the fusion of heavy ions depends on the height and width of the Coulomb barrier. But also the strong channel coupling of relative motion with internal degrees of freedom enhance the capture cross section significantly by several orders of magnitude at subbarrier energies.
The height of the potential barrier can be calculated quite well using the Bass approximation [28] for the interaction between two heavy spherical nuclei. Coupling with the excitation of nuclear collective states and with nucleon transfer channels is the second main factor which determines the capture cross section at near-barrier energies. These collective states are surface vibrations and/or rotations of deformed nuclei and can roughly be divided in two categories:

1. For the fusion of light nuclei, the capture cross section is quite good described by taking into account only a few low-excited states using some coupled channel code.
2. Considering the fusion of heavy nuclei, the nuclei are regarded as rather "soft" nuclei, which means, that these have low lying vibrational excitations. Hence, a realistic nucleus-nucleus interaction leads to very large dynamic deformations and, thus, a large number of coupled channels have to be taken into account complicating the microscopic calculation of T(E,ℓ) significantly.

To take into account the main effect of decreasing the potential barrier height which corresponds to an increasing penetration probability at subbarrier energies due to dynamic deformation of the nuclear surface, Zagrebaev [25] suggests the following nucleus-nucleus potential energy for nuclei with quadrupol deformations:

$$\begin{aligned} V_{1,2}(r,\beta_1,\beta_2,\theta_1,\theta_2) &= V_C(r,\beta_1,\beta_2,\theta_1,\theta_2) + V_{prox}(r,\beta_1,\beta_2,\theta_1,\theta_2) \\ &+ \frac{C_1}{2}(\beta_1-\beta_1^0)^2 + \frac{C_2}{2}(\beta_2-\beta_2^0)^2 \end{aligned} \tag{1.9}$$

where $\beta_{1,2}$ are the dynamic quadrupol deformations, $\beta^0_{1,2}$ are the static deformations, $\theta_{1,2}$ are the orientation of the symmetry axis of statically deformed nuclei and C are the stiffness parameter, calculated within the LDM. In the case of spherical nuclei $\beta^0_1 = \beta^0_2 = 0$ and this potential yields the Coulomb barrier very close to the Bass barrier. In [25] the number of variables is reduced by assuming, that:

1. the deformation energies of the two nuclei are proportional to their mass $\left(\frac{C_1\beta_1^2}{C_2\beta_2^2} = \frac{A_1}{A_2}\right)$
2. only one deformation parameter can be used ($\beta = \beta_1 + \beta_2$)

With this approach, a total potential energy landscape consisting of Coulomb-, nuclear and deformation potential plotted in the (r,β) space is calculated (see Figure 1.7). There are two characteristic points on the potential energy surface:

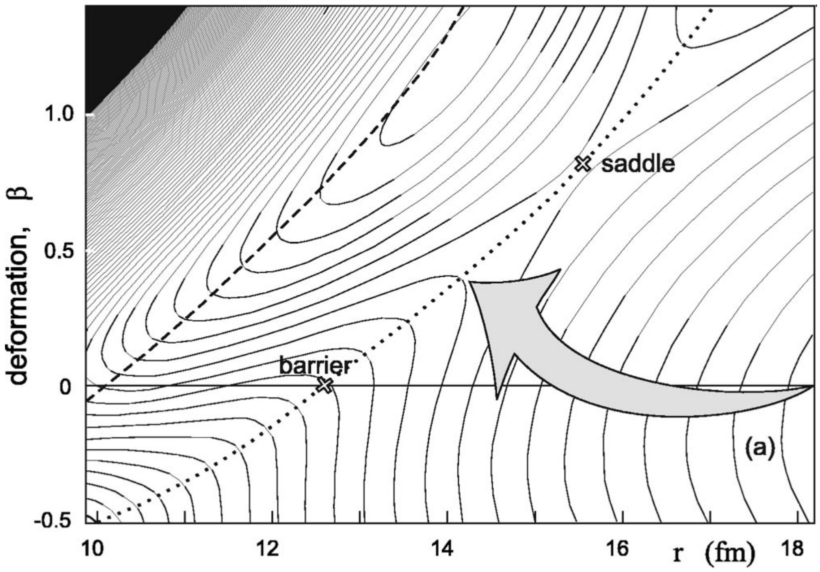

Figure 1.7: Landscape of the potential energy surface of the nuclear reaction ^{48}Ca + ^{208}Pb. The saddle point and the potential barrier of spherical nuclei are shown by crosses. The ridge of the barrier is shown by the dotted line, whereas the dashed line corresponds to the contact distance of the two nuclei. The incoming flux is shown schematically by the grey shaded arrow. Adopted from [25].

1. The potential barrier of two spherical nuclei B_0, which is very close to the Bass barrier (see Figure 1.8 a)

2. Saddle point B_S, the lowest point of the multidimensional barrier, which is much smaller than B_{Bass} (see Figure 1.8 b)

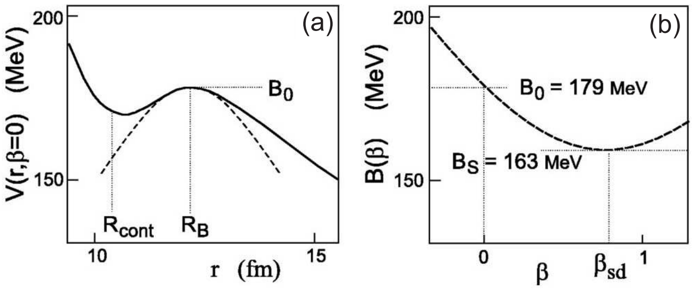

Figure 1.8: (a) Interaction potential of spherical nuclei and its parabolic approximation (dashed line) in the vicinity of the barrier. (b) Potential energy at the ridge of the two-dimensional barrier, i.e., along the dotted line passing through the saddle point. Adopted from [25].

With increasing masses of the interacting nuclei the difference (B_0-B_S) becomes larger. The point of contact is of course much smaller than the barrier. To calculate the penetration probability of this potential, the Hill-Wheeler formula is used in which the barrier height is modified by a centrifugal term to describe the quantum penetration probability of the one-dimensional barrier (see Figure 1.8 a). The radial dependence of the barrier is approximated by a parabola. To take into account the multidimensional character of the real barrier, Zagrebaev introduces a Barrier distribution function f(B) to determine the total penetrability:

$$T(E,\ell) = \int f(B) \cdot \frac{1}{1 + \exp\left(\frac{2\pi}{\hbar\omega_B(\ell)}\left[B + \frac{\hbar^2}{2\mu R_B^2(\ell)}\ell(\ell+1) - E\right]\right)} dB \tag{1.10}$$

$\hbar\omega_B$ ... defined by the width of the parabolic barrier
R_B ... position of the barrier
$f(B)$ ... barrier distribution (normalization condition: $\int f(B)dB = 1$)
$B_M = \frac{(B_0+B_S)}{2}$
$N(\Delta_1, \Delta_2)$...normalization coefficient
$\Delta_2 = \frac{B_0-B_S}{2} = 2MeV$

In general, Δ_1 is less than Δ_2 and can be considered as equal to 2 MeV. The formula for T(E,ℓ) is qualitatively understood and proved to be valid and hence, it can be used as an empirical formula with fitted parameters.

Compound Nucleus Formation

After coming over the Coulomb barrier the two nuclei reach the point of contact. The further evolution of the system depends strongly on the masses of the touching nuclei and on their deformation at that point.

In the case of a strongly asymmetric combination of projectile and target nucleus, the system is transformed into the CN configuration with high probability. Especially for fusion reactions dealing with light and medium nuclei, this probability is close to unity ($P_{CN} \approx 1$).

This happens in the synthesis of heavy elements when the charge of one of the nuclei is lower or of the order of 15. Due to large (B-Q)-values for these reactions, the excitation energies of the formed CN are quite high, of the order of several tens of MeV. Hence, the survival probability of the CN during the cooling process is very low.

In the case of more symmetric nuclear configurations, the system may evolve with a high probability after nucleon transfer reactions took place directly into the fission exit channel without having formed a CN. This process is called "fast fission" or "quasifission".

The evolution of the nuclear system is mainly determined by the character of the multidimensional potential energy, which is determined by collective degrees of freedom playing the major role in this whole process, since at subbarrier collision energies the nuclei practically have zero kinetic energy at the point of contact.

The main problem in describing the process of CN formation in competition with the quasifission process is the correct choice of the aforementioned degrees of freedom, the further derivation of the potential energy and the solution of the transport equation.

There are two basic approaches for describing the evolution of the nuclear system starting from the moment at which the two colliding nuclei touch each other to either the moment of formation of a spherical CN or the moment of reseparation in two fragments (quasifission):

1. An approach assumes, that the two touching nuclei instantly and completely lose their individualities and can be treated as one strongly deformed mononucleus which develops in the multidimensional space of deformation either into a spherical CN or into the fission channel. In practice, the number of used collective degrees of freedom is restricted to only a few, defining the shape of the nuclear system but neglecting the shell structure of the nuclei, which play an important role at low excitation energies and especially at the initial moment of contact. More realistic calculations have been performed using the Langevin equation and taking the shell

effects in the three dimensional potential energy into account [29, 30, 31, 32, 33, 34].

2. An opposite approach has been proposed by Antonenko et al. in 1993. In his model, the two colliding nuclei which have passed the Coulomb barrier and have reached the contact point remain after that in this position, keeping entirely their shapes and individualities. The nucleon transfer only causes subsequent evolution of the "dinuclear system".
   In this approach, CN formation is defined as the complete transfer of all nucleons from the light nucleus to the heavier one. This process competes with the nucleon transfer from the heavy nucleus to the lighter one, resulting in a subsequent separation of the two nuclei (quasifission). [35, 36, 37]

The real situation seems to be somewhere in between both approaches, because it is very unlikely and improbable that during the evolution to an almost spherical nucleus all the nucleons are strictly divided in two groups, nucleons belonging to the projectile only moving in this volume and nucleons of the target only moving in that volume.

The probability of valence nucleon collectivization starts to increase immediately after the contact of the nuclear surfaces took place and after overcoming the Coulomb barrier, as shown in [38]. In a later stage of the evolution, when all the valence nucleons are moving in the volume of both nuclei, the internal or core nucleons with lower energies remain in the volume of their original nucleus.

At the final stage of the CN formation, when the number of shared nucleons is rather large, the concept of the deformed mononucleus resulting from the dinuclear system seems to be suitable.

In 2001 Zagrebaev proposed a new mechanism of the CN formation and the quasifission process [26, 38]. This model assumes, that a certain number of shared nucleons appear when two nuclei get in contact. These nucleons move within the whole volume occupied by the nuclear system and belong to both nuclei forming a neck between the nuclei. Hence the number of such collectivized nucleons increases in contrast to the number of nucleons belonging to each particular nucleus, which decreases.

The CN is formed at the point, when all nucleons are collectivized and arranged in the potential of the CN. The inverse process of nucleon de-collectivization drives the nuclear system to the fission channel [26, 34]. It is interesting to note, that calculations using this formalism have shown, that the quasifission process can also contribute to the yield of symmetric fission fragments, which means, that the common approach of measuring the fusion cross section by measuring the fragment mass distribution of the fissions may have some uncertainties.

Statistical decay of the excited nucleus

The survival probability of the excited CN C(E^*,J) in the process of its de-excitation by emission of neutrons and γ-rays in competition with fission and emission of light charged particles ($C \rightarrow B + x \cdot n + N \cdot \gamma$) can be calculated within the statistical model of atomic nuclei [39]. The partial decay width of the emission of a particle a, a γ-quantum, and for fission respectively can be expressed by the following equations:

$$\Gamma_{C\rightarrow B+a}(E^*, J) = g^{-1} \cdot \int_0^{E^*-E_a^{sep}} \sum_{l,j} T_{l,j}(e_a) \cdot \sum_{I=|J-j|}^{I=J+j} \rho_B(E^* - E_a^{sep} - e_a, I; \beta_2^{g.s.})de_a \tag{1.11}$$

$$\Gamma_\gamma^L(E^*, J) = g^{-1} \cdot \int_0^{E^*} \sum_{I=|J-j|}^{I=J+j} f_L(e_\gamma) \cdot e_\gamma^{2L+1} \rho_C(E^* - e_\gamma, I)de_\gamma \tag{1.12}$$

$$\Gamma_{fission}^L(E^*, J) = g^{-1} \cdot \frac{\hbar\omega_B}{T} \cdot (\sqrt{1+x^2} - x) \cdot \int_0^{E^*} T_{fission}(e, J)\rho_C(E^* - e, J, \beta_2^{sd})de \tag{1.13}$$

$$g = 2\pi\rho_C(E^*, J) \tag{1.14}$$

where ρ_A defines the state density of the nucleus A with the excitation energy E^* and Spin J, and $T_{l,j}(e_a)$ defines the penetration probability of the Coulomb and centrifugal barrier by the light particle a from the nucleus C. Assuming that the electric dipole radiation (L=1) dominated in high energy γ-emission one can use the strength function:

$$f_{E1} = 3.31 \cdot 10^{-6}(\mathrm{MeV}^{-1})\frac{(A-Z)\cdot Z}{A}\frac{e_\gamma\Gamma_0}{(E_0^2 - e_\gamma^2)^2 + (e_\gamma\Gamma_0)^2} \tag{1.15}$$

$$E_0 = \frac{167,23}{A^{1/3}\sqrt{1,969 + 14,074 \cdot A^{-1/3}}} \tag{1.16}$$

$$\Gamma_0 = 5\ MeV \text{ (for heavy nuclei)} \tag{1.17}$$

The equation for the fission width uses the Kramer correction which takes into account the influence of the nuclear viscosity ν, which is typically of the order of $[(1-30) \cdot 10^{21} s^{-1}]$ on the fission probability x.

The penetrability of the fission barrier ($T_{fission}$), depending on the height of the fission barrier of the rotating nucleus ($B_{fission}$) which depends on the moment of inertia at ground state and saddle point can be described by the following equations:

$$T_{fission}(e,J) = \frac{1}{1+\exp(-\frac{2\pi}{\hbar\omega_B}[e - B_{fission}(E^*,J)])} \tag{1.18}$$

$$B_{fission}(E^*,J) = B_0(E^*,J) - (\frac{\hbar^2}{2\Im_{g.s.}} - \frac{\hbar^2}{2\Im_{s.d.}})J(J+1) \tag{1.19}$$

$$\Im_{g.s.,s.d.} = k\cdot\frac{2}{5}MR^2(1+\frac{\beta_2^{g.s.,s.d.}}{3}) \tag{1.20}$$

with the ground state fission barrier ($B_0 = B_{LDM} - \delta W e^{-\gamma_D E^*}$), which contains the fission barrier deduced from the liquid drop model (B_{LDM}) as well as a shell correction energy for the nucleus in the ground state (δW) and a damping parameter (γ_D), which describes the decrease of the influence of shell effects on the energy level density with an increase of the excitation energy.
The level density ρ can be expressed by:

$$\rho(E,J;\beta_2) = \text{const}\cdot K_{Coll}(\beta_2)\frac{2J+1}{E^2}\exp\left(2\sqrt{a\cdot[E-E_{rot}(J)]}\right) \tag{1.21}$$

where K_{Coll} defines the so called collective enhencement factor characterizing the level density enhencement by collective excitations.
Rotating bands of deformed nuclei bring the main contribution to the collective enhancement in the level density. For spherical nuclei the collective enhancement is smaller and is caused by vibrational excitations. The borderline between deformed and almost spherical nuclei is around $|\beta_2| \approx 0.15$. At this deformation, K_{rot} changes very sharply from around 150 to 1 so that K_{vib} is getting mayor influence on K_{coll}. ($K_{vib} \approx 1-10$)

$$K_{Coll}(\beta_2) = \frac{\Im_\perp T}{\hbar^2}\phi(\beta_2) + K_{vib}[1-\phi(\beta_2)] \tag{1.22}$$

$$\phi(\beta_2) = \frac{1}{1+\exp\left[\frac{\beta_2^0+\beta_2}{\Delta\beta_2}\right]} \quad (\beta_2^0 \approx 0.15, \Delta\beta_2 \approx 0.04) \tag{1.23}$$

$$T = \sqrt{\frac{E_{int}}{a}} \tag{1.24}$$

The survival probability depends only on the ratio $\Gamma_n/\Gamma_{fission}$ and hence on the ratio $\rho_B(E-E_n^{sep},\beta_2^{g.s.})/\rho_B(E-B_{fission},\beta_2^{s.d.})$. Therefore, the survival probability of deformed nuclei is independent of the collective enhancement, due to the fact, that the effects of both collective modes are canceling each other out.

For spherical nuclei, the ratio $\Gamma_n/\Gamma_{fission}$ is proportional to $K_{vib}(\beta_2^{g.s.})/K_{rot}(\beta_2^{s.d.})$ and hence the survival probability can be significantly reduced by the collective enhancement factor. In this case, the dependence of K_{coll} on the deformation plays an important role. The calculation of the total survival probability for the formation of a cold EVR after the emission of x neutrons is usually performed within numerical calculations based on the analysis of the multistep decay cascade. Zagrebaev [25] uses for example an explicit analytic expression, which directly takes the Maxwell-Boltzmann energy distribution for the emitted neutrons into account:

$$P_{EVR} = \int_0^{E_0^* - E_n^{sep}(1)} \frac{\Gamma_n}{\Gamma_{tot}}(E_0^*, J_0) P_n(E_0^*, e_1) de_1 \cdot ... \tag{1.25}$$

$$\cdot \int_0^{E_{x-1}^* - E_n^{sep}(x)} \frac{\Gamma_n}{\Gamma_{tot}}(E_{x-1}^*, e_x) \cdot G_{N\gamma}(E_x^*, J_x \rightarrow g.s.) de_x \tag{1.26}$$

Here, $E_n^{sep}(k)$ denotes the binding energy of the k-th emitted neutron and e_k denotes the energy of the k-th emitted neutron. The probability of e_n is given by the probability distribution $P_n(E_k^*, e_k)$, while E_k^* denotes the excitation energy of the EVR after the emission of k neutrons, $E_k^* = E_0^* - \sum_{i=1}^{k} \left[E_n^{sep}(i) + e_i\right]$.

Finally, $G_{N\gamma}$ denotes the probability, that the remaining excitation energy and angular momentum will be emitted by the emission of N γ-quanta. Numerical calculations show, that the average energy of the emitted γ-quanta is in the range of 0.1 to 1 MeV and that their influence on the final cross section is weak, except for the $0n$ evaporation channel.

1.3.3 Predicted cross sections for the formation of ^{270}Hs from different nuclear fusion reactions

As described above, nuclear fusion reactions can be divided in three subsections, cold, warm and hot fusion, depending on the excitation energy of the EVR at near barrier incident energies. Cold fusion reactions are based on closed spherical shell target nuclei of lead and bismuth in combination with various projectile nuclei. In practice only projectiles up to zinc are used due to the sharp drop of the EVR cross section, but also even heavier projectiles have been used, so far without success [40].

While the excitation energy of EVR produced in cold fusion reactions is rather low and hence the survival probability is higher compared with other fusion reaction types due to fewer evaporated neutrons, the fusion probability is much lower. Especially with

increasing charge of the synthesized superheavy elements, the latter factor becomes dominant decreasing the yield of EVR dramatically.
There are two factors for that behavior. On the one hand, the EVRs produced in cold fusion reactions are neutron deficient and far away from closed shells or sub shells and hence neutron separation energies are rather high and fission barriers are rather low. Hence the survival probability is reduced. On the other hand, and this is the mayor reason, the fusion probability decreases sharply with increasing charge of the projectile. As shown in [41], the fusion probability shows two major dependences, an energy and an asymmetry dependence. The energy dependence means the difference of the ′internal′ excitation energy of CN ($E^*_{int}(\ell) = E_{c.m.} + Q - E_{rot}(\ell)$) and the excitation energy of the CN at the center-of-mass energy equal to the Bass barrier (E^*_B) and can be formulated in the case of cold fusion as:

$$P_{CN}(E^*, \ell) = \frac{P^0_{CN}}{1 + \exp\left[\frac{E^*_B - E^*_{int}(\ell)}{\Delta}\right]} \tag{1.27}$$

The $E^*_B - E^*_{int}(\ell)$-dependence corresponds approximately to the $(B - Q)$ value.
The asymmetry dependence is included in P^0_{CN} as:

$$P^0_{CN} = \frac{1}{1 + \exp\left[\frac{Z_1 Z_2 - \zeta}{\tau}\right]} \tag{1.28}$$

In this formula, ζ and τ are just fitted parameters. Although this formulas are only valid for cold fusion reactions, the main conclusions and dependences are valid [42] also in the case of warm and hot fusion reactions. The energy and asymmetry dependence still have a mayor influence on the fusion probability and hence on the EVR cross section. One very interesting and also very important question is which of those two dependences plays the major role for the synthesis of superheavy elements. In order to study the systematics of fusion probability without dealing with exit channel effects, like the survival probability, different fusion reactions resulting in the same CN are investigated. These reactions have on the one side different asymmetries and on the other side, due to their nuclear structure slight or large differences in their (B-Q)-values.

In the case of the doubly magic nucleus ^{270}Hs, different reactions, leading to the same CN (^{274}Hs) can be studied with the aim to investigate the influence of mass asymmetry and (B-Q)-value on the CN formation in the entrance channel. These are ^{26}Mg + ^{248}Cm, ^{30}Si + ^{244}Pu, ^{36}S + ^{238}U, and ^{48}Ca + ^{226}Ra. Bass barrier, Q-value, (B-Q)-values and

$Z_1 \cdot Z_2$ (proportional to the reaction asymmetry) are displayed in Table 1.1. As can be seen, these reactions differ in their asymmetry, from the most asymmetric reaction $^{26}\mathrm{Mg} + {}^{248}\mathrm{Cm}$ to the most symmetric reaction $^{48}\mathrm{Ca} + {}^{226}\mathrm{Ra}$, as well as in their excitation energy at the center-of-mass energy equal to the Bass barrier $(B - Q)$. Here, the reaction $^{48}\mathrm{Ca} + {}^{226}\mathrm{Ra}$ has the lowest and hence the most favorable value. The reaction $^{30}\mathrm{Si} + {}^{244}\mathrm{Pu}$ has the highest and thus the most unfavorable value. The interesting question is, which of both parameters are dominant and hence, which reaction provides the highest yield compared with the others.

Table 1.1: Bass barrier, Q-value, (B-Q)-values and $Z_1 \cdot Z_2$ for various reactions leading to the CN $^{274}\mathrm{Hs}$.

Reaction	B [MeV]	Q [MeV]	(B-Q) [MeV]	$Z_1 \cdot Z_2$
$^{26}\mathrm{Mg} + {}^{248}\mathrm{Cm}$	126.9	-82.2	44.7	1152
$^{30}\mathrm{Si} + {}^{244}\mathrm{Pu}$	144.0	-98.0	46.0	1316
$^{36}\mathrm{S} + {}^{238}\mathrm{U}$	159.1	-116.7	42.4	1472
$^{48}\mathrm{Ca} + {}^{226}\mathrm{Ra}$	187.0	-153.9	33.1	1760

Recently, the formation of deformed doubly-magic $^{270}\mathrm{Hs}$ in the 4n evaporation channel in the complete fusion reactions $^{248}\mathrm{Cm}(^{26}\mathrm{Mg}, 4n)$, $^{244}\mathrm{Pu}(^{30}\mathrm{Si}, 4n)$, $^{238}\mathrm{U}(^{36}\mathrm{S}, 4n)$, and $^{226}\mathrm{Ra}(^{48}\mathrm{Ca}, 4n)$ has been studied theoretically in more detail using a two-parameter Smoluchowski equation[43]. Due to a lower reaction Q value, the reactions $^{238}\mathrm{U}(^{36}\mathrm{S}, 4n)^{270}\mathrm{Hs}$ ($\sigma_{theo} = 24$ pb) and $^{226}\mathrm{Ra}(^{48}\mathrm{Ca}, 4n)^{270}\mathrm{Hs}$ ($\sigma_{theo} = 30$ pb) are predicted to have higher cross sections compared to the reactions $^{248}\mathrm{Cm}(^{26}\mathrm{Mg}, 4n)^{270}\mathrm{Hs}$ ($\sigma_{theo} = 12$ pb) and $^{244}\mathrm{Pu}(^{30}\mathrm{Si}, 4n)^{270}\mathrm{Hs}$ ($\sigma_{theo} = 8$ pb). The calculated excitation functions of these reactions can be found in Figure 1.9.

A maximum cross section for the $^{226}\mathrm{Ra}(^{48}\mathrm{Ca}, 4n)^{270}\mathrm{Hs}$ reaction of about 30 pb was also predicted in other calculations, using a different method[41], which has been shown to reproduce experimental cross sections for various $^{48}\mathrm{Ca}$-based fusion reactions with actinide targets. The calculated excitation functions for the $2n$ - $5n$ evaporation channel can be found in Figure 1.10.

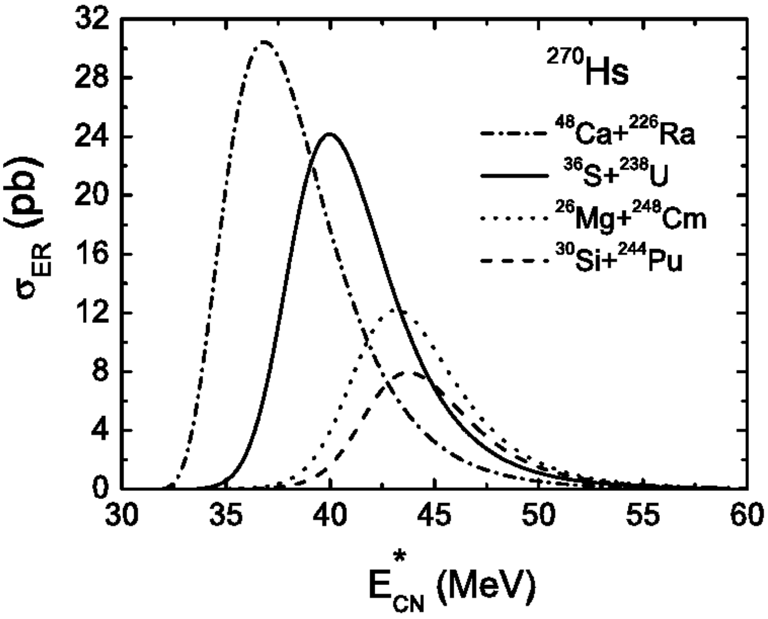

Figure 1.9: Evaporation residue cross sections (σ_{ER}) for the $4n$ channel of the complete fusion reactions ^{26}Mg+^{248}Cm, ^{30}Si+^{244}Pu, ^{36}S+^{238}U and ^{48}Ca+^{226}Ra. Adopted from [43].

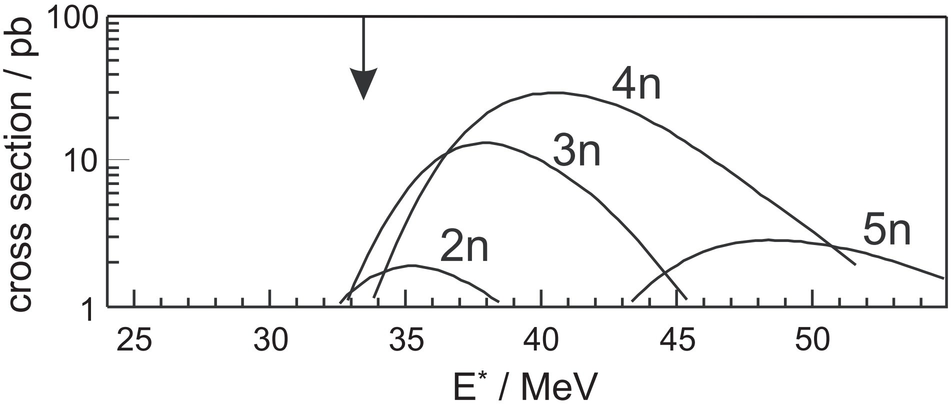

Figure 1.10: Excitation functions for the $2n$- to $5n$-evaporation channels of the complete-fusion reaction ^{48}Ca+^{226}Ra. The Bass barrier B_{Bass} [28] is shown by an arrow. Adapted from [41].

HIVAP

HIVAP (Heavy-Ion VAPorisation statistical-evaporation model) is a computer code for calculating EVR cross sections from heavy ion induced fusion reactions [44]. It was developed and improved by W. Reisdorf and M. Schädel. It has been shown during the last two decades that HIVAP reproduces experimental measured EVR cross sections up to element 106 within a factor of 2-3. HIVAP takes into account a dynamically fluctuating barrier for the fusion probability and temperature dependent shell effects in the level density for the fission probability.

HIVAP uses conventional statistical decay theory, assuming that the formation of the compound nucleus by complete amalgamation of projectile and target nuclei is a step completely independent of the subsequent deexcitation by nuclear fission and/or emission of light particles and gamma rays. Fusion is assumed to occur whenever a fusion barrier calculated from the global nucleus-nucleus potential of Bass [28] is passed. Below the barrier, a WKB transmission calculation is performed.

Due to coupled channels effects the barrier is "distributed" [45, 46]. For the mostly deformed actinide target nuclei, the experimentally known deformation by orientation averaging have been taken into account and on top of this orientational barrier fluctuation another independent "vibrational-plus-transfer" contribution has been added. As a phenomenological parameterisation of this barrier distribution, a Gaussian distribution cut off at both ends after 5 standard deviations has been used. Such a phenomenological approach [47] reproduces reasonably well experimental subbarrier fusion excitation functions.

The sensitive parameters, which are involved in the second-deexcitation-step, are primarily level density parameters, fission barriers, and masses. The masses are used to deduce particle separation energies and shell corrections. Whenever possible, they were taken from experiment. Otherwise the predictions of Liran and Zeldes [48] were used. The code follows the evaporation chain through all the steps allowing for neutron, proton, alpha, and gamma emission in addition to (multiple chance) fission. The transmission through the fission barrier was calculated by the classical approximation.

To demonstrate the accuracy of HIVAP concerning the prediction of experimental EVR cross sections, the excitation functions for $4n$ through $8n$ evaporation channels from the $^{238}\mathrm{U}(^{12}\mathrm{C}, xn)^{250-\mathrm{x}}\mathrm{Cf}$ reaction are shown in Figure 1.11.

Very good agreement between the experiment and the calculation is achieved not

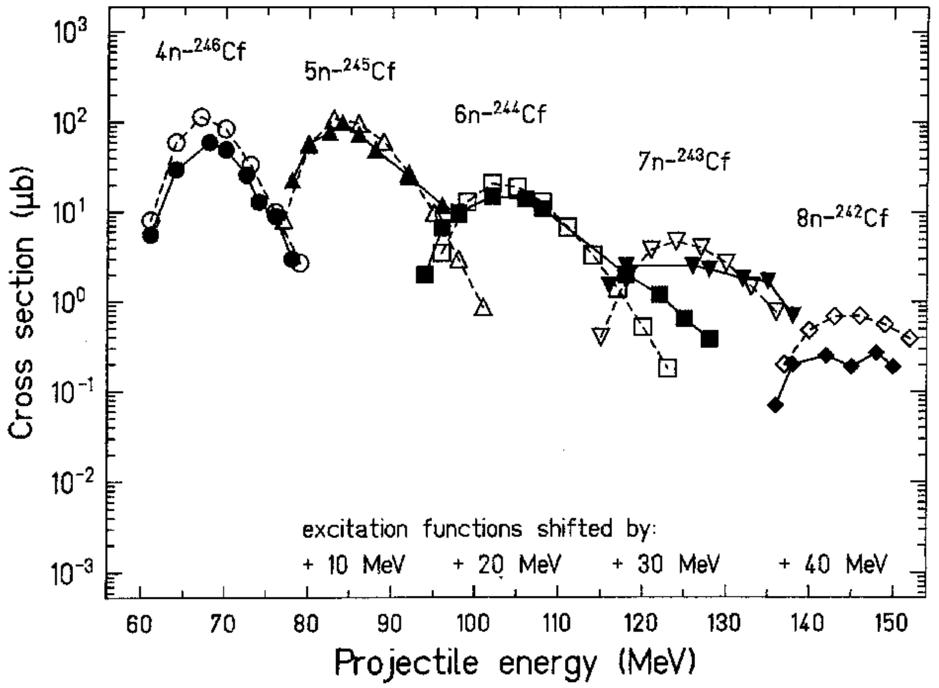

Figure 1.11: Excitation functions for the $^{238}\text{U}(^{12}\text{C}, xn)^{250-\text{x}}\text{Cf}$ reaction. Open symbols are from HIVAP calculations, full symbols are experimental. Adapted from [44].

only for the position of the maxima but also for absolute cross section values. The largest discrepancies as observed for the 7n and 8n evaporation channel are still less than a factor of three. This clearly demonstrates the validity of these calculations in the range of compound nucleus excitation energies from 34 MeV (61 MeV projectile energy in Figure 1.11) up to more than 80 MeV.

HIVAP calculations for the complete nuclear fusion reaction $^{238}\text{U}(^{36}\text{S}, xn)^{274-\text{x}}\text{Hs}$ have been performed by Ch. E. Düllmann [49]. The results for the 3n-6n channel are displayed in Figure 1.12.

HIVAP predicts the 3n channel to be the dominant channel with a maximum cross section of about 10 pb at an excitation energy of about 30 MeV. The 4n and 5n channel are predicted to have maximum cross sections of about 3 pb at 38 MeV and 48 MeV, respectively. At 38 MeV, HIVAP also predicts a cross section of about 1 pb for the 3n channel. The 6n channel should provide a maximum cross section of about 0.3 pb at 56 MeV. It is important to note, that predictions from HIVAP for the 4n channel are about one order of magnitude lower that predictions made by Liu et *al.* [43].

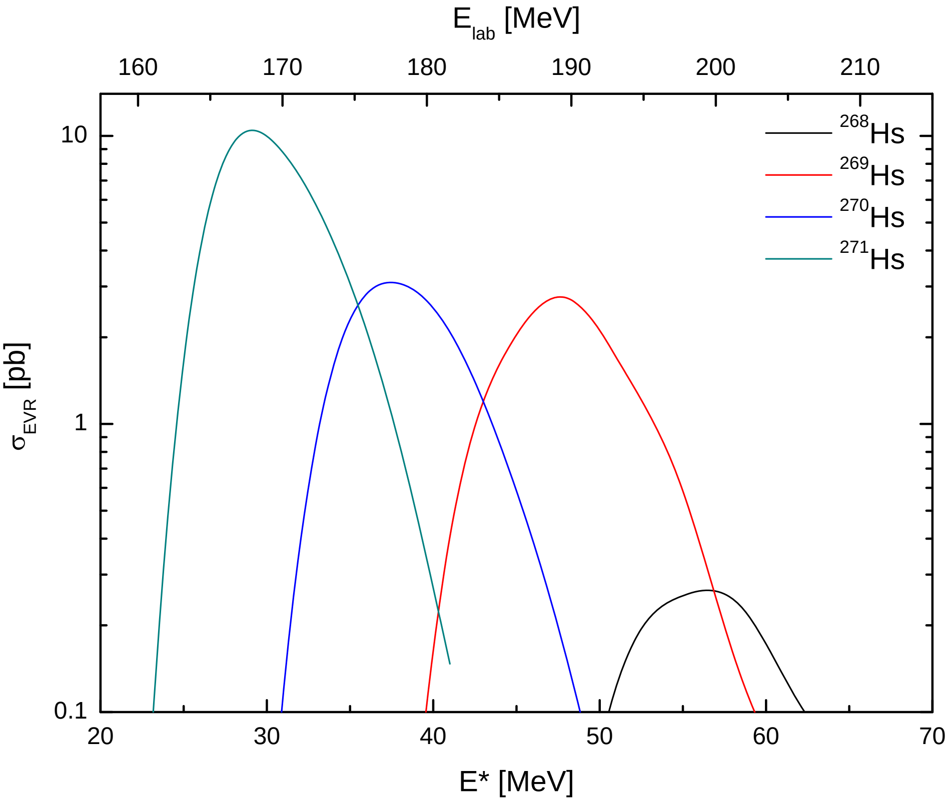

Figure 1.12: HIVAP predictions for the excitation functions for the $^{238}\mathrm{U}(^{36}\mathrm{S}, xn)^{274-\mathrm{x}}\mathrm{Hs}$ reaction.

1.3.4 Experimental challenges on the production of SHE

SHE are produced in heavy-ion induced complete nuclear fusion reactions, followed by sequential evaporation of one or several neutrons. The projectile and target nucleus form an excited CN, which is highly unstable and undergoes fission, unless it de-excites rapidly by emission of neutrons and γ-rays. During each step of de-excitation by neutron emission, a competition with fission takes place, which makes the survival probability extremely sensitive on the fission barrier. Due to the repulsive Coulomb force between target and projectile nucleus, the latter has to overcome the fusion barrier. Even if the projectile energy is high enough to overcome this barrier, the impact parameter plays a very important role, since the nuclei only get in touch at small impact parameters. If those parameters are too large, the incident projectile is deflected. This corresponds to elastic scattering, when the kinetic energy of the incident particles is conserved (large impact parameters). At medium impact parameter inelastic scattering takes place, when the kinetic energy of the incident particles is not conserved and the target nucleus gets excited due to electromagnetic or nuclear forces. Hence, the probability of a capture of the projectile by the target nucleus and a further CN formation followed by de-excitation (successive neutron emission without fissioning) is strongly suppressed compared with reaction channels, like transfer reactions. These reaction channels lead to a huge amount of different nuclei with cross sections in the order of b. In addition, also elastically scattered target nuclei recoil out of the target with high cross sections. Compared with EVR cross sections for the production of ^{270}Hs in complete nuclear fusion reactions, which are of the order of pb, these are higher by a factor of one trillion! Hence, highly efficient and selective separation methods have to be applied in order to reduce the unwanted background of byproducts. Since the half-lives of SHE decrease with increasing atomic number, the separation techniques have to be also very fast.

During the last decades, two basic separation techniques have proven their worth. On the one hand, chemical methods have been used to separate selectively SHE from transfer reaction products due to their chemical properties based on the atomic number. Using chemical arguments, the discovery of a new element can be established. The limiting factor of this technique is the half-life of the SHE which has to be at least half a second for gas phase chemistry and several tens of seconds for liquid phase chemistry. On the other hand, electromagnetic recoil separators have been developed, separating the reaction products due to their ionic charge and momentum. The separation times are determined here by the recoil velocity and the length of the separator, providing the study of SHE with half-lives as short as few microseconds.

1.4 Decay properties of SHE

In this section, I would like to refer to the common decay modes and properties of SHE. Due to the large number of positively charged protons bound inside of the nucleus, SHE can and will increase their binding energy by radioactive decay. These decays, especially the α-decays are unique for every isotope (like a fingerprint) and hence the formation of a SHE nucleus can be unambiguously established by measuring its characteristic decay-pattern. This method is especially convincing when the observed decay chain leads into the region of already well known nuclei.

1.4.1 Decay properties and stability of heaviest elements

As mentioned before, SHE only exist due to nuclear shell effects, enhancing the nuclear stability. Hence, the half-lives and decay modes of these depend mainly on the strength of those effects and therefore on shell closures in the SHE area. Due to this, one very important and interesting point is the prediction of closed shells or sub shells beyond the closed spherical proton and neutron shells at Z=82 and at N=126. Several possible proton shell closures are predicted, at Z=114, 120, or 126, depending on the model used [2,3,4,5]. On the neutron side, most models agree, that the next closed shell is expected at N=184 [3,4]. Beside these predicted spherical shell closures, deformed shell closures can be found. Improved calculations for shell closures including higher orders of deformation, predicted a closed deformed proton and neutron shell at Z=108 and N=162 [6,23,50], with shell correction energies similar to those, resulting for spherical shell closures. Measurements of Q_α-values show, that nuclei around Z=108 and N=162 have lower Q_α-values, which correspond to longer half-lives, indicating that these two deformed shell closures really exist [51,52]. Around these closed shells, an area of nuclides of relative stability and hence longer half-lives was predicted to form a so called island of stability, which is surrounded by nuclei with reduced stability and hence shorter half-lives. The systematics of spontaneous-fission half-lives reflects the systematics of shell-correction energies in the SHE area, since these properties are directly connected. As can be seen in Figure 1.13, a significant increase of (negative) shell-correction energy (a) and hence a major increase of SF half-life (b) from 10^3 s for deformed and 10^{12} s for spherical SHE was calculated.

The much stronger increase of SHE half-lives for spherical shell closures originates from an increase of the fission barrier width, which becomes much wider than for de-

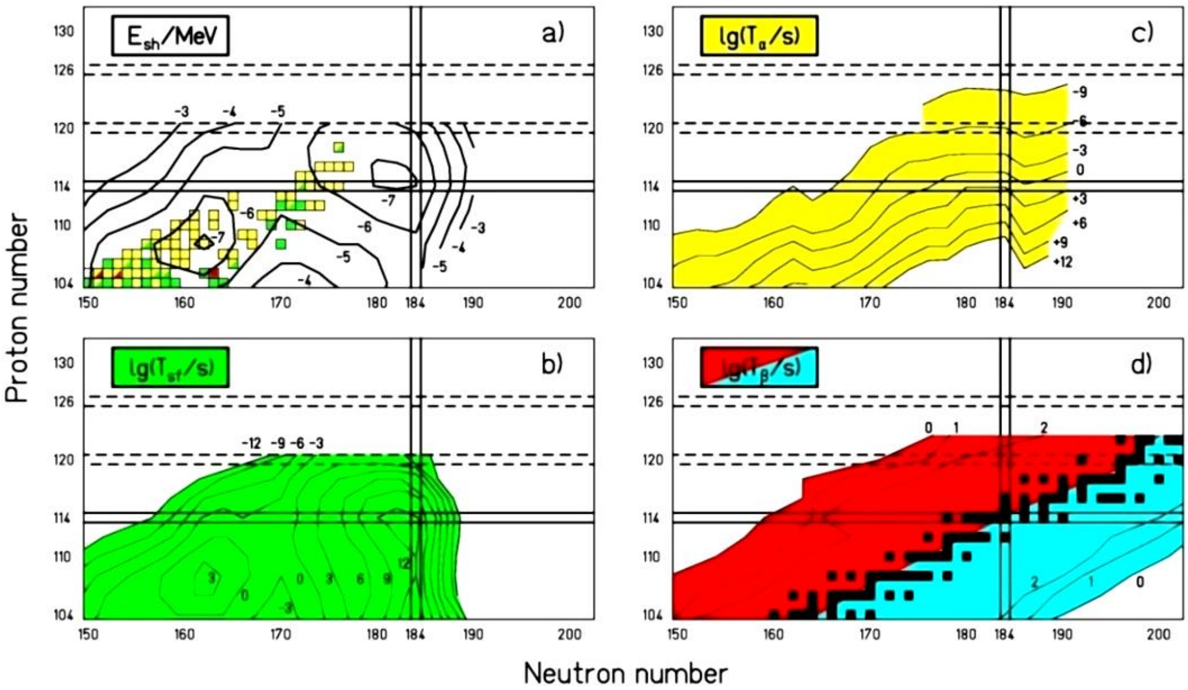

Figure 1.13: Shell-correction energy (a) and partial half-lives for SF (b), α-decay (c) and β-decay (d). Figure adapted from [53], using data from [54].

formed shell closures. The plots reflect the spherical shell closures at Z=114 and N=184 (solid lines), but also the two other candidates for proton shell closures at Z=120 and Z=126 (dashed lines) are included. As can be seen in Figure 1.13, partial α- and β-decay half-lives are only slightly influenced by shell effects, as their decay process occurs between neighboring nuclei. Partial α-decay half-lives at N=184 decrease monotonically from 10^{12} s near Z=114 down to 10^{-9} s near Z=126. The valley of β-stability passes through the spherical shell closures at Z=114 and N=184. A β-decay half-life of less than one second is reached at a distance of more than 20 neutrons from the bottom of the valley [55].

Enhanced stability and decay properties around Z=108 and N=162

As mentioned before Sobiczewski and co-workers performed improved shell correction energy calculations, including higher orders of deformation [6, 23, 50]. These calculations revealed a deformed proton and neutron shell closure at Z=108 and N=162. This can be clearly seen in a contour map containing the ground-state shell correction energies E_{sh} of nuclei in a wide range of nuclei with proton number Z=82-120 and neutron number

N=126-190 (see Figure 1.14). The plot reveals three minima in this region. The first and deepest ($E_{sh} = -14.3$ MeV) is obtained for the doubly magic spherical nucleus ^{208}Pb. The second one ($E_{sh} = -7.2$ MeV) is arranged at the nucleus ^{270}Hs, which is predicted to be a doubly magic deformed nucleus [6, 50]. The third minimum ($E_{sh} = -7.2$ MeV) can be found for the nucleus ^{298}114, which is predicted to be the next heavier doubly magic spherical nucleus to the last experimentally known doubly magic ^{208}Pb. Beside these minima, a rather wide plateau can be found around ^{252}Fm, which can be considered as a nucleus with closed deformed sub-shells [6, 50].

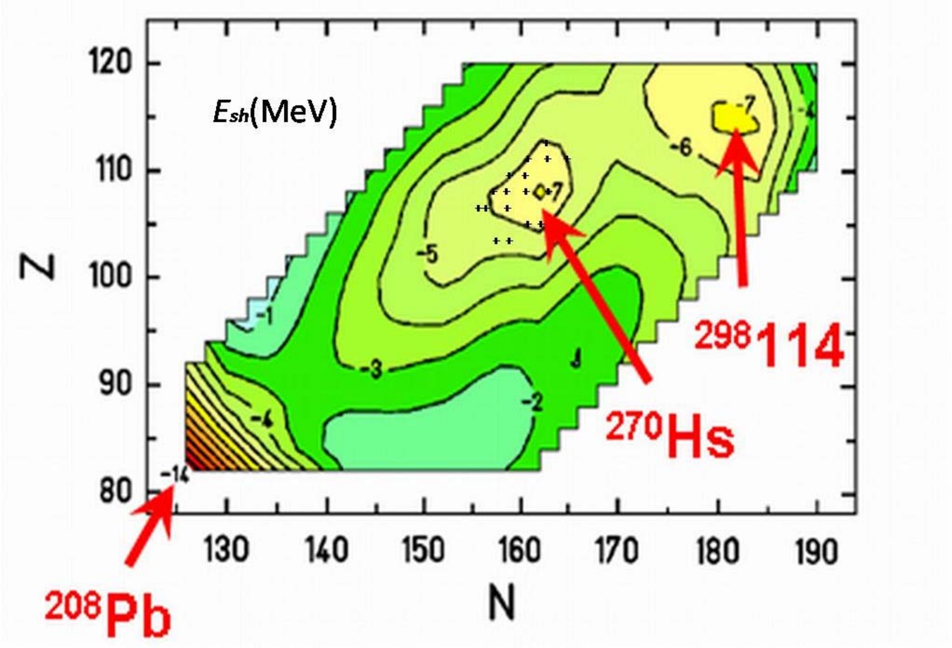

Figure 1.14: Contour map of ground-state shell correction energies E_{sh}. Adopted from [27].

The stabilization effect is also reflected by α-decay energies (Q_α) systematics near and at closed shells, due to a relation between partial α-decay half-lives and Q_α values. This relation can be evaluated using the phenomenological Viola-Seaborg formula, which was modified by Parkhomenko and Sobiczewski [56]. The partial α-decay half-life is estimated as:

$$\log_{10} T_\alpha^{ph}(Z, N) = aZ(Q_\alpha - \bar{E}_i)^{1/2} + bZ + c, \tag{1.29}$$

Here, Z denotes the proton number; a,b,c are parameters fitted to experimental data and $\bar{E}_i$ varies for different nuclei as follows:

$$\bar{E}_i = \begin{cases} 0 & \text{for even-even nuclei,} \\ \bar{E}_p & \text{for even-odd nuclei,} \\ \bar{E}_p + \bar{E}_n & \text{for odd-odd nuclei,} \end{cases} \tag{1.30}$$

$$\begin{aligned} a = 1.5372, \qquad b = -0.1607, \qquad c = -36.573 \\ \bar{E}_p = 0.113 \text{ MeV}, \qquad \bar{E}_n = 0.171 \text{ MeV} \end{aligned} \tag{1.31}$$

$\bar{E}_p$ and $\bar{E}_n$ correspond to the average excitation energy of proton and neutron one-quasiparticle states, which become occupied after α-particle emission. Using this formula it is possible to derive values for T_α within a factor of four (within a factor of two for even-even nuclei). The main conclusion of this formula is that the partial α-decay half-life is antipropotional to the α-decay energy. In Figure 1.15 calculated Q_α-values of even-even nuclei are plotted and compared with experimentally measured values for nuclei close to ^{270}Hs.

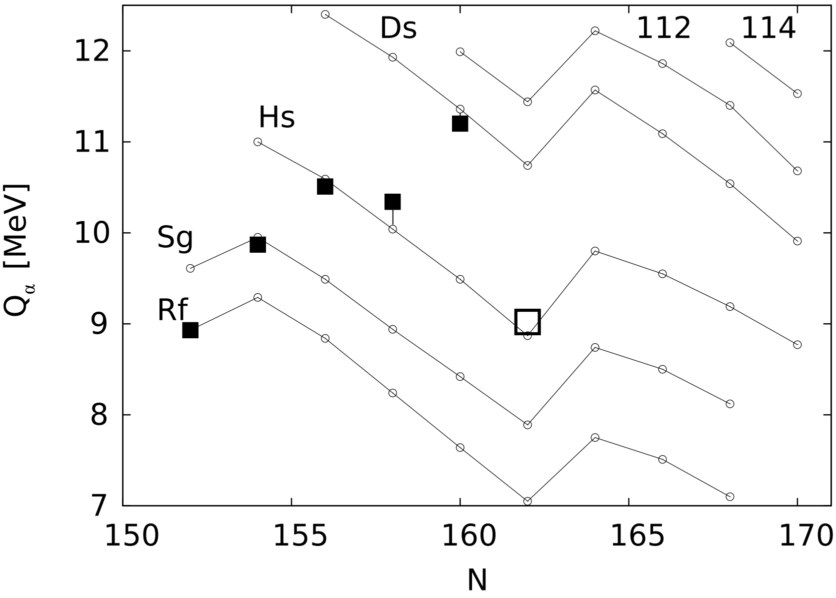

Figure 1.15: Comparison of Q_α values from theoretical calculations [57, 58] and experimental data [51, 59, 60, 61] for even-even nuclei. Adopted from [51].

The closed Z=108 proton shell can be seen as a large gap between Hs and Ds isotopes. Hence, going from Hs to Ds isotopes, Q_α decreases corresponding to an increase in T_α, reflecting enhanced stability for Hs isotopes (Z=108). In addition, the shell closure at N=162 also enhances stability of isotopes leading to a local minimum at N=162. The dominat decay mode can be obtained by comparing the results for partial half-lives as shown in Figure 1.16 for even-even nuclei. In general, the regions around the shell closures of ^{270}Hs and ^{298}114 form a landscape of α-particle emitters surrounded by spontaneously fissioning nuclei. From the decay scenario in Figure 1.16 follows, that the most likely decay mode of ^{270}Hs as well as ^{268}Hs and ^{272}Hs is α-decay. While ^{270}Hs is expected to have a half-life of the order of a few seconds, both other isotopes should decay within a half-life shorter than one second as a result of stabilization effects of the N=162 closed shell. The possible daughter nuclides ^{266}Sg and ^{262}Rf are expected to decay via SF, which is more probable than α-decay. For even-odd nuclei, similar calculations can be done resulting in α-decay as dominate decay mode for ^{269}Hs and ^{271}Hs as well as for their daughters ^{265}Sg and ^{267}Sg. For ^{261,263}Rf partial half-lives for α-decay and SF are comparable and hence there will be an almost equal α/SF branching.

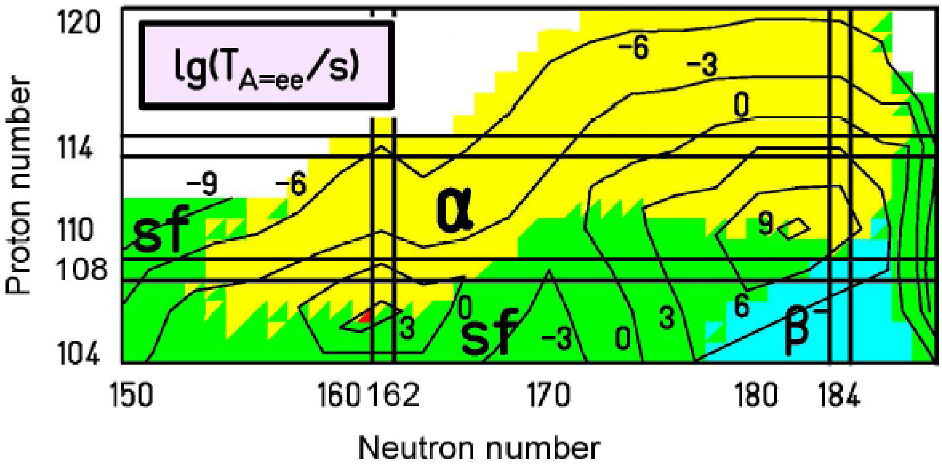

Figure 1.16: Decay scenario in the region of SHE for even-even nuclei. Data from [54].

1.4.2 Decay properties and production of isotopes near Z=108, N=162

The estimates of Section 1.4.1 have been mostly confirmed in experiments aiming at the investigation of the decay properties of Hs-isotopes in the last decade [7, 51, 52, 62]. For ^{269}Hs, α-α-α-α or α-α-SF decay chains are known from previous experiments [7, 63, 64, 65].

For decay of ^{268}Hs and ^{270}Hs, α-SF cascades have been observed [51, 62], while ^{271}Hs decays via α-α-SF or α-SF chains [52]. The decay properties of these Hs isotopes near N=162 are summarized in Table 1.2 and Figure 1.17.

Table 1.2: Decay Properties of $^{269-271}$Hs and daughter nuclei measured in previous experiments. Data taken from [8, 66, 67, 68, 69].

Nuclide	decay mode branching	$T_{1/2}$	E_α [MeV]
^{268}Hs	α	≤ 0.5 s	9.44
^{269}Hs	α	9.7 s	8.95, 9.13
^{270}Hs	α	$\sim$ 23.0 s	8.88
^{271}Hs	α	$\sim$ 4 s	9.13, 9.30
^{264}Sg	SF	68^{+37}_{-18} ms	
^{265a}Sg	α	$8.9^{+2.7}_{-1.9}$ s	8.80-8.90
^{265b}Sg	α	$16.2^{+4.7}_{-3.5}$ s	8.70
^{266}Sg	SF	359^{+248}_{-104} ms	
^{267}Sg	α/SF 0.17/0.83	$84.3^{+58.1}_{-24.2}$ s	8.20
^{261a}Rf	α	68 ± 3 s	8.28
^{261b}Rf	α/SF 0.09/0.91	3 ± 1 s	8.51
^{263}Rf	SF	$8.3^{+39.8}_{-3.8}$ s	

From Q-value interpolations of all known Hs isotopes, an α-particle-energy of about 9.44 MeV for the decay of ^{268}Hs can be deduced. From results of a chemical search experiment for this nuclide follows that its half life is most likely $\leq$0.5 s [69]. The decay properties of ^{268}Hs have been investigated for the first time in 2009 using the velocity filter SHIP at the GSI [62]. The complete nuclear fusion reaction $^{238}\text{U}(^{34}\text{S}, xn)^{272-\text{x}}\text{Hs}$ has been used and one decay chain of ^{268}Hs was measured. The production cross section was $0.54^{+1.3}_{-0.45}$ pb. The decay properties of ^{269}Hs, ^{270}Hs, and ^{271}Hs have been investigated in previous Hs chemistry experiments using the complete fusion reaction $^{248}\text{Cm}(^{26}\text{Mg}, xn)^{274-\text{x}}\text{Hs}$ [7, 51, 52]. In addition, the excitation functions of the 3-5n exit channels of this reaction have been measured at five different beam energies [8] in two experimental campaigns, using an improved chemical separation and detection system. In former experiments, it has been shown, that Hs chemistry is very selective and effective [7]. An overall efficiency of around 55% for the separation and detection of ^{269}Hs was reached. Maximum cross sections of about 3 pb, 3 pb, and 7 pb for the 3n, 4n, and 5n channel have been observed, respectively.

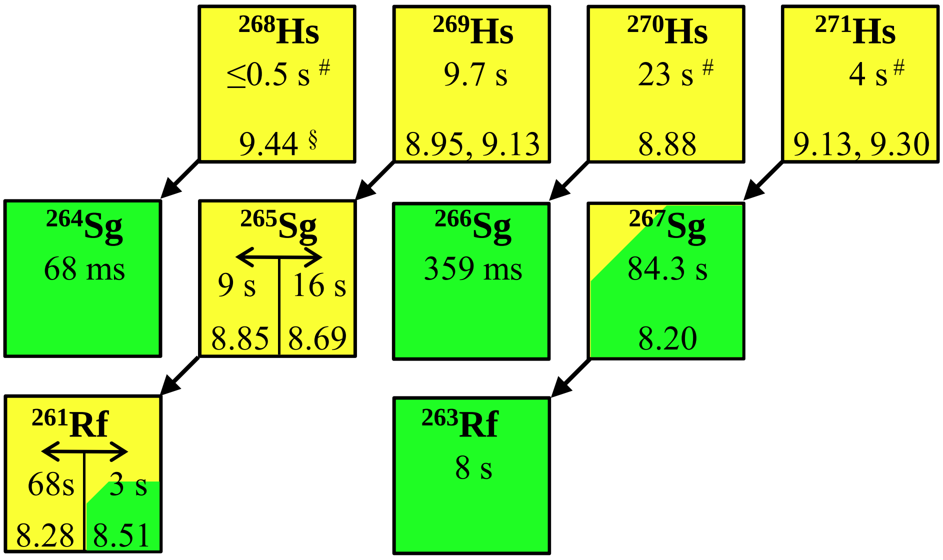

Figure 1.17: Decay properties of Hs isotopes and daughters. The half-lives of Hs isotopes marked with a sharp ($^{\#}$) were calculated according to the formalism outlined in [56]. The α-decay-energy of ^{268}Hs marked with a paragraph sign (§) is calculated from the Q$_\alpha$-value of ^{268}Hs deduced from Q$_\alpha$-systematics based on all known Hs-isotopes [69].

1.5 Kinematic separators

1.5.1 Overview

As S. Hofmann has described [1], a separator for fusion reactions should fulfill three specifications:

1. The separation mechanism should base on physical principles
2. It should be faster than all previous technologies
3. It should be optimized for fusion reactions

Under these conditions, three types of separators can be considered:

1. Gas-filled separators
   Gas filled separators contain a light-weight gas, usually helium (like TASCA or BGS), hydrogen (like TASCA or DGFRS) or mixtures of both, at low pressure, usually 0.5 mbar to 1 mbar. A charge distribution around an average charge-state of the fusion products, recoiling out of the target, is achieved by colliding and interacting several times with the gas atoms. The separation of the fusion products from beam particles and other products is obtained by the magnetic field of a dipole magnet, deflecting the particles due to their mass, charge state and velocity, which define their magnetic rigidity. Only particles with a defined magnetic rigidity are guided through a dipole magnet.

2. Velocity separators
   Velocity or kinematic separators are so called Wien filters, which consist of electric and magnetic dipole fields, separating the particles leaving the target by their velocity. While the deflection in the electric field is $\sim \frac{q}{m \cdot v^2}$, in the magnetic field it is $\sim \frac{q}{m \cdot v}$. By combining both fields, only particles with a certain velocity can pass the separator.

3. High frequency filters
   For accelerators like the UNILAC at the GSI, which accelerate the projectiles as bunches, another concept for separating fusion products can be applied. The idea is to place a high frequency resonator behind the target working at the same frequency as the accelerator but with an electric field transverse to the beam direction. Because of technical difficulties, this concept has never been realized.

1.5.2 Theory and layout of gas-filled separators

Heavy ions, passing a gas at low pressure, are changing their charge state due to collisions with the gas atoms [70]. Either they lose electrons and get into a higher charge state or they capture electrons from the gas atoms or molecules and decrease their charge state. If the path length of the ion in the gas is much larger than the mean free path between these collisions, a charge distribution around an average charge state is established. The trajectory of the heavy ions passing through the magnetic dipole field depends on their properties, the average charge state, mass, and velocity, and on the magnetic field strength and is described by the following formula:

$$B\rho = \frac{mv}{qe} \tag{1.32}$$

Using the Thomas-Fermi atomic model, the average charge state can be described as:

$$\overline{q} = \left(\frac{v}{v_0}\right) Z^{\frac{1}{3}} \tag{1.33}$$

By using this approximation, the magnetic rigidity of the ion is now only characterized by its A and Z and independent of the velocity and of the initial charge distribution:

$$B\rho = 0.0227 \cdot \frac{A}{Z^{\frac{1}{3}}}\ Tm \tag{1.34}$$

This formula is only valid, if the time between two interactions is larger than the de-excitation of an excited state of an ion. If this is not the case, the so-called density effect takes place, which describes the fact, that an excited electron can be stripped from a heavy ion more easily than an electron in the ground state [71]. This effect changes of course the charge state distribution and the average charge state substantially and hence also the magnetic rigidity.

Another property of gas-filled separators, which is connected with the rigidity, is the dispersion in the focal-plane. The focal-plane can be considered as the focus of the separator, where spatial distribution of the reaction products is minimal. The focal-plane is the place where the detector or the RTC (Recoil Transfer Chamber)-window (in case of a chemistry separator experiment) is installed. The dispersion defines the change of the rigidity with a certain change in the position in the focal-plane ($\frac{\Delta x}{\Delta B\rho / B\rho}$). It describes the range in magnetic rigidity, which is covered by the detection system. Its unit is centimeter per percent change in magnetic rigidity ($\frac{cm}{\%}$). Since it is not so easy to calculate the magnetic rigidity of the reaction products with small errors, a small dispersion is preferred to get the fusion products in the detection system. This is the case for the DGFRS and TASCA for example, so that these devices are very useful for superheavy element synthesis experiments.

The separation inside of the gas-filled separator happens due to different magnetic rigidities of the fusion products, transfer products, scattered target atoms, and the beam, as can be seen in equation 2.3. For the reaction $^{48}\mathrm{Ca} + {}^{244}\mathrm{Pu} \rightarrow {}^{288}114 + 4n$ for example, the ratio between the $B\rho$ for fusion products, target atoms, and beam particles is 1.0 : 0.9 : 0.3. In this context, especially for asymmetric reactions like the latter, where the fusion products and the target atoms have similar rigidities, a large dispersion is favored to obtain an optimal separation. Table 1.3 contains some gas-filled separators, used in SHE experiments. An example for a separator with large dispersion is the BGS, providing a good separation factor and hence lower background also for very asymmetric reactions, like $^{22}\mathrm{Ne} + {}^{238}\mathrm{U} \rightarrow {}^{255}\mathrm{No} + 5n$.

Table 1.3: Comparison of gas-filled recoil separators. Data adopted from [70, 72].

Separator	Configuration	Solid angle [msr]	Bending angle	Max. Bρ [Tm]	Length [m]	Dispersion [cm/%]
DGFRS	DQ_hQ_v	10	23°	3.1	4.3	0.63
GARIS	DQ_hQ_vD	22	45°	2.2	5.8	0.78
BGS	Q_vD_hD	45	70°	2.5	4.6	1.80
RITU	$Q_vDQ_hQ_v$	10	25°	2.2	4.7	1.00
TASCA (HTM)	DQ_hQ_v	13.3	30°	2.4	3.5	0.90
TASCA (SIM)	DQ_vQ_h	4.3	30°	2.4	3.5	0.10

The reason for the larger dispersion and hence separation of the BGS compared for example with the DGFRS is the design of the separator. While the DGFRS has a traditional DQ_hQ_v setup with a bending angle of 23° of the dipole, the BGS has a Q_vDD design with a bending angle of 70°.
The main part of a gas-filled separator is an arrangement of magnetic dipole and quadrupole magnets around a gas-filled chamber (see Figure 1.18). While the dipole magnet is responsible for the separation itself and should be installed as close as possible to the target to get maximum acceptance, the quadrupole magnets are used for focusing the fusion products into the focal-plane afterwards. Due to the magnetic field inside, a quadrupole magnet is only able to focus vertically or horizontally, depending on the direction of the electric current inside. Hence, in most separators, they are used in doublets, to obtain optimum focusing in both directions.

Some devices are using an extra quadrupole for horizontal focusing before the dipole to increase the acceptance of the dipole, like GARIS II or RITU. In the latter case, an increase of 30% has been observed for asymmetric reactions compared with the tradi-

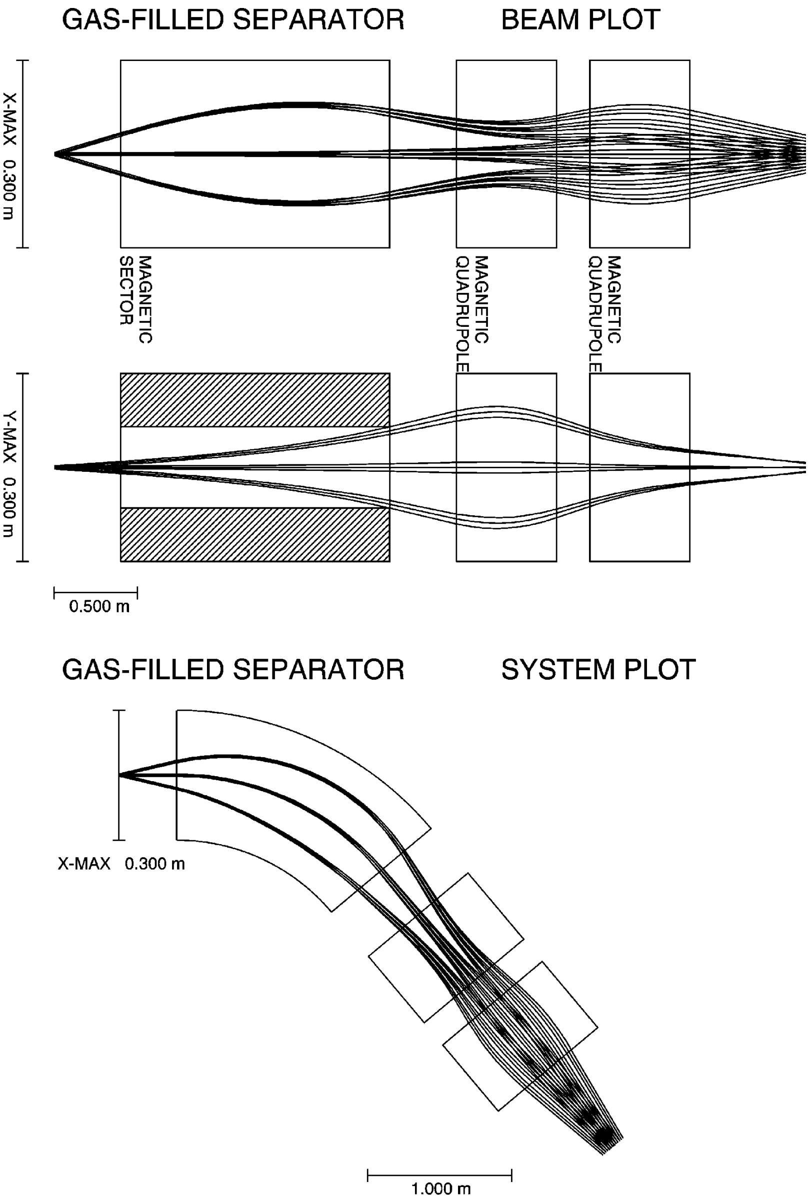

Figure 1.18: Schematic layout of a gas-filled separator consisting of a horizontally focusing dipole magnet (left side) and a quadrupole doublet (right side). Particle trajectories are shown for three different $B\rho$-values starting from three target positions for three angles. Adopted from [73].

tional DQQ configuration [70].

Besides the magnet arrangement, the chosen gas and its pressure are key characteristics of a separator. In principle, there are two kinds of gases which are useful for operation, hydrogen, helium, and a mixture of them. While the separation of transfer products is better with hydrogen, higher field strengths are required in this situation [74]. So most separators, especially those which cannot provide such high fields, use helium instead, which needs lower field strength for the operation.

TASCA for example can be used with both gases, but with hydrogen only to a lower maximum rigidity compared with helium. Only the DGFRS can be operated with pure hydrogen for all reaction products due to its very high maximum magnetic rigidity of 3.1 Tm. A third key feature of gas-filled separators is the isolation of the filling gas from the beam line. The traditional approach, which is used in the BGS or the DGFRS is the installation of an entrance window in front of the target from the beam line. The disadvantage of such a window is the additional energy loss of the projectiles, causing a wider energy distribution of the fusion products and hence less efficiency of the separator. A new development in this field is the application of windowless operation by differential pumping, which has been applied first at RITU and is used nowadays also at GARIS and TASCA. This concept consists of several pumps divided by collimators, making a window unnecessary.

1.6 Chemistry of SHE

1.6.1 Introduction of chemical properties of SHE

Chemical properties and the chemical behavior of all elements can be classified, systematized, and compared using the periodic table, discovered by Dmitri Mendeleev and independently by Lothar Meyer in 1869. The position of elements is defined by their electronic configuration and hence by their proton number. Many unknown elements have been found due to a missing element in that table and precise predictions about their chemical properties and the chemical behavior could be made according to their predicted position in the periodic table.

During the last decades, the validity of the periodic table has been tested by synthesizing heavier and heavier transuranium elements. Each new element fitted quiet well in its respective group and its chemical behavior followed the trend of its lighter homologues. This is not self-evident, due to the fact that the chemical properties of the heaviest elements can vary from their lighter homologues, because the electronic configuration in the ground state can differ for elements within one group. The electronic structure of SHE is influenced by relativistic effects, which are caused by the extremely high, relativistic velocities of the inner and also outer electrons due to the very high nuclear charge, creating an extremely strong electric field. The relativistic velocities cause an increase in the electron mass as

$$m = \frac{m_0}{\sqrt{1 - (\frac{v}{c})^2}} \tag{1.35}$$

where m_0 is the electron rest mass, v is the electron velocity and c is the speed of light. One consequence is a decrease of the effective Bohr radius for s orbitals.

$$a_B = \frac{\hbar^2}{mc^2} \tag{1.36}$$

This contraction of the s and $p_{1/2}$ orbitals due to relativistic effects results in a better shielding of the central nuclear charge, so that the outer orbitals (d and f) are less affected by the nuclear charge and hence become more expanded and destabilized.
Therefore, for heaviest elements some deviations from trends of lighter homologues within one group can be expected, due to very strong relativistic effects on the valence electron shells. Thus, theoretical studies, based on relativistic quantum theory and quantum-chemical methods become extremely important for predictions of experimentally studied properties of heaviest elements. In combination with extrapolations from the periodic table, they are very valuable for designing experiments dealing with only a few single atoms.

As mentioned before, superheavy nuclei become less bound with increasing nuclear charge due to the repulsive electrostatic force of the protons. Hence, the production cross section and production rates drop rapidly with increasing nuclear charge. For element 108, hassium, for example, at maximum only a few atoms can be produced during one week of experiment under optimal conditions. Chemical experiments can only be performed with superheavy isotopes with half-lives of at least half a second or larger. If the half-life is of the order of seconds, there are some fast chemical techniques, which can be used. One of these is based on the principle of gas chromatographic separations utilizing differences in the volatility. Also differences in K_D for SHE, actinides, and lighter transactinide elements are important for clean separations. E.g. aqueous phase chemistry by solvent extraction or ion exchange separations can be applied.
Superheavy elements from 104, Rf to 108, Hs as well as 112, Cn and their chemical behavior have been studied using these techniques. An overall review of these techniques and experiments can be found in the book "The Chemistry of Superheavy Elements" edited by M. Schädel [53].

Due to low production rates and short half-lives, only some basic properties can be measured, like the absorption enthalpy of an atom or a compound on various chromatographic surfaces, or the distribution coefficient or a charge of a complex on an ion exchange resin. Fortunately these properties give an answer to the question, if a new element behaves similarly to its lighter homologues in the chromatographic separation process or not.

1.6.2 Hs chemistry

Due to its electronic configuration, element 108, hassium, is predicted and was demonstrated for the first time in [7] to belong to group 8 of the periodic table. It is a homologue of (Fe), Ru, and Os. Ru and Os are the only elements known, which are able to form a state with an oxidation number 8+, with the exception of Xe, which is known to form a highly unstable and explosive tetroxide (XeO_4). If Hs follows the trend of its lighter homologues, it should form a tetroxide (HsO_4). If furthermore HsO_4 behaves similarly to RuO_4 and OsO_4, its high volatility can be used for an effective separation of this element from many unwanted non-volatile reaction products.

This separation mechanism was indeed used in several experiments on highly efficient chemical separations of Hs. In 1985, experiments aimed at searching SF decaying isotopes of element 108, produced in the heavy-ion induced complete fusion reaction $^{40}\mathrm{Ar} + {}^{235}\mathrm{U}$ (CN=^{275}Ds), were performed at FLNR, Dubna [75]. In another experiment using the complete fusion reaction $^{22}\mathrm{Ne} + {}^{249}\mathrm{Cf}$ (CN=^{271}Hs) at a lab energy of 123 MeV, an α or SF decaying ^{267}Hs produced via the $4n$ evaporation channel was searched for, which was believed to have a half-life of the order of 1s [75, 76]. In previous test experiments with Os, OsO_4 was efficiently absorbed on silicon detectors covered by a Pb layer. However, the main experiment was not sensitive enough to detect Hs events.

Another setup called Online Separation and Condensation AppaRatus (OSCAR) was installed at the 88-inch cyclotron in Berkeley in the year 1987 [77, 78]. OSCAR was used for searching α-decaying ^{272}Hs, which was expected to be the EC daughter product of ^{272}Mt. The efficiency for the separation and condensation of osmium was 36 %, measured in test experiments. Also in this main experiment, no Hs events could be detected and an upper limit for the production cross section of 1 nb was established.

The first successful experiment on Hs chemistry was performed at the GSI Darmstadt in the framework of a large international collaboration in 2001 [7] using the complete

nuclear fusion reaction ^{26}Mg + ^{248}Cm at a beam energy of $E_{lab} = 145$ MeV. A schematic drawing of the experimental setup is shown in Figure 1.19.
Nuclear reaction products recoiling from the target were thermalized in a gas volume of the IVO device [79] and flushed with a dry helium + oxygen mixture, which was used as a carrier gas. The reaction products passed a quartz column filled with a quartz wool plug, which was heated up to 600 °C and which served as a filter for aerosol particles. This plug provided at the same time a surface to complete the oxidation reaction of Hs to hassium tetroxide (HsO_4). These molecules were further transported by the carrier gas jet through a PFA capillary to a detection system. Due to its high volatility, HsO_4 can only be adsorbed by physical adsorption (physisorbtion), in which the forces involved are intermolecular forces (Van-der-Waals forces). These are of the same kind as those responsible for the imperfection of real gases and the condensation of vapors, and they do not involve a significant change in the electronic orbital patterns of the species involved [80]. Hence, for the adsorption of HsO_4 from the gas phase, thermo chromatography with a negative temperature gradient was used. The chromatographic column, the Cryo OnLine Detector (COLD), also served as detection system for the identification of decaying Hs atoms. COLD consisted of 36 pairs of silicon PIN-photodiodes, mounted at a distance of 1.5 mm, appropriate for the detection of α-particles and fission fragments. Always three diodes were connected as one detection unit. A temperature gradient from -20 °C to -170 °C was established along the detector array. A total of 7 decay chains

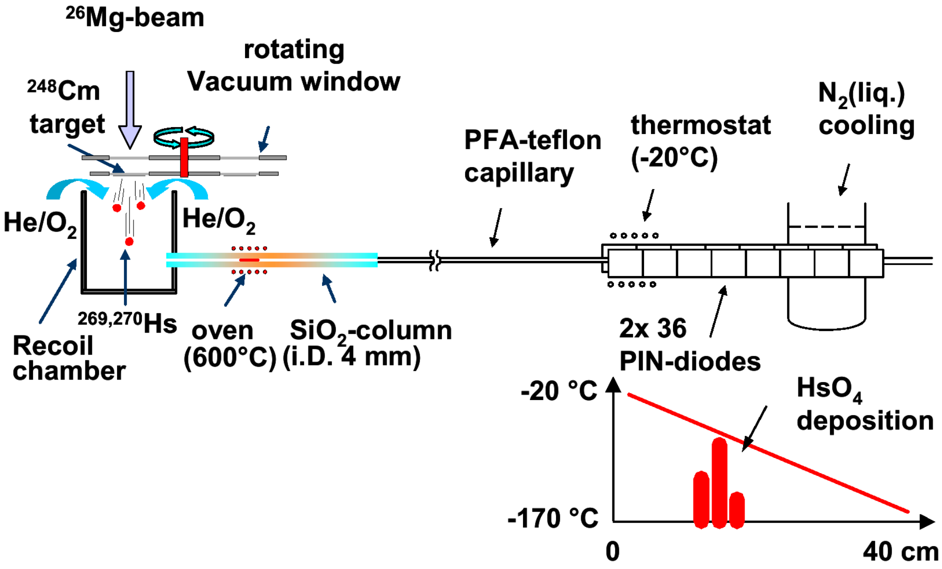

Figure 1.19: Schematic drawing of the experimental setup used in Hs chemistry experiments, which was carried out by Düllmann *et al.* [7].

detected in this experiment were assigned to the decay of ^{269}Hs or tentatively to that of ^{270}Hs [7,63]. The attribution of decay chains to ^{270}Hs was shown to be incorrect in later experiments [8]. However, a very important result of this experiment was the first chemical identification of hassium. From the observed deposition temperature of Hs, which was found to be around -45 °C its adsorption enthalpy was derived to be $-\Delta H_a(\mathrm{HsO_4}) = 46 \pm 2$ kJ/mol and hence confirmed expected chemical properties of Hs as homologue of Ru and Os [81,82].

The next experiment aimed at the investigation of the chemical properties of Hs was a chemistry experiment conducted by A. von Zweidorf *et al.* at the GSI in 2002 [83]. In this experiment the same complete fusion reaction (^{26}Mg + ^{248}Cm) and the same beam energy of E_{lab} = 145 MeV as in the previous experiment [7] was used. Furthermore, the setup used for the chemical separation of Hs was also similar. The only differences were the application of a moisturized carrier gas and the addition of small amounts of ^{152}Gd to the Cm target, to produce short-living Os isotopes, for online monitoring of the experiment. Also, the new detection apparatus CALLISTO (Continuously working Arrangement for cLusterLess transport of In-SiTu produced volatile Oxides) was used. The volatile Os and Hs tetroxides were transported via the gas jet to the detection system, where they were deposited on a surface covered with a thin layer of NaOH due to a neutralization reaction taking place. In analogy to OsO_4, which forms with aqueous NaOH $Na_2[OsO_4(OH)_2]$, an osmate with an oxidation number 8+, HsO_4 presumably was deposited as $Na_2[HsO_4(OH)_2]$, a hassate with an oxidation number 8+ [83]. A detection system consisting of 16 silicon PIN-photodiodes was facing a layer of NaOH, providing the detection of α particles and SF fragments. Overall, six decay chains were assigned to the decay of Hs isotopes. However, due to the 2π detection geometry and the resulting low detection efficiency, mostly incomplete decay chains were measured. Furthermore, the energy of the α-particles was partially degraded in the NaOH layer, resulting in a energy resolution of 80-130 keV (FWHM). Hence, an unambiguous assignment of the observed decay chains was not possible and an unambiguous confirmation of the decay properties of ^{270}Hs was impossible.

Starting from 2003, the new group for chemistry of SHE at the Institute of Radiochemistry (TU Munich) began with the investigation of Hs isotopes near the expected N=162 shell closure, which was predicted by theoretical calculations [6,23,84]. Therefore, precise nuclear data on the decay properties of ^{270}Hs were especially important. Hence, the main goal of two experimental campaigns in 2004 and 2005 at the GSI in the framework of a large international collaboration was to investigate the decay properties of ^{269,270}Hs and their daughters, nuclear reaction studies and the search for new isotopes in the region of interest using the aforementioned COMPACT system. Again, the complete nuclear fusion reaction $^{248}\mathrm{Cm}(^{26}\mathrm{Mg}, xn)^{274-\mathrm{x}}\mathrm{Hs}$ was chosen and investigated at 5 different beam energies. Altogether, 26 genetically linked decay chains originating from Hs nuclei have been observed. Based on 12 decay chains originating from ^{269}Hs, the decay properties of this Hs isotope and its daughters were refined. Furthermore, the decay properties of ^{270}Hs, as well as ^{271}Hs were measured for the first time [51, 52]. The obtained decay properties for ^{270}Hs and ^{266}Sg contradict those measured in previous experiments and an alternative explanation of the previously detected decay properties was presented. Most likely the nuclide ^{270}Hs and its daughter ^{266}Sg were not measured in former experiments and the decay chains attributed to these nuclides originated from isomeric states from ^{269}Hs and ^{265}Sg, respectively [66]. Again, the chemical results of [7] were confirmed.

1.7 Summary and purpose

SHE only exists due to nuclear shell effects enhancing the nuclear stability. In the region of SHE, two centers of stabilization against spontaneous fission exist, around the predicted spherical doubly magic nucleus ^{298}114 and around the deformed doubly magic nucleus ^{270}Hs. Enhanced stability of the latter one has been confirmed in recent experiments. From the measured E_α values of Hs isotopes near N=162 and deduced Q_α systematics, half-lives could be calculated of the order of several seconds for $^{269-271}$Hs.

As described above, the production cross section for the formation of SHE formed in heavy-ion induced nuclear fusion reactions can be described in three stages. First of all, the approaching phase of projectile and target nucleus and the penetration or the overcoming of the Coulomb barrier by the projectile takes place, depending on the beam energy. In the second stage, projectile and target nuclei get into contact with each other and a nucleon flux gets established forming in the end a highly excited compound nucleus (CN) or being interrupted and a reseparation of projectile-like and target-like nucleus takes place. If the CN is formed, it is cooled down by neutron- and γ-emission or it is lost by entering the fission channel in the third stage. To investigate the reaction mechanism, it is necessary to fix as many reaction parameters as possible. Since the capture (first stage) and the de-excitation (third stage) of the EVR production cross section are well understood, these factors should be fixed in order to investigate the fusion probability, which is not satisfyingly understood. Hence the impact of this factor and the parameters influencing it, like the reaction asymmetry or the reaction Q-value should be examined in this work. In a recent publication, the influence of these two parameters on the fusion probability for cold fusion reactions has been studied and qualitatively as well as quantitatively evaluated [41].

The aim of this thesis is to study the Q-value influence on the production of SHE and especially on the synthesis of $^{269-271}$Hs. To do so, there are four different reactions leading to the same CN (^{274}Hs*):

1. $^{248}\mathrm{Cm}(^{26}\mathrm{Mg}, xn)^{274-\mathrm{x}}\mathrm{Hs}$
2. $^{244}\mathrm{Pu}(^{30}\mathrm{Si}, xn)^{274-\mathrm{x}}\mathrm{Hs}$
3. $^{238}\mathrm{U}(^{36}\mathrm{S}, xn)^{274-\mathrm{x}}\mathrm{Hs}$
4. $^{226}\mathrm{Ra}(^{48}\mathrm{Ca}, xn)^{274-\mathrm{x}}\mathrm{Hs}$

These differ in their (B-Q)-value and hence in their Q-value as well as in their reaction asymmetry.
Recently, the formation of deformed doubly-magic ^{270}Hs in the $4n$ evaporation channel in the complete fusion reactions $^{248}\mathrm{Cm}(^{26}\mathrm{Mg}, 4n)^{270}\mathrm{Hs}$, $^{244}\mathrm{Pu}(^{30}\mathrm{Si}, 4n)^{270}\mathrm{Hs}$, $^{238}\mathrm{U}(^{36}\mathrm{S}, 4n)^{270}\mathrm{Hs}$, and $^{226}\mathrm{Ra}(^{48}\mathrm{Ca}, 4n)^{270}\mathrm{Hs}$ has been studied theoretically in more detail using a two-parameter Smoluchowski equation [43]. Simple entrance channel arguments make CN formation appear favorable for systems with larger mass asymmetry [85]. However, due to a lower reaction Q value, the reactions $^{238}\mathrm{U}(^{36}\mathrm{S}, 4n)^{270}\mathrm{Hs}$ ($\sigma_{theo} = 24$ pb) and $^{226}\mathrm{Ra}(^{48}\mathrm{Ca}, 4n)^{270}\mathrm{Hs}$ ($\sigma_{theo} = 30$ pb) are predicted to have higher cross sections compared to the reactions $^{248}\mathrm{Cm}(^{26}\mathrm{Mg}, 4n)^{270}\mathrm{Hs}$ ($\sigma_{theo} = 12$ pb) and $^{244}\mathrm{Pu}(^{30}\mathrm{Si}, 4n)^{270}\mathrm{Hs}$ ($\sigma_{theo} = 8$ pb) [43]. A maximum cross section for the $^{226}\mathrm{Ra}(^{48}\mathrm{Ca}, 4n)^{270}\mathrm{Hs}$ reaction of about 30 pb was also predicted in other calculations, using a different method, [41] which has been shown to reproduce experimental cross sections for various ^{48}Ca-based fusion reactions with actinide targets.

The main aim of this work was to investigate the most promising reactions $^{238}\mathrm{U}(^{36}\mathrm{S}, xn)^{274-\mathrm{x}}\mathrm{Hs}$ and $^{226}\mathrm{Ra}(^{48}\mathrm{Ca}, xn)^{274-\mathrm{x}}\mathrm{Hs}$ and to compare them with the already measured reaction $^{248}\mathrm{Cm}(^{26}\mathrm{Mg}, xn)^{274-\mathrm{x}}\mathrm{Hs}$ to verify or falsify the theoretical reaction studies, mentioned above. Furthermore, the main parameters, which are the aforementioned asymmetry and the (B-Q)-value, affecting the fusion probability of the EVR cross section most, should be examined and evaluated.

As shown by Düllmann *et al.* [7], a chemical separation of Hs is very efficient. Hence, chemical separation and detection systems can be applied to produce these isotopes, especially ^{270}Hs, very efficiently in complete nuclear fusion reactions. This technique was applied in the reaction $^{238}\mathrm{U}(^{36}\mathrm{S}, 4n)^{270}\mathrm{Hs}$, which was investigated in a two week experiment performed at the GSI in 2008 using the chemical separation and detection system COMPACT. The reaction $^{226}\mathrm{Ra}(^{48}\mathrm{Ca}, 4n)^{270}\mathrm{Hs}$ was examined in two experimental campaigns in 2008 at the Dubna Gas-filled Recoil Separator (DGFRS) at FLNR in Dubna by the DGFRS-group in collaboration with the Institut für Radiochemie (TU München).

Chapter 2

Experimental setup

2.1 Overview

Nuclear fusion reactions at the end of stability in the transactinide region are characterized by very low fusion-evaporation cross sections in the order of pb or even fb compared with other nuclear reactions like nuclear transfer reactions. These reactions deal with cross sections in the order of μb or even mb resulting in a very high yield of background in superheavy element experiments. Due to this huge amount of unwanted reaction products, efficient online or offline separation methods, depending on the half-lives of the fusion products, have to be applied in order to detect the produced superheavy evaporation residues.

In the last five decades several approaches have been used to make the separation more efficient. One technique is to filter the produced nuclei according to their velocity by a Wien filter, which has been realized for example with the "SHIP" separator at the GSI or the Vassilissa separator at the FLNR in Dubna. These separators use electric and magnetic fields to let only nuclei with a certain velocity pass to the focal-plane.
Another approach is the gas-filled separator, which is realized for example with the Berkeley Gas-filled Separator (BGS) [86], the Dubna Gas-filled Recoil Separator (DGFRS) at the FLNR in Dubna [87] or TASCA [72] installed at the GSI. These devices consists of a dipole magnet and in most cases followed by a set of two quadropole magnets for focusing, which all are filled with a light gas with low pressure. The reaction products are deflected inside of the dipole magnet according to their A/q ratio in the energy region we are using in our experiments.

Electromagnetic separators are not element specific and hence suited for all SHE, as long as their half-life is longer than the time-of-flight inside of the separator, which is in the order of μs. This is the case for all known SHE ($Z<119$). A detailed introduction of kinematic separators for superheavy element experiments can be found in Section 1.5 and especially the DGFRS is presented in Section 2.3.

A completely different approach is the separation due to the chemical behavior of the fusion products. This technique has been applied for a separation of new elements in transuranium synthesis experiments produced in neutron capture reactions and has been used during the last decades in experiments on the chemistry of SHE. Being absolutely element specific is a unique key feature and the main advantage of chemistry as separation technique. In principle, chemistry can be applied for any superheavy element, if the isotopes under study are long-lived enough for a selected chemistry approach. But along with the isolation and identification of SHE nuclides, chemical studies provide additional information about chemical properties of new chemical elements.

In our case, we applied a gas phase thermo chromatography method, utilizing the chemical behavior of hassium of forming a very volatile tetroxide, to separate it from most all other reaction products with a very high efficiency. The experimental setup is based on the same concept as described in [7, 63]. This chemical method can be used in the case of hassium, because its half-life of about 10 seconds is much longer than the time needed for chemical reaction, separation and transport, which is altogether about two seconds. Hence it is possible to separate hassium fast and effectively by chemical means from target like elements or those produced in nuclear transfer reactions. A more detailed discussion and description of SHE gas phase thermo chromatography experiments for hassium can be found in Section 2.2

2.2 Chemistry experiments

2.2.1 Overview

The position of an element in the periodic table and, hence, its chemical properties, are defined by the atomic number of an element. Thus, they are dependent on the number of electrons and electronic structure caused by the nuclear charge, the proton number. Therefore, different atoms can be separated by chemical processes due to differences of their valence electron structure depending on the proton number. In the history of the synthesis of transuranium elements, the separation from target atoms or unwanted byproducts was performed using chemical methods. These methods can be very selective for one selected element and are able to separate the wanted SHEs from unwanted reaction products.

The number of α-active transactinide isotopes with half-lives suitable for chemical studies is quite high. However, the spectrometric detectors for measuring α-particles or fission fragments are sensitive to the high neutron flux nearby the target. In addition, they do not withstand elevated temperatures and active chemical reagents. Hence, the reaction products must be transported several meters away from the beam stop. Thus, a thermalization of the reaction products in the gas volume of a recoil chamber combined with a following transport with a gas jet through a capillary directly to a gas chromatographic system is necessary [88].

All chemical experiments with transactinides can be separated in two groups, experiments in the gas phase and experiments in the liquid phase. An enhanced separation efficiency and selectivity from unwanted byproducts can be achieved in liquid phase experiments. The main disadvantages of this technique are a longer separation time and a lower detection efficiency.

Gas phase separation procedures are fast, efficient and can be performed continuously, resulting in a high overall yield. Finally, nearly weightless samples can be prepared on thin foils or directly on the detector surface, which provides α- and SF-spectroscopy of the separated products with a good energy resolution and in a high, nearly 4π detection geometry.

Despite the fact that only few inorganic compounds of the transition elements exist, that are appreciably volatile below temperatures of about 1000 °C, which is a experimentally manageable temperature, gas-phase chemical separations played and still play an important role in chemical investigations of transactinide elements. A very detailed introduction to this field can be found in [27, 88].

Gas phase chemistry experiments are based on the principle of gas-solid chromatography. A separation of volatile species occurs due to the repeated interaction of a volatile compound or atom, transported by a gas jet through the chromatographic column on the one side and the column surface as the stationary phase on the other side. For experiments investigating the chemical properties of transactinide compounds, two different types of chromatographic separation have been developed. Thermo chromatography (TC) and isothermal chromatography (IC). Using TC [89], which has been applied in this work, a carrier gas is flowing through a chromatographic column, to which a negative temperature gradient has been applied. Species, that are volatile at the starting point (temperature at the entrance of the column) are transported downstream of the column by the carrier gas flow. The decreasing temperature in the column results in an exponentially increasing time the species spend in the adsorbed state. Different species form distinct deposition peaks at a temperature T_a corresponding to the maximum of the peak, depending on their adsorption enthalpy ΔH_a on the column surface and are thus separated from each other.

The experimental setup used for the reaction $^{36}S + ^{238}U$, based on TC, is similar to that described in [7, 63]. A schematic drawing of this experimental setup is displayed in Figure 2.1.

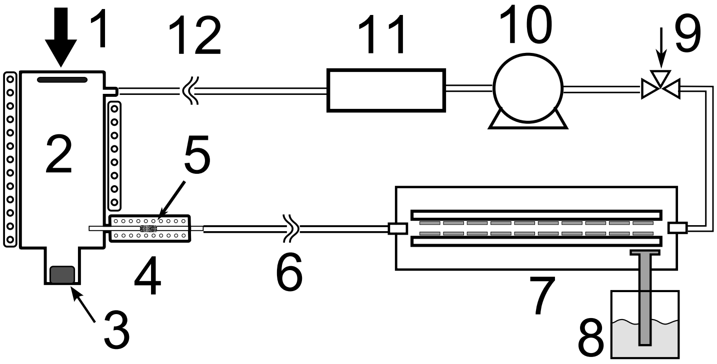

Figure 2.1: Schematic drawing of the experimental setup: (1) heavy ion beam, (2) heated recoil chamber with target, (3) beam stop, (4) oven, (5) quartz filter, (6) PTFA capillary for gas transport to detector, (7) COMPACT detection system with 2 × 32 PIPS detectors, (8) liquid nitrogen cooling, (9) gas mixture and flow control, (10) membrane pump, (11) NYAD^{TM} dew point measurement device, (12) gas inlet into the recoil chamber. Adapted from [8].

A beam of ^{36}S-ions was impinged on a rotating ^{238}U target. Nuclear fusion products, that recoiled out of the target were thermalized in a He/O_2 gas mixture inside of the heated recoil chamber (RC). Recoiling products were partially oxidized already in the partial oxygen atmosphere inside of the RC. A gas flow flushed the RC and transported volatile species to a quartz wool plug arranged inside an oven. This plug served as a filter for aerosol particles and provided a surface to finalize the oxidation reaction. Hence, all non-volatile species were effectively separated from volatile species like HsO_4, OsO_4, Rn, and At, which passed through the filter and were transported through a PTFE (PolyTetraFlouroEthylene) capillary to the detection system COMPACT (Cryo On-line Multidetector for Physics and Chemistry of Transactinides). COMPACT is a system which provides the separation and detection of at room temperature volatile species by measuring their nuclear decay properties. The separation inside the detector is based on the principle of TC [90]. The carrier gas was circulated in a loop. Flow and pressure of the gas were automated and controlled remotely. The moisture of the gas was continuously measured by a NYAD^{TM} dew point measuring device. To keep the moisture as low as possible to avoid water condensation inside of COMPACT, the gas mixture was dried in drying cartridges as well as in a moisture trap. A more detailed discussion of COMPACT can be found in Section 2.2.4.

2.2.2 Preparation of $^{36}SO_2$

^{36}S (natural abundance 0.01 %) is a very expensive material. About 2 g of ^{36}S was provided by the GSI in elemental form. It was oxidized to $^{36}SO_2$ gas and condensed inside of several flasks in a laboratory of the Institut für Radiochemie (TU München) in Garching, Germany. This oxidation was necessary, since ^{36}S is a very expensive material and had to be utilized in a safe and efficient way by the ion source.

The sulfur material (a powder in elementary form with 80% enrichment) was melted in a quartz glass boat at a temperature of about 160 °C and afterwards placed inside of a glass "T" part with KF flanges. Through the top flange a glow filament was implemented, and the other flanges were used as gas inlet and outlet. Three flasks made from stainless steel were connected in series with surrounding cooling mantles made from copper tubes. The flasks were covered inside with PTFE and each of them had two valves at both sides. The whole vacuum tight system was first pumped down to 10^{-3} mbar and then flushed with helium. The flasks were cooled down to -140 °C by liquid nitrogen vapor flowing through the copper cooling tubes. Afterwards the helium flow was switched to an oxygen gas flow of $\approx$50 ml/min. The oxygen gas was purified from water content by molecular sieves. The glow filament was used to ignite a self supporting combustion of the sulfur material. The complete oxidation was finished after 10 min (see Figure 2.2). At the exit from the third flask, the outgoing gas was guided through a glass flask filled with a NaOH solution. This was used as a trap for SO_2. No sulfur has been found inside the trap. The content of condensed $^{36}SO_2$ has been measured in all three flasks after the oxidation process has been completed. More than 80% of produced $^{36}SO_2$ have been found in the first flask, while 16% have been condensed in the second flask and 2.3% in the last one, respectively. The total conversion yield was 99%. Afterwards the flasks were heated up to equilibrate the gas pressure. Then each flask was closed from both sides and disconnected separately [91].

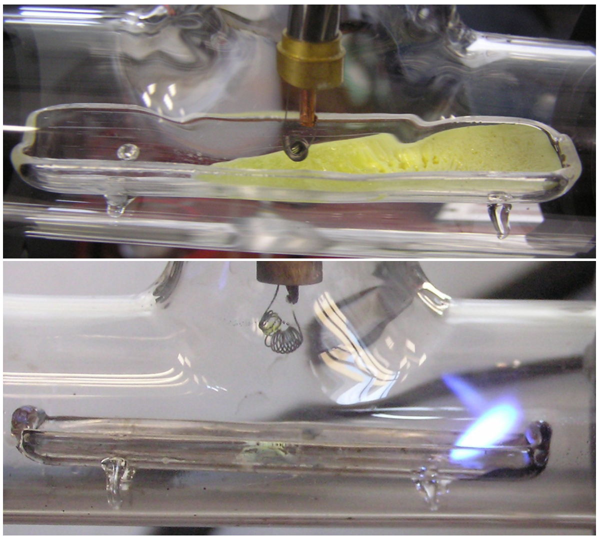

Figure 2.2: Quartz boat with elementary ^{36}S before and during the combustion process. Adapted from [91].

2.2.3 Irradiation Setup

The experiment was performed in a two week campaign in May 2008 at the GSI Helmholtzzentrum für Schwerionenforschung (GSI) in Darmstadt, Germany. The GSI is an accelerator centre in the heart of Germany and may provide beams from ^{12}C to ^{238}U for various experiments and applications in nuclear and particle physics. For our purpose, the UNILAC (UNIversal Linear ACcelerator) was used, since it is the most suitable accelerator at the GSI for low energy nuclear physics experiments with high currents. Behind the UNILAC, three beam line branches are arranged in the experimental hall, X, Y, and Z. The Z branch is among other applications used as the connection beam line between the UNILAC and the heavy ion synchrotron SIS (Schwerionensynchrotron) which is used for particle physics experiments and which will be used in future as pre-accelerator for FAIR (Facility for Antiproton and Ion Research). In the Y branch, the velocity separator SHIP is situated. Our experiment was performed in the X branch of the experimental hall in cave X1, the closest one to the UNILAC. Inside of X1 various experiments on chemical and decay properties of SHE have been performed. During the experimental campaign in May 2008, using a chemical separation setup, a beam of ^{36}S^{5+} ions from an ECR (Electron Cyclotron Resonance) source was provided by the UNILAC accelerator. The UNILAC is able to provide beams of accelerated ions of elements from carbon to uranium with energies up to 20 MeV/u. The beam is pulsed with a 25 % duty cycle and a pulse length of about 5 ms.

The ECR source was chosen, because of its very low consumption compared with other types of sources. Inside of the ECR the $^{36}SO_2$ was converted to a plasma state and the $^{36}S^{5+}$ ions were guided out of the source and injected into the UNILAC. With its high frequency resonators and the Alvarez structures, ^{36}S was accelerated up to E_{lab} = 256.4 MeV (corresponding to 7.13 MeV/u [92]), which was used during the whole experiment, and impinged on a rotating ^{238}U target. Typical beam intensities were 350 particle nA ($2.2 \cdot 10^{12} s^{-1}$). The beam intensity was measured with a transformator in front of the target and with a beam stop at the back wall of the RC. By exchanging the RC by a faraday cup (under vacuum) followed by an irradiation of the target, the measured transformator currents could be calibrated for a precise measurement of the beam integral. A picture of the mounted faraday cup can be found in Figure 2.3. These faraday cup measurements were performed several times during the experiment.

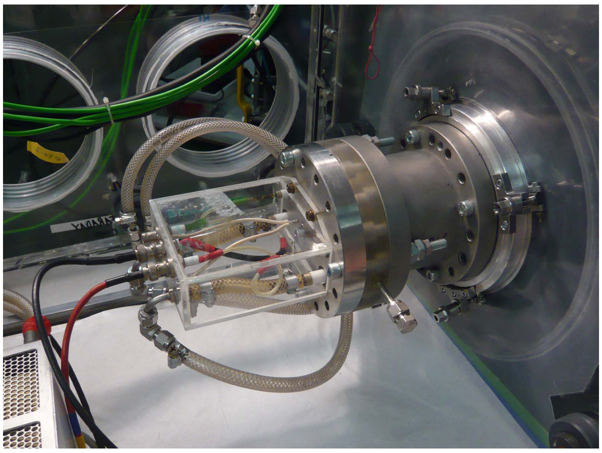

Figure 2.3: Picture of the faraday cup mounted periodically for exact beam current measurements.

In combination with two sets of targets with different thicknesses, the complete nuclear fusion reaction $^{36}S + ^{238}U$ was investigated at two beam energies inside of the targets. In the first target set, the beam energy was $E_{lab} = (179.5 \pm 4.5)$ MeV, corresponding to an excitation energy of $E^* = (39 \pm 4)$ MeV. According to HIVAP [44] calculations, this value is close to the maximum of the $4n$ channel (see Figure 1.12). Also, the predicted maximum of the calculated $4n$ excitation function from [43] is very close to that energy (see Figure 1.9). Inside of the second target the beam energy was $E_{lab} = (193.5 \pm 3.5)$ MeV, which corresponds to an excitation energy of $E^* = (51 \pm 3)$

MeV. This value is close to the maximum of the $5n$ channel (see Figure 1.12). Both target sets are composed of an about 20.2 μm Be vacuum window and a 6 mm He/O_2 gas volume, followed by the Be backing.

The target material of the first target set (TR1) was deposited on a 12.6 μm Be backing (corresponding to 2.33 mg/cm^2 Be) and consisted of three arc-shaped $^{238}U_3O_8$ targets of 1.8 mg/cm^2, 1.5 mg/cm^2, and 1.6 mg/cm^2. These targets were produced by molecular plating. A picture presenting the target before and after the irradiation can be found in Figure 2.4.

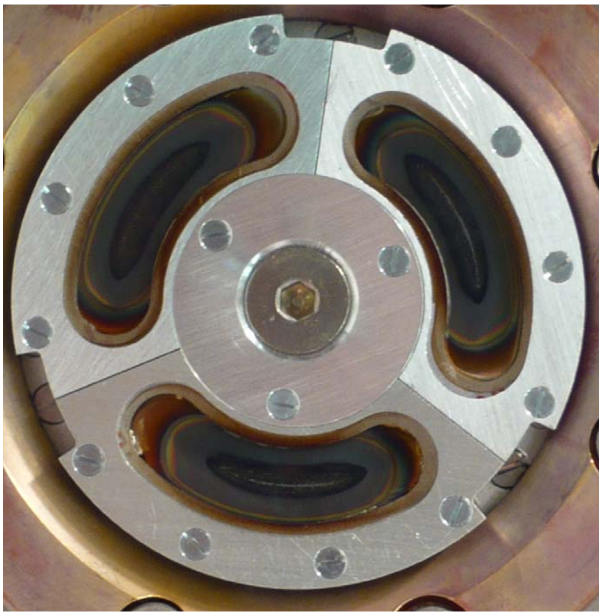

Figure 2.4: Photography of the first ARTESIA target wheel with $^{238}U_3O_8$ targets used in the TUM experiment on Hs chemistry. Photo courtesy of C. E. Düllmann.

This target wheel had been irradiated with $4.2 \cdot 10^{18}$ ^{48}Ca ions prior to our experiment [93]. One of the segments contained 20 μg/cm^2 of ^{nat}Nd for the simultaneous production of α-decaying Os isotopes, a chemical homologue of Hs, for online monitoring of the chemical yield.

The target material of the second target set (TN22) was deposited on a 8.2 μm thick Be backing and consisted of three targets comprising 1.0 mg/cm^2 of metallic ^{238}U each, which has been deposited by sputtering. Pictures of the target before and after the irradiation can be found in Figure 2.5.

Due to the oxygen-containing atmosphere, the targets are expected to start oxidizing

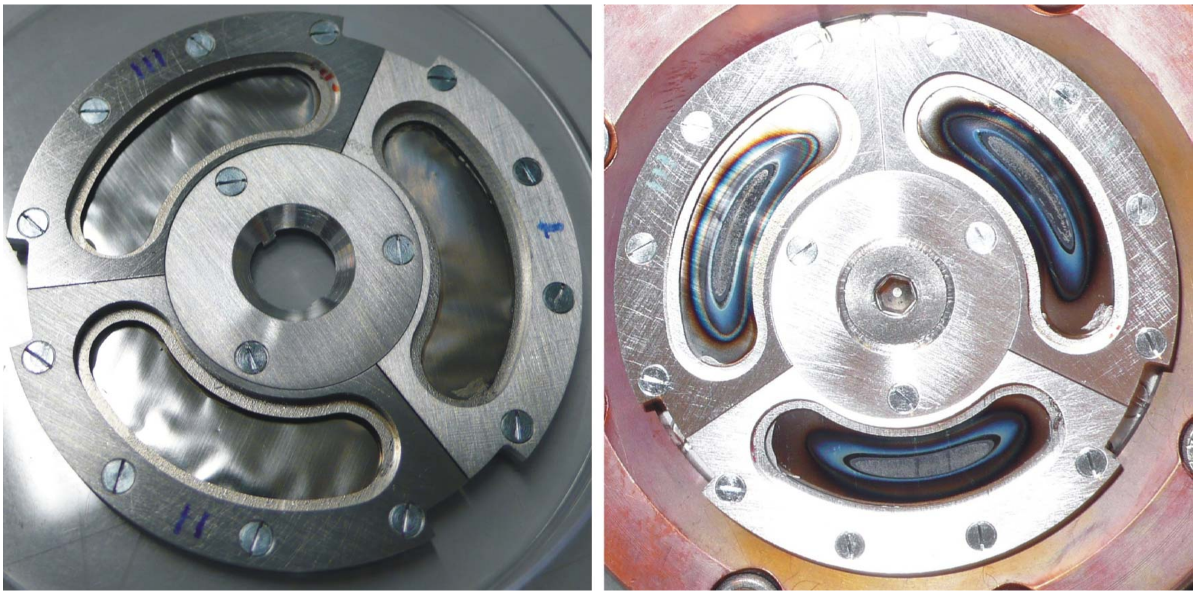

Figure 2.5: Photography of the 2nd ARTESIA target wheel with metallic ^{238}U targets used in the TUM experiment on Hs chemistry. It is shown before (left) and after (right) the irradiation with ^{36}S ions. Photo courtesy of C. E. Düllmann.

during the very first moments of beam irradiation.

Due to the energy loss of the beam in the vacuum window and the target backing a power of 23 W (first target set) respectively 20 W (second target set) was induced by the beam at typical beam intensities during the bombardment. An effective cooling was necessary to prevent damage to the target and the windows due to overheating. Indeed, the target and window resistance against heat and radiation damages is the limiting factor for not increasing the beam intensities even further. In our experiment a rotating target and vacuum window wheel, ARTESIA, was used. Such a technically challenging irradiation setup was constructed and put into operation by M. Schädel et al. [94].

Both target wheels were rotating with 2000 rpm, in synchronization with the beam pulse. The main advantage of such rotating targets is the more effective cooling compared with a stationary target. This is caused due to the spreading of the beam over a larger target area in the case of the rotating target. The detailed composition of each target and segment can be found in Table 2.1.

Both targets were measured after the experiment by α- and γ-measurements as well as by radiography to determine the ^{238}U thickness. These measurements where performed at the Institut für Kernchemie of the university of Mainz by Jörg Runke and Dr. Klaus

Table 2.1: Details of both used target sets in the experimental campaign on the reaction ^{36}S+ ^{238}U.

Segment	Be backing [μm]	target material as	target material thickness [mg/cm^2]
TR1_I	12.5 ± 0.5	$^{238}U_3O_8$	1.6
TR1_II	12.7 ± 0.4	$^{238}U_3O_8$	1.8
TR1_III	12.6 ± 0.3	$^{238}U_3O_8$	1.5
TN22_I	8.2	met. ^{238}U	1.0
TN22_II	8.1	met. ^{238}U	1.0
TN22_III	8.2	met. ^{238}U	1.0

Eberhardt [95]. Both measurements were performed on all segments and one backup segment from the second target set, which has not been irradiated served as a standard. The results of both analyses can be found in Table 2.2.

Table 2.2: Target thicknesses resulting from α- and γ-measurement of all segments of both used targets. Data from [95].

Segment	target material thickness from α-measurement [μg/cm^2]	target material thickness from γ-measurement [μg/cm^2]
TR1_I	1056 ± 53	1332 ± 32
TR1_II	1535 ± 77	1695 ± 36
TR1_III	1418 ± 71	1475 ± 34
TN22_I	1039 ± 52	1062 ± 26
TN22_II	1011 ± 51	955 ± 27
TN22_III	994 ± 50	886 ± 29

During the α-measurements, all segments were measured at a distance of 15 cm to the detector for 24 hours. The γ-spectroscopy was performed with the 186 keV line of ^{226}Ra a daughter of ^{238}U and every segment was measured for 15 hours. These long times were necessary due to the very long half-life of ^{238}U of $4.468 \cdot 10^9$ years. Only in one segment from the first target, a loss of approximately 20% of the target material has been observed.

Examples of spectra from α- and γ-measurement of the standard and segment TN22_I can be found in Figure 2.6 and Figure 2.7. As can be seen, the α-spectra of the irradiated and nonirradiated segments are more or less the same. Both γ-spectra are very similar but new γ-lines can be found in the irradiated sample originating from transfer products created during the ^{36}S bombardment.

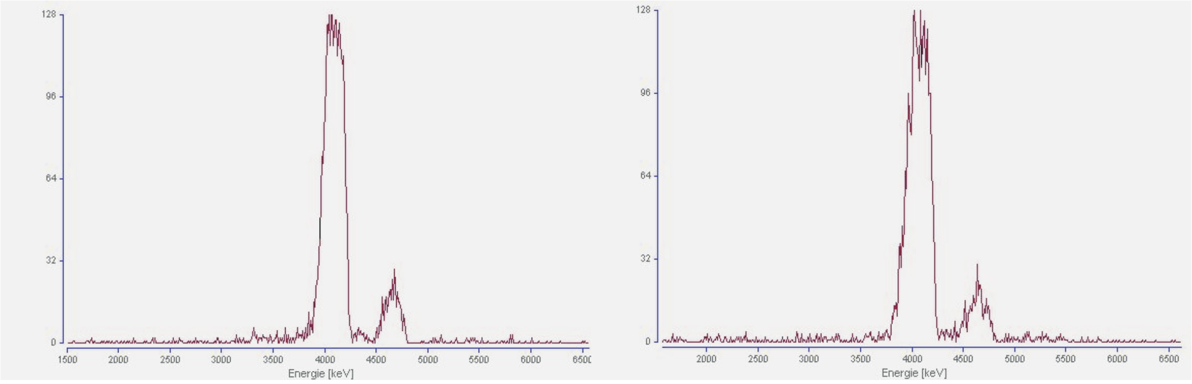

Figure 2.6: α-spectrum of the ^{238}U target standard (left) and of TN22_1 (right) [95].

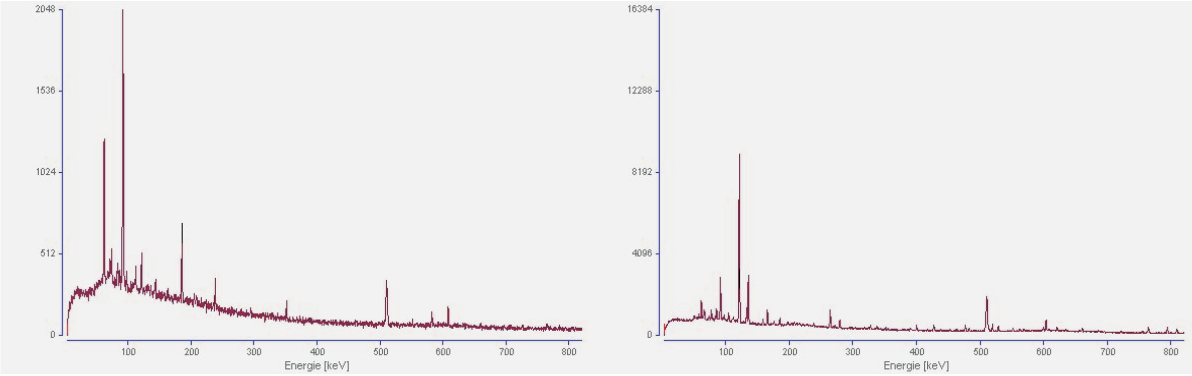

Figure 2.7: γ-spectrum of the ^{238}U target standard (left) and of TN22_1 (right) [95].

Evaporation residues, produced in complete nuclear fusion reactions and recoiling from the target were stopped in the He/O$_2$ gas mixture at 1.1 bar inside of a recoil chamber (see Figure 2.8). The beam passing the layers of the target wheel was stopped in a beam dump. The beam dump consisted of a water cooled copper plate mounted at the end of the RC. The dimensions of the RC and the gas pressure were adjusted for the stopping range of recoiling Hs atoms produced. The RC was flushed with about 1.3 l/min

He/O_2 gas mixture. The oxidation reaction of Hs to HsO_4 was expedited by heating the RC via an external oven up to 350 °C. Volatile products or compounds of products, like HsO_4, OsO_4, Rn, or At, were transported by the gas jet to the quartz wool filter, which was heated by two external ovens to about 550 °C. At this filter, the oxidation process was completed and non-volatile products were caught. The retention time for volatile species was negligible in comparison with the transport time to the detector. The separation factor for separation of volatile species from nonvolatile species was $> 10^6$ [8].

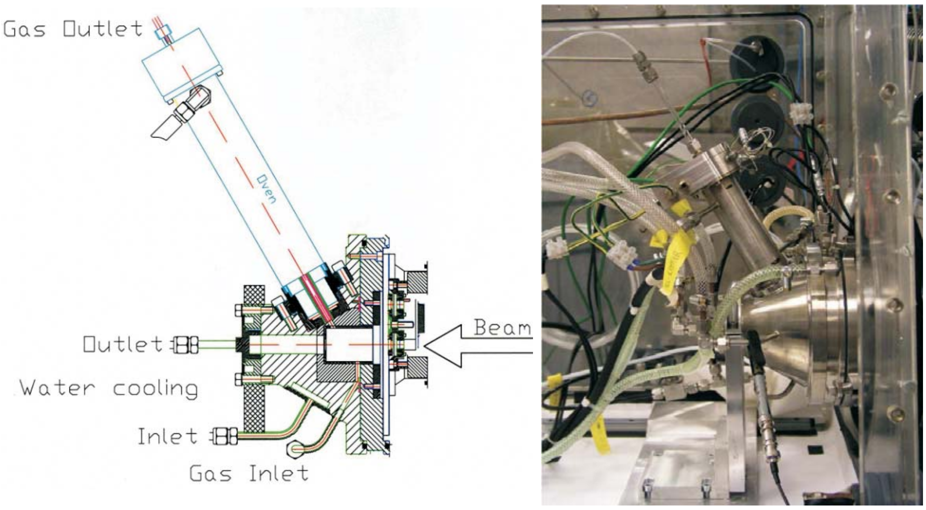

Figure 2.8: Schematic cross section drawing of the recoil chamber. The oven attached to the gas outlet contains the quartz wool filter. Adapted from [27].

Because of the high radiation dose close to the target during an irradiation, the detection setup had to be shielded. This was achieved by placing it behind a two meter thick concrete wall. The length of the transport line from the RC to the detections system was up to eight meters, corresponding to transport times of about two seconds.

2.2.4 COMPACT

The detection system COMPACT (Cryo Online Multidetector for Physics And Chemistry of Transactinides) was constructed particularly for chemical experiments with Hs, as well as with elements 112 and 114. Its commissioning was accomplished in the frame of [8]. COMPACT was constructed as a cryo thermatography detector [79, 90] for the separation and detection of volatile species or volatile compounds of α-decaying superheavy elements. COMPACT , like CTS (Cryo Thermo chromatographic Separator) and COLD (Cryo On-Line Detector) is designed on the one hand as a TC column [96] for separation of volatile species according to their volatility and on the other hand as a detector with 4π detection geometry for the efficient detection of adsorbed molecules and atoms. Along the channel (column), formed by a series of planar silicon diodes, a longitudinal negative temperature gradient is established. CTS, the first TC detector, was constructed by U. Kirbach *et al.* [90] at the Lawrence Berkeley National Laboratory. In the first Hs experiment [7] the improved COLD [79] was used, which had a geometrical efficiency for detecting α-particles emitted by a species adsorbed inside the detector array of 77%. In that experiment the principle of thermo chromatographic separation and detection has been proven by observing the nuclide ^{269}Hs and its decay daughters after chemical isolation.

COMPACT is a more improved TC separation and detection device, with a aforementioned geometrical efficiency of about 4π. Silicon diodes for the detection of α-particles and SF fragments are glued on the inner side of the thermo chromatographic channel to reach a maximal possible geometrical efficiency. A carrier gas is flowing through the TC chromatography column. Volatile elements or compounds are transported through the column downstream by the carrier gas flow. Due to the decreasing temperature in the column, the time the species spend in the adsorbed state increases exponentially. Different species are separated from each other by forming distinct deposition peaks, depending on their adsorption enthalpy (ΔH_a^0) on the column surface.

During this experimental campaign, two similar COMPACT detectors have been used. Due to water adsorption inside of COMPACT the formed ice layer negatively affected the energy resolution of the silicon detectors. Therefore, a heating and drying procedure has to be applied. To provide a continuous measurement during the experiment, two COMPACT units were operated alternately. The TC column consisted of two arrays of 32 passivated Implanted Planar Silicon (PIPS) detectors, which were facing each other at a distance of 0.5 mm, embedded in a two-part Invar$^{\text{TM}}$ enclosure. The two panels were joined together and sealed with 1 mm In-wire, forming a vacuum tight gas channel. The gas carrying volatile species flowed through the 0.5 mm wide gap formed between the panels. Schematic drawings of the arrangement of the PIPS detectors in the Invar panel$^{\text{TM}}$ are shown in Figure 2.9, Figure 2.10, and Figure 2.11.

Electrical feedthrough contacts were welded into the Invar panels and sealed with epoxy. The PIPS diodes were designed and manufactured at the Institute of Electron Technology, Warsaw. The diodes used in this experiment were an enhanced version of

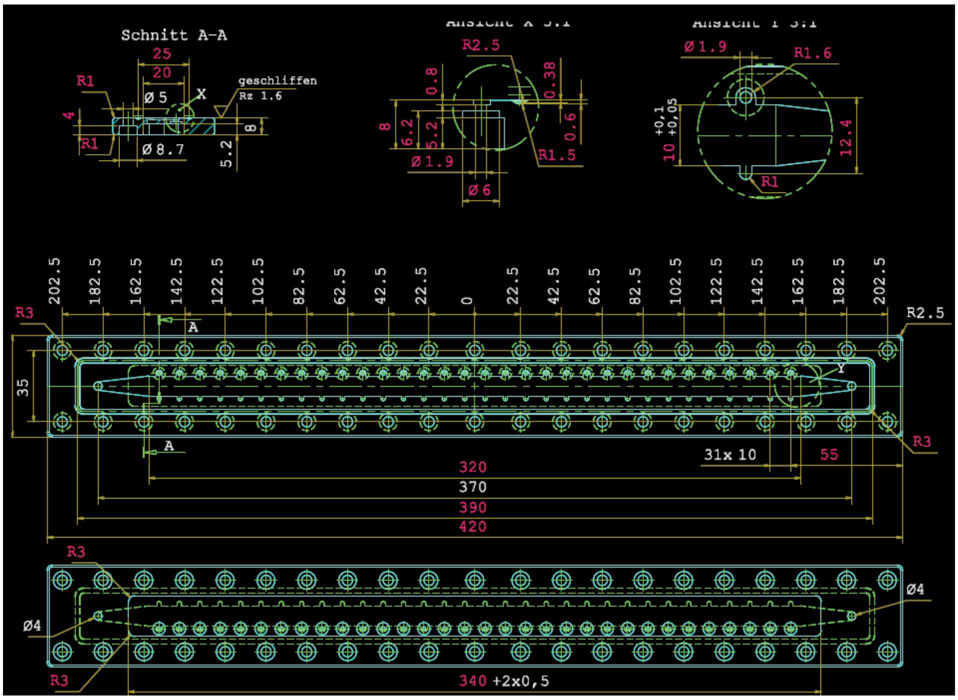

Figure 2.9: A drawing of a bottom detector panel with gas inlet/outlet. Picture adopted from [27].

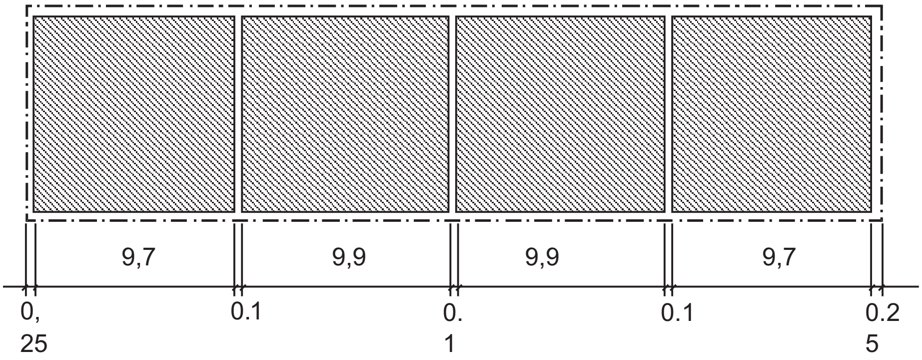

Figure 2.10: New detector chip 10 x 40 mm^2 with 4 single photodiodes. Picture adopted from [27].

those used in former Hs chemistry experiments [8] characterized by an increased detection efficiency. A photograph of one Invar panel with glued-in PIPS detectors can be found in Figure 2.12.

They were 300 μm thick epitaxial silicon PIN diodes with a 120 μm thick active layer, sensitive for α-particles and fission fragments. The active area of a PIPS diode

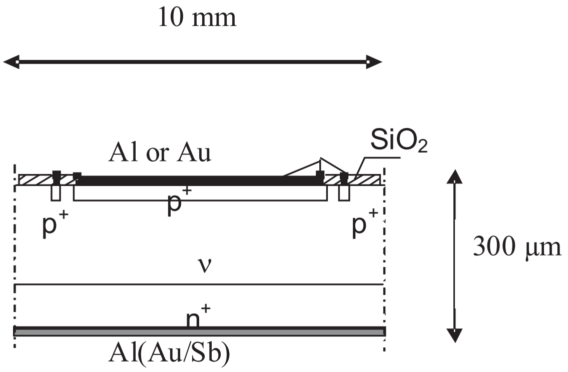

Figure 2.11: Schematic drawing of a PIN photodiode made at ITE Warsaw. Picture adopted from [27].

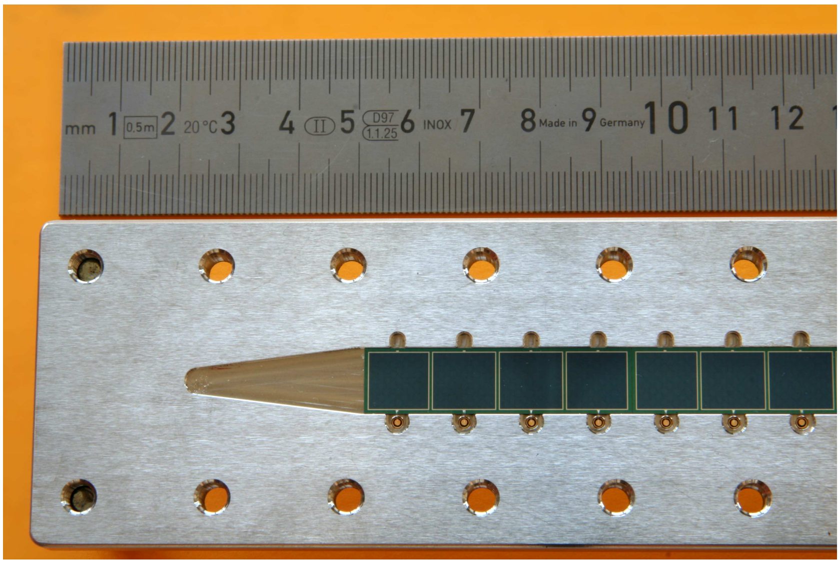

Figure 2.12: Photograph of one Invar panel with glued-in PIPS detectors. Picture adopted from [27].

was 9.7×9.8 mm^2. Four diodes were suited on one Si chip at a distance of 0.1 mm to minimize the inactive surface. The surface of the diodes can be covered with a thin layer of various materials depending on the chemical properties of the element or compound to be investigated. The nearly 4π detection geometry yielded a very high detection efficiency, necessary for the investigation of SHE. The probability for detecting an α-particle emitted from a species deposited anywhere in the detector channel, including non-active surface of diodes and channel sides, was 86% and the probability for detecting at least one fission fragment of such a species was 94%. The analysis of the detection efficiency is presented in Chapter 3. The detectors were calibrated off-line with ^{219}Rn and its α-decaying products emanating from an ^{227}Ac source. The energy resolution was better than 50 keV (FWHM) under experimental conditions.

The negative temperature gradient from +20 to -125 °C, applied along the TC column was achieved by cooling the exit end of the column with liquid nitrogen. The temperature along the detector channel was measured by four thermoelements, the first thermoelement was glued near the first PIPS diode, the second near the 11th, the third near the 21st and the fourth thermoelement near the 32nd PIPS diode. A typical temperature measurement with a fitted gradient can be found in Figure 2.13.

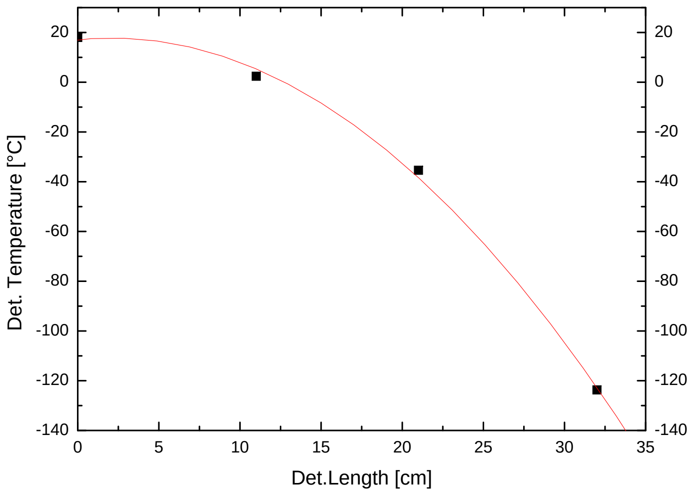

Figure 2.13: Measured COMPACT temperatures (black boxes) and fitted temperature gradient (red line).

The gradient is not linear, due to the limited thermal conductivity of INVAR^{TM}, hence it is steeper in the low temperature range. A dew point of about -70 °C was achieved under experimental conditions, minimizing water adsorption on the inner detector surface. This was done by drying the gas in a condensation cold-trap and by chemical means using a drying cartridge filled with Sicapent^{TM}. A thin ice layer was formed during the experiment on surfaces with temperatures below the dew point. The ice layer was negatively affecting the energy resolution in the cold part of the detector channel mainly for detector pairs 26 to 32, which are kept at temperatures of -70 °C to -125 °C. Because HsO_4 molecules were adsorbed at higher temperature, formation of ice did not degrade the detector resolution for Hs decays. Once a day the gas loop was switched from the used one to the newly dried and conditioned detector. The former detector was heated up to room temperature, pumped down on one side by a vacuum pump while flushed from the other side with helium gas to remove the ice or water layer from the detector channel and to prepare it for the next detector switching.

The signals from the PIPS diodes were processed with 64-channel spectrometric electronics, built at the Joint Institute for Nuclear Research, Dubna. The electronics existed twice to make the switching of the detectors once per day as fast and easy as possible. A schematic diagram of the COMPACT electronics is presented in Figure 2.14. 64 PIPS diodes were connected to four 16-channel preamplifiers through coaxial cables. The diodes were operated at E_{Bias} = -10 V, the average dark current through one single diode was ~ 10 nA if the detector was cooled. Signals from the preamplifiers were provided over coaxial cables to four 16-channel amplifiers with two amplification ranges ($\times 1$ and $\times 10$). Then they were multiplexed in 8 16-channel multiplexors. The analog signal and digital information about the detector number from the multiplexor were processed in a ADC module. The ADC module consists of 8 12-bit ADCs, a 1 μs clock and a communication module based on the ALTERA$^{\mathrm{TM}}$chip. The ADC device was read out by the data acquisition computer via a PCI interface card containing a FIFO buffer. The readout time was 5 μs, hence a signal counting rate with a frequency of up to 200 kHz could be processed. Data were transferred via a computer network and stored at a data analysis computer, placed in the control room. The data analysis software allowed on-line visualization of the data and an on-line correlation search. The COMPACT electronics was constructed to be reliable and easily transportable. The power supply for the electronics, all amplifiers, and ADCs were designed as 19” rack modules. Hence, it was possible to place the whole electronics together with the power supply and test modules in a 12 U 19” rack.

2.2.5 Gas system

The main tasks of the gas system is to fast and efficiently transport the created volatile species to COMPACT. These volatile species are flushed out of the RC, transported through the PTFE capillary via the heated quartz wool plug, where the separation from non-volatile compounds takes place, to the detection system. There, the volatile species can be adsorbed and their decay can be measured. The gas system was installed as a gas loop to reduce gas humidity. This was necessary, because the detector was

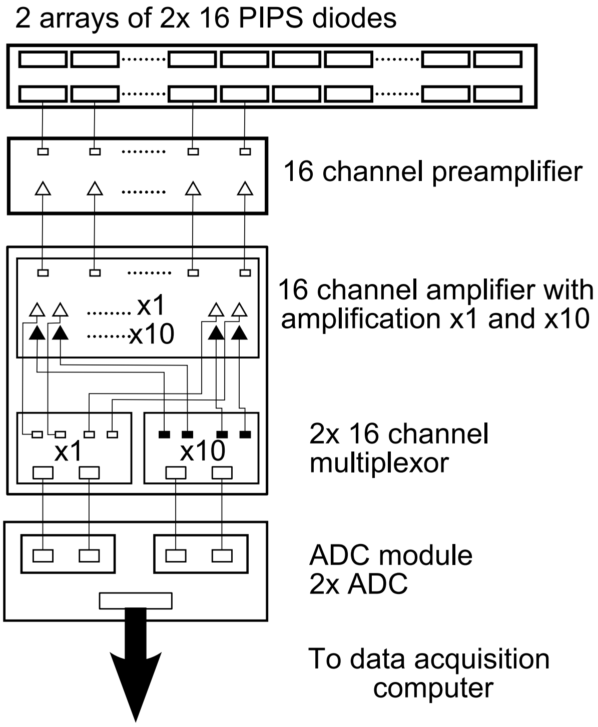

Figure 2.14: Schematic drawing of the data acquisition electronics. Connections for the readout of 16 out of 64 PIPS diodes are shown.

cooled down to very low temperatures. Hence, the water content of the transport gas had to be removed to avoid water condensation and ice formation on cold surfaces inside the detector channel. Especially for experiments with very volatile species, where very low temperatures are established, a very dry system with a very low dew point is strongly recommended. This was achieved by continuous recycling and drying of the gas. Another important condition was the pressure in the recoil chamber, which was limited by a ~ 20 μm thin Be vacuum window, separating the RC from the accelerator beam line, to a maximum pressure difference of 1.2 bar. Especially during an irradiation of radioactive targets any disruption of the vacuum window is extremely dangerous and has to be avoided to prevent the beam line from being contaminated by target material fragments. Reliable and fast acting safety precautions have to be employed to avoid a pressure increase, which is able to destroy the vacuum window. A schematic drawing of the gas system used in TUM Hs chemistry experiments is shown in Figure 2.15.

Gas was circulated in the loop with membrane pumps. Flow conditions, dew point, and pressure of the gas were controlled continuously by a computer. The control software was written in LabVIEW$^{\mathrm{TM}}$providing an automation of the gas control. Safety measures

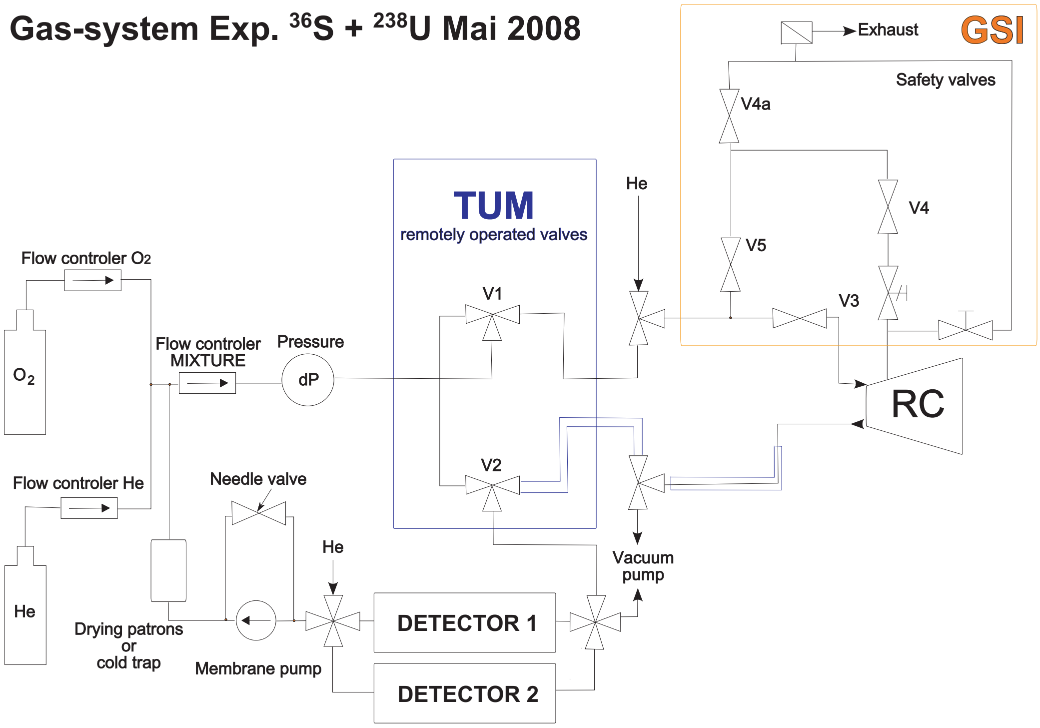

Figure 2.15: Schematic drawing of the improved gas system, as used in the ^{36}S + ^{238}U experiment.

were assured by two independent systems. The first safety system, shown in Figure 2.15 as a box (”GSI safety valves”), was a system of hardware operated valves, which immediately ventilated the recoil chamber to air in case of an overpressure or underpressure in the recoil chamber to prevent any damage of the target and vacuum window. The second safety system was operated by the LabVIEW^{TM}control server, which prohibited all flows in the gas system and switched the system to the by-pass mode in case of any unexpected behavior of the gas system. This was necessary to prevent any water contamination propagating in the gas system, which would have caused a longer drying period of the gas system.

The moisture of the gas was determined by a NYAD^{TM}device through measuring the dew point temperature. For drying of the gas, different techniques can be used, chemical and/or physical drying procedures. Chemical methods are e.g. the use of tubes filled with fresh activated silica-gel, alkali metals, or their hydrides or phosporus-pentoxid which all interact very strongly with water. Silica-gel is also able to trap water vapors, if it is cooled down. The most used physical method is the cooling trap, in which the gas is flushed through a column which is cooled down by liquid nitrogen to about -90 °C condensing water until the dew point has reached the trap temperature. In this experiment, a cold trap filled with molecular sieves and a trap filled with Sicapent$^{\mathrm{TM}}$was used. A dew point of -70 °C was achieved under experimental conditions, which proved to be sufficient to keep the part of the detector surface clean, where $\mathrm{HsO_4}$ adsorbed.

Another main task of the gas system is to establish a high gas flow through the system, which corresponds to a low transport time being very relevant for the total efficiency of the setup. The flow is created by membrane pumps establishing a flow of up to 1.8 l/min. At typical gas flow rates a transport time of about 2 s was achieved in this experiment. A picture of the gas system, the electronics, and both detector boxes can be found in Figure 2.16.

Figure 2.16: Photograph of the experimental setup: 2 COMPACT detectors with related electronics, and the gas control system.

Due to small leaks in the vacuum windows and of the RC and in the cooled detector panel, new gas had to be supplied from gas tanks from time to time. Unfortunately, another leak at the Swagelok$^{\mathrm{TM}}$connector linking the exit of the detector with the gas system was found. This leak was caused by thermal contraction of the PTFE capillary which was larger than the thermal contraction of the stainless steel Swagelok$^{\mathrm{TM}}$connector. A leak rate of 100 ml/min was measured, corresponding to 5% of the total flow through the system. However, this leak was not affecting the measurement, because it was located at the exit outside of the detector. The gas pressure in the system, gas flow rates, as well as moisture of the gas was controlled on-line by a LabVIEW^{TM}server. The inner logic of the server allowed autonomous operation of the gas system and automatic actuation of safety valves in case of unexpected behaviour. The design and commissioning of the gas control system was carried out in the framework of [8].

2.3 DGFRS experiments

2.3.1 The DGFRS

The Dubna Gas-Filled Recoil Separator (DGFRS) is installed at the Flernov Laboratory of Nuclear Reactions (FLNR) at the Joint Institute for Nuclear Research (JINR) in Dubna, Russia and was put in operation in 1989 [87]. The layout of the DGFRS is the traditional DQQ setup, with the dipole magnet close to the target, followed by a quadrupole doublet, the first focusing in horizontal, the second focusing in vertical direction. A schematic picture of the separator can be found in Figure 2.17.

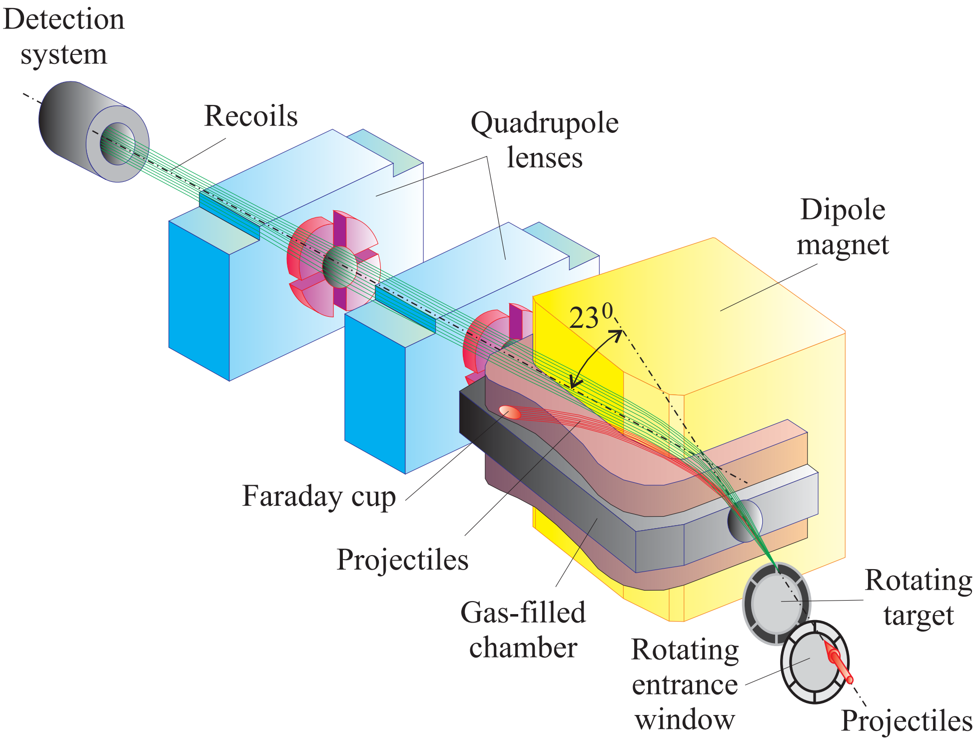

Figure 2.17: Schematic drawing of the DGFRS

The separator is filled with hydrogen gas at a pressure of about 1 Torr ($\widehat{=}$ 1.33 mbar). The maximum rigidity, which can be achieved with the dipole, is about 3.1 Tm. This value is the worldwide maximum for separators used for fusion-evaporation reactions. By using hydrogen instead of helium, the average charge state of the ions is reduced resulting in increasing magnetic rigidities. Hence strong dipole magnets are required. The main advantage of using hydrogen gas inside of a separator is the increased ratio of magnetic rigidities of fusion products, targetlike products, and beam particles and hence better separation inside of the dipole. The transmission efficiency of the separator for Z $= 112 - 118$ nuclei produced in reactions of ^{48}Ca with actinide targets is about $35 - 40\%$ [74].

A picture of the DGFRS can be found in Figure 2.18.

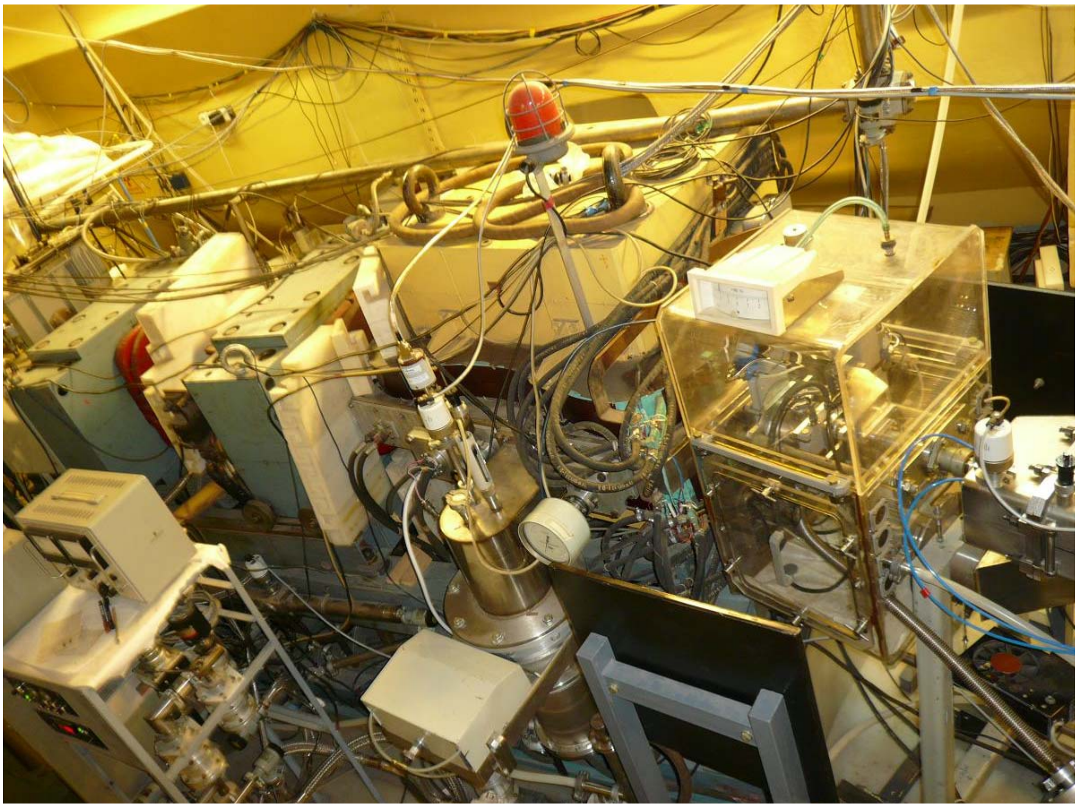

Figure 2.18: Picture of the DGFRS. The targetbox is situated on the right side, the dipole magnet in the center and the quadrupol doublet on the left.

2.3.2 Irradiation setup

A very important feature of the DGFRS is the possibility to irradiate highly radioactive targets. In the last years several radioactive actinide targets from less active ones like ^{238}U ($T_{1/2} = 4.468 \cdot 10^9$ a) to highly active targets like ^{249}Cf ($T_{1/2} = 350.6$ a), have been used for the production of SHE. A list of those used actinides can be found in table Table 2.3.

Table 2.3: Comparison of radioactive actinide targets used for complete nuclear fusion reactions with ^{48}Ca-beams, measured at the DGFRS.

Target	deposited as	half-life [a]	decay mode	thickness [mg/cm^2]
^{233}U	U_3O_8	$2.455 \cdot 10^5$	α	0.44
^{238}U	U_3O_8	$4.468 \cdot 10^9$	α	0.35
^{237}Np	NpO_2	$2.144 \cdot 10^6$	α	0.37
^{242}Pu	PuO_2	$3.750 \cdot 10^5$	α	0.40
^{244}Pu	PuO_2	$8.00 \cdot 10^7$	α	0.38
^{243}Am	AmO_2	7370	α	0.36
^{245}Cm	CmO_2	8500	α	0.34
^{248}Cm	CmO_2	$3.40 \cdot 10^5$	α, SF	0.35
^{249}Cf	CfO_2	350.6	α	0.23, 0.34

Dealing with the highly radioactive targets is a special challenge for SHE experiments. On the one hand the emitted radiation is a hazard for nuclear scientists and technicians working on the experiment. Hence, it is strongly recommended and necessary to install an effective shielding of the target during the mounting and dismounting of the target box and working with it during the experiment. The mounting of the target wheel inside of the target box is performed in a high level safety lab. The separator and in particular the detection system have to be protected from any contamination with the target material as it may happen when the target gets destroyed by the beam. Both aims can be achieved by constructing a target box with an internal second shielding. The target box used at the DGFRS at FLNR can be closed by valves on the beamline side as well as on the separator side. This makes sure, that no activity can leave the target box during mounting or dismounting. A picture of the target box and the surrounding

Plexiglas box can be found in Figure 2.19.

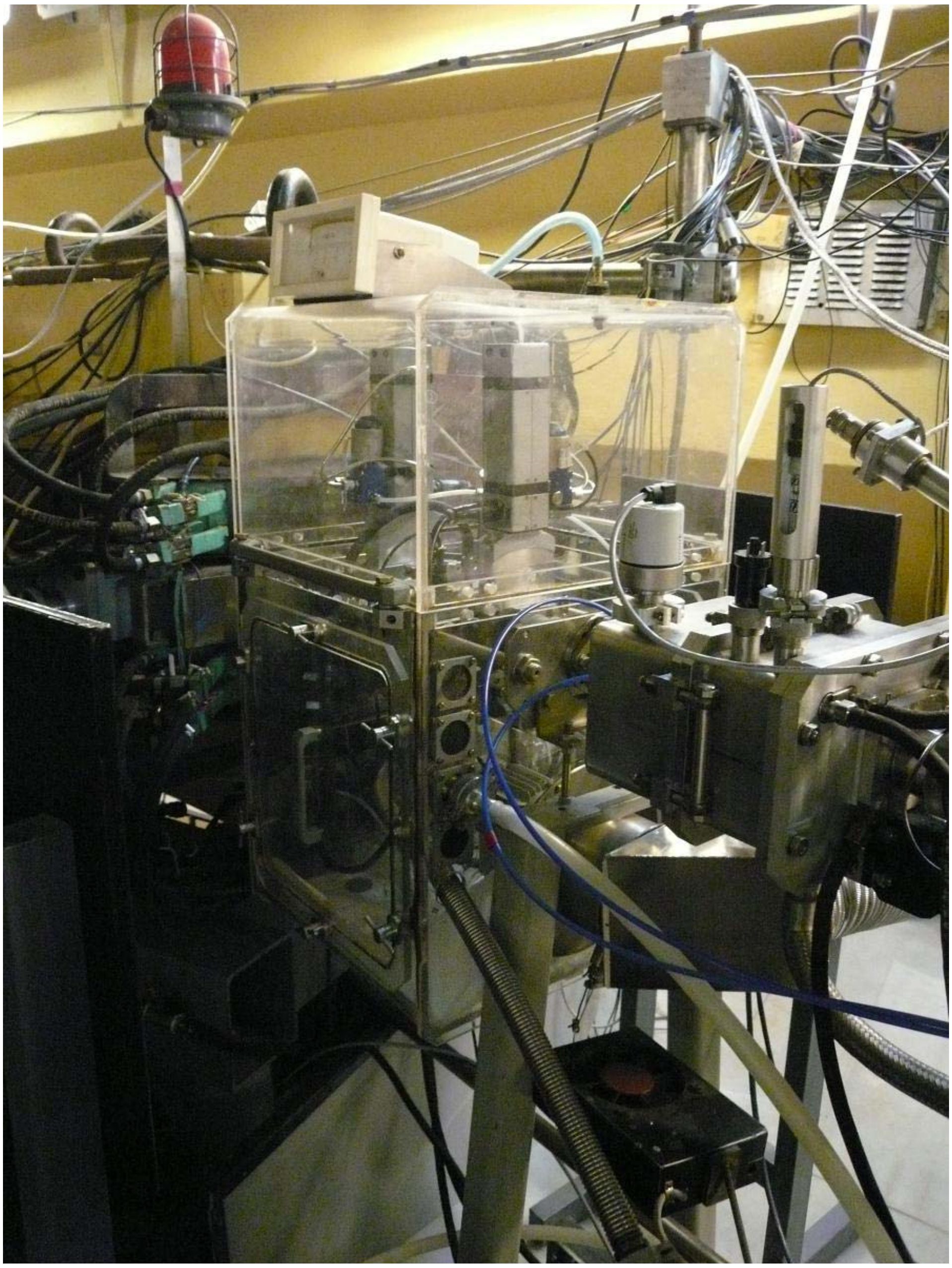

Figure 2.19: Picture of the target box with the surrounding Plexi-glas box.

Due to the target box and valve tightness, materials and thicknesses, almost no radiation can escape the array. To prevent the separator and dectection system from fragments of a destroyed target, the target wheel itself is arranged in a second inner box. This box has a cylindrical shape and two holes, one on the beam line side and one on the separator side. The ions of the beam pass the front hole, before impinging on the target wheel. Reaction products being created inside of the target, leave the target in beam direction and pass the rear hole. Afterwards they reach the separator and get deflected by the dipole magnet. If the target gets destroyed, i.e. by very high beam intensity, the target material gets scattered and only very little passes the small hole, while the bulk of it is retained by the walls of the inner box.

Another problem, which may happen dealing with radioactive targets is the emanation of radioactive gases as decay products of the target material. This was the case during the two experimental campaigns in 2008, when two ^{226}Ra-targets were irradiated by ^{48}Ca ions. The target material was deposited on a 1.5-μm Ti foil of the 36-cm^2 rotating target wheel. The thickness during the first campaign was 0.23 mg/cm^2 and 0.36 mg/cm^2 during the second campaign. The integrity of the target layer was tested regularly by measuring the ^{226}Ra α-particle counting rate. ^{226}Ra decays by α-decay with a half-life of 1600 years to ^{222}Rn. ^{222}Rn is a noble gas with a half-life of only 3.825 days. The decay products are also short lived. When the ^{226}Ra-target is irradiated during an experiment, it gets heated due to energy loss of the beam ions. Hence ^{222}Rn-nuclei diffuse rapidly to the surface and leave the target and may contaminate the separator, detection system, and technical equipment. Due to this reason, in most accelerator facilities in the world, handling ^{226}Ra is prohibited. Indeed, performing experiments with ^{226}Ra is very challenging due to the ^{222}Rn problem. Nevertheless, the scientists in Dubna created a very effective but simple solution. A vacuum pump was connected to the inner target box removing all evaporated ^{222}Rn. Between the inner target box and the pump, two cylinders filled with charcoal were mounted, absorbing ^{222}Rn due to the large surface. During the experiment the success of this method was tested by measuring the activity at the surface of the two charcoal filled tubes. In the first part of the experiment, only the first tube was active, while almost no radiation was emitted by the second tube. Later on a rise in activity could be measured for the second tube. The two tubes can be considered as a chromatography column which are slowing down the ^{222}Rn atoms due to van-der-Waals interaction with the large charcoal surface. Because of the relatively short half-life of ^{222}Rn of about four days, nearly all gas atoms have decayed inside of the tubes. As a second protection method, a Plexiglas box was mounted around the target box and kept under low pressure. In total, neither the detection system or the separator nor the experimental hall were contaminated during both experimental campaigns, which lasted several months.

The beam particles, ^{48}Ca ions in our case, were produced by the ECR source, extracted, injected to and accelerated by the U400 cyclotron of the FLNR, JINR. Typical beam intensities at the target were 0.7-1.1 pμA. Three different beam energies have been used, $E_{lab} = 228.5$ MeV, 233.5 MeV, and 240.5 MeV. The beam energy was measured by applying a time-of-flight system with a systematic uncertainty of 1 MeV. After passing through a rotating 1.5-μm Ti foil, serving as a vacuum window between the gas-filled separator and the vacuum of the beam line, the beam was impinging on the 36-cm^2 rotating target. Behind the target box, the magnets are installed in the aforementioned order. Behind the second quadrupole, a Mylar window of about 1 μm thickness is installed, to separate the hydrogen of the DGFRS from the detection system box, which is filled with pentane with a pressure of about 1.5 Torr. In the detector box, the detection system is installed.

2.3.3 Detection system

The detection system itself consists of two units, the time-of-flight (TOF) system and the focal-plane detector and is installed inside of the pentane filled detector chamber, following the DGFRS from beam direction. A schematic drawing can be found in Figure 2.20

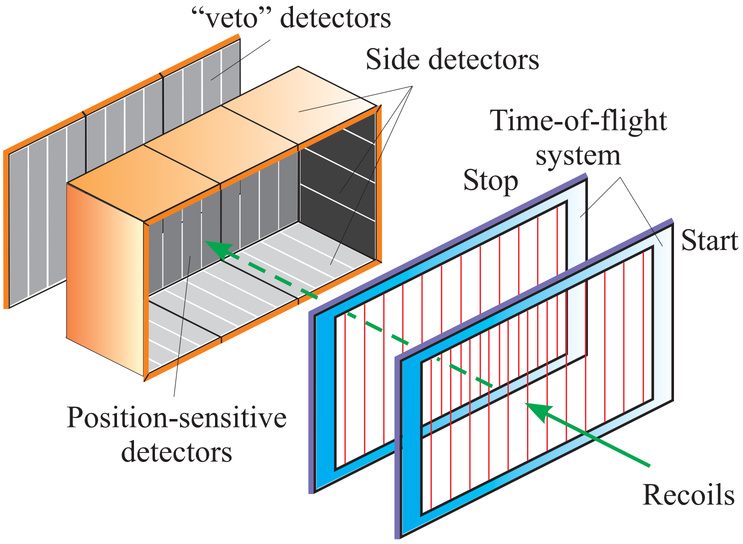

Figure 2.20: Schematic drawing of the DGFRS detection system consisting of the time-of-flight (TOF) system and the focal-plane detector, as used in the ^{48}Ca + ^{226}Ra experiment.

The TOF system consists of two arrays of multiwire proportional chambers, each array is composed of anode and cathode grids. The main function of the TOF-system is to distinguish in the focal-plane detector between implantation signals of recoiling nuclei and signals from radioactive decay inside of the focal-plane detector. While traveling through the pentane, the recoiling nuclei interact with the gas creating ion-electron pairs, which are divided and amplified by the electric field between the anode and the cathode and read out as a current signal in both of them. After passing the TOF, the recoiling nuclei are implanted in the focal-plane detector. A picture of the focal-plane detector can be found in Figure 2.21. The silicon based focal-plane detector is composed of the implantation detector, where the recoiling nuclei are implanted, the backward array or box detector to measure decays in backward direction and the veto or punch-through detector installed behind the implantation detector for measuring scattered hydrogen atoms passing the implantation detector.

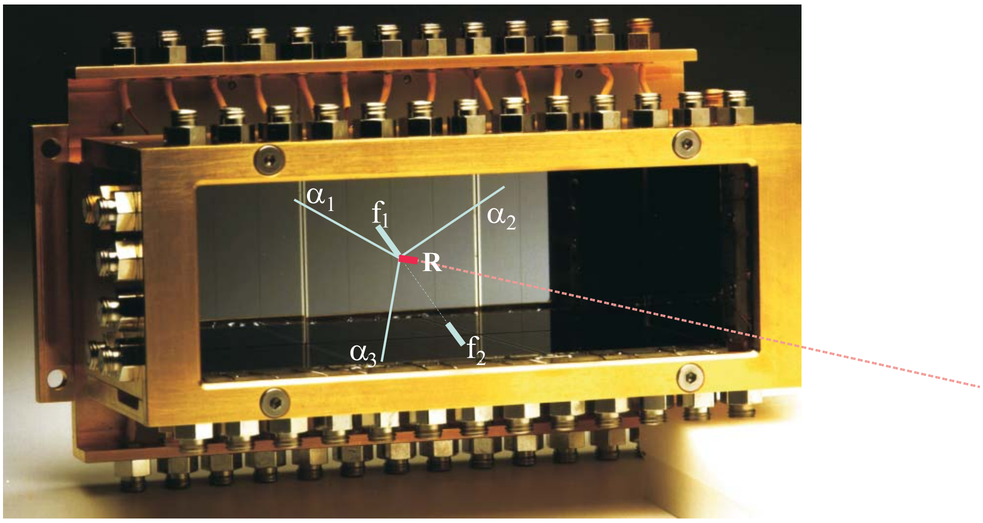

Figure 2.21: Picture of the focal-plane detector, as used in the ^{48}Ca + ^{226}Ra experiment. The red line indicates an impacting EVR, while its decay inside of the detector is outlined by the blue lines.

The implantation detector is a 4 cm x 12 cm silicon detector array with 12 vertical position-sensitive strips, which is surrounded by eight 4 cm x 4 cm silicon side detectors without position sensitivity, forming the box detector. The overall detection efficiency for alpha particles, emitted from decays of implanted nuclei is about 87 %.

The detection system is usually calibrated using well known reactions, creating well known products, for example, $^{48}\mathrm{Ca} + {}^{\mathrm{nat}}\mathrm{Yb} \rightarrow \mathrm{Th} + xn$ and $^{48}\mathrm{Ca} + {}^{206}\mathrm{Pb} \rightarrow {}^{252}\mathrm{No} + 2n$. The thorium isotopes were used for the calibration of the α range. These isotopes (especially ^{217}Th with $E_\alpha = 9.25$ MeV) are quite useful to perform alpha calibration for superheavy element synthesis experiments. Due to the very short half-lives, the predominant alpha decay occurs with a high energy similar to the alpha energies from the decay of superheavy elements.

The resulting energy resolution of the detection system for α particles is 50-110 keV (FWHM) for decays in the implantation detector, depending on the strip number, and 130-310 keV for α particles escaping the implantantion detector in backward direction and being measured in the box detector.

The decay of ^{252}No, which has a large fission branch, was used to calibrate the high energy branch of the detectors with SF fragments. The measured fragment energies were not corrected for the pulse-height defect of the detectors or for energy loss of escaping fission fragments in the detector chamber entrance window, dead layers of the detectors, and the pentane gas filling of the detector chamber. The mean sum energy loss of fission fragments of ^{252}No registered in the implantation detector and side detectors compared to the total kinetic energy (TKE) was about 20-25 MeV.

The position resolution also measured at FWHM of correlated EVRs with emitted α particles or fission fragments were 1.1-1.9 mm and 0.6-1.6 mm, respectively. For α particles, detected by both the implantation detector and side detector, the EVR-α position resolution depends on the energy deposited in the implantation detector and had a mean value of 2.0-3.5 mm and 3.4-5.8 mm for energies larger and lower than 3 MeV, respectively.

Chapter 3

Analysis of the experimental data

The current chapter presents the experimental data analysis performed on the data obtained in the experiments dealing with the nuclear reactions $^{36}\mathrm{S} + {}^{238}\mathrm{U}$ (Section 3.2) and $^{48}\mathrm{Ca} + {}^{226}\mathrm{Ra}$ (Section 3.1). The calculation of the overall efficiency of COMPACT, which describes the experimental sensitivity is displayed in Section 3.3. The expected decay pattern is a cascade of subsequent decays and hence time correlations between detected events can be used to identify Hs decay chains in the α- and SF background, which is introduced and presented in Section 3.4.

3.1 Analysis of experimental data from the DGFRS experiments

3.1.1 Experiments on the reaction $^{48}\mathrm{Ca} + {}^{226}\mathrm{Ra}$

The experiments on the complete nuclear fusion reaction $^{48}\mathrm{Ca}+$ $^{226}\mathrm{Ra}$ were prepared, conducted, operated, and analyzed by the DGFRS group of the FLNR, JINR, Dubna, Russia. Our group was invited to both experimental campaigns, in summer 2008 and winter 2008/2009 and, hence, we could work on the experiments in a collaboration of the FLNR and the Institut für Radiochemie of the Technical University of Munich. As mentioned the experiment itself as well as the analysis of the experimental data [97] have been performed by the DGFRS group and I was explicit allowed to use all the material in this thesis.

The Dubna gas-filled recoil separator [74] was used to transmit EVRs to the detectors and to separate them from ^{48}Ca beam ions, scattered particles, and transfer-reaction products. The transmission efficiency for Hs isotopes was estimated to be approximately 40% [97]. The EVRs, produced inside the target, recoiled out and passed through the DGFRS. After passing through a time-of-flight system (TOF) they were implanted in a 4-cm · 12-cm semiconductor detector array. Details can be found in Section 2.3.3. The experimental conditions are summarized in Table 3.1.

Table 3.1: ^{226}Ra target thicknesses, average reaction-specific lab-frame beam energies in the middle of the target layers used in the present work, corresponding average excitation energies, and total accumulated beam doses. Adapted from [97].

Target thickness [mg/cm^2]	E$_{lab}$ [MeV]	E* [MeV]	Beam dose [10^{18}]
0.23	228.5	34.2 - 38.1	2.9
0.36			3.3
0.23	233.5	38.0 - 42.5	3.0
0.36			1.1
0.36	240.5	44.0 - 48.1	2.3

During the first experimental campaign, two runs were performed with a 0.23 mg/cm^2 target while another three ones were performed with a 0.36 mg/cm^2 target during the second experimental campaign. Excitation energies of the compound nucleus at given projectile energies are calculated using the masses of [92], taking into account the thickness of the targets and the energy spread of the incident cyclotron beam. The beam energy losses in the entrance window of the separator, target backing, and target layers were calculated using [98]. Due to beam-associated background, for detection of daughter nuclides, the beam was switched off after a recoil signal was detected with an implantation energy of E$_{ER}$ = 9-15 MeV expected for complete-fusion evaporation residues, followed by an α-like signal defined by an energy of 9.0 MeV $\leq$ E $\leq$ 9.38 MeV in the same strip, within a 2.2-mm wide position window and a time interval of Δt$\leq$8 s. However, to reduce the number of beam interruptions and for collecting larger beam integrals during the first experiment (E$_{lab}$ = 233.5 MeV, 0.23 mg/cm^2 target), which happened about 75% of the experimental time, the experiment was performed without switching the beam off (see Table 3.1). The beam energy of E$_{lab}$ = 233.5 MeV corresponds to the expected maximum for the 4n-evaporation channel producing ^{270}Hs. ^{270}Hs decays via α-particle emission, followed by short-lived spontaneously fissioning ^{266}Sg ($T_{1/2}$=0.36 s [52]) and could be convincingly registered during beam-on intervals due to the low counting rate of SF-like events and a very short correlation time. Other parts of the experiment, investigating the $3n$ and $5n$ evaporation channel at $E_{lab} = 233.5$ MeV ($3n$ and $5n$), as well as both experiments at $E_{lab} = 228.5$ MeV ($3n$) were performed with 3-min beam-off intervals. In the experiment at $E_{lab} = 240.5$ MeV beam energy, examining the $4n$ and $5n$ evaporation channel, a beam-off time interval of 1 min was used. If an α-particle with E = 8.5-9.1 MeV was registered in any position of the same strip within the interval, the beam-off interval was automatically extended to 3 minutes.

Experiments were carried out at three beam energies (see Table 3.1). The highest projectile energy of $E_{lab} = 240.5$ MeV is close (3 MeV less) to the expected maximum of the $5n$ evaporation channel, obtained from calculations [41], as shown in Figure 4.6. A still higher production cross section for the $4n$ channel, compared to the $5n$ channel can be expected at this energy, according to the calculations (see Figure 4.6). The mean projectile energy of $E_{lab} = 233.5$ MeV corresponds to the maximum of the $4n$-evaporation channel cross section. At this energy one can expect minor production of ^{271}Hs in the $3n$-evaporation channel according to the calculations. At the lowest projectile energy of $E_{lab} = 228.5$ MeV corresponding to an excitation energy of $E^* = 36$ MeV, about the same yields of ^{271}Hs and ^{270}Hs can be expected. At this energy the yield of ^{271}Hs should be the same as at an energy of $E_{lab} = 233.5$ MeV corresponding to an excitation energy of $E^* = 40$ MeV, whereas the yield of ^{270}Hs should be three times lower at the lower energy (see Figure 4.6).

3.2 Analysis of experimental data from the TUM Hs chemistry experiment

3.2.1 Experiment on the reaction ^{36}S + ^{238}U

Hs nuclei were produced in the 3–5n channel of the reaction ^{238}U(^{36}S, xn)$^{274-x}$Hs. In an experimental campaign in 2008, one beam energy was used in combination with two different sets of ^{238}U targets. Due to differences in the target thickness, two different beam energies in the target were obtained in the middle of the target $E_{lab} = 179.5$ MeV and $E_{lab} = 193.5$ MeV, corresponding to excitation energies, $E^* = (39 \pm 4)$ MeV and

(51 ± 3) MeV, respectively. HIVAP predicted the maximum cross sections for the $4n$ and $5n$ evaporation channel, at these excitation energies. A summary of experimental conditions for both beam energies is given in Table 3.2. Due to the effective chemical separation, only α-lines originating from volatile species $^{172-174}$Os, ^{211}At, and ^{219,220}Rn and their daughters were identified.

Background α-decay events in the area of interest at α-particle energies of 8.0–10.0 MeV were attributed mainly to ^{212}Po originating from the in-flight decay of ^{220}Rn. A typical sum spectrum of all α-particles detected during the first part of the ^{36}S + ^{238}U experimental campaign of all 32 detector pairs is presented in Figure 3.1.

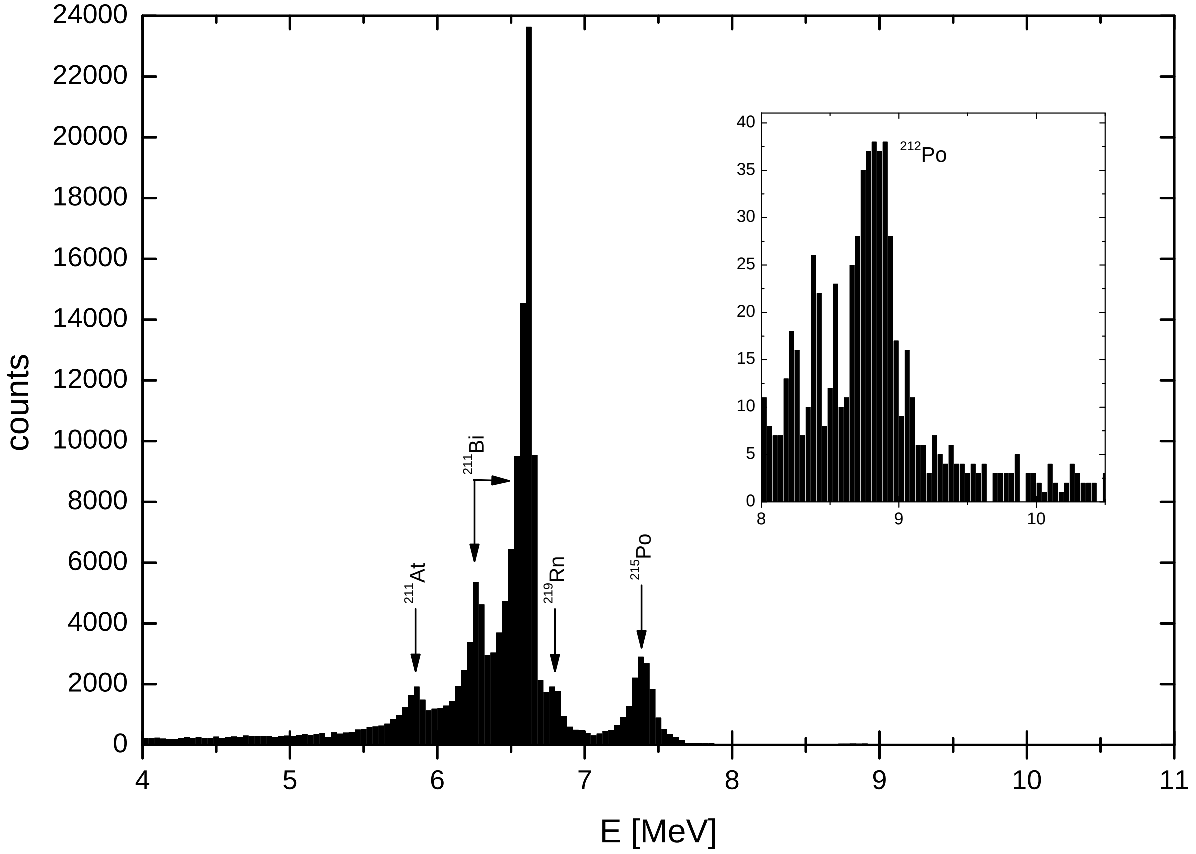

Figure 3.1: Alpha sum spectrum of all 32 detector pairs accumulated during the first part of the ^{36}S + ^{238}U experimental campaign (93 hours). ^{211}Bi originates mostly from off-line α-line calibrations. Only α-lines originating from ^{211}At and ^{219,220}Rn and their daughters were identified in the spectrum. The area of interest is shown in the enlarged cutout. Background α-decay events in the area of interest were attributed mainly to ^{212}Po originating from the in-flight decay of ^{220}Rn.

Taking the decay properties of ^{269}Hs [51, 52, 63, 65, 79, 83, 99], and heavier ^{270}Hs [51, 52], and ^{271}Hs [51, 52] as a base, a decay chain was defined as an α-decay occurring in the energy range from 8.0 – 9.5 MeV followed within 300 s in the same or a neighboring detector pair either by an α-decay in the same energy window or by a SF. This search procedure was repeated within the chain with identical conditions until no further α-decay or SF was found. Due to the α- and SF background, pseudo-correlated sequences can be formed with non-zero probability. Based on measured counting rates the number of expected random correlated chains was calculated. The number of expected α-SF and α-α-SF pseudo-correlated chains caused by background are presented in Table 3.2 along with the number of detected correlations.

Table 3.2: Summary of experimental conditions in the ^{36}S + ^{238}U experiments. E_{lab} denotes the beam energy in laboratory frame, E^* is the excitation energy, I_{Beam} is the accumulated beam integral, T_{irr} is the irradiation time in hours, N_α and N_{SF} are the numbers of measured α- ($8.0 < E < 9.5$ MeV) and SF ($15 < E < 400$ MeV) decays. n_b(α-SF) and n_b(α-α-SF) stand for the number of expected random α-SF and α-α-SF correlations caused by α- and SF-background. Columns N_2, N_3, and N_4 list the number of observed two-, three-, and four-member correlations (α-SF, α-α-SF, and α-α-α-α). The search for correlations was performed in subsequent 300 s time windows, according to the decay properties reported in [8].

E_{lab} [MeV]	E^* [MeV]	I_{Beam} [particles]	T_{irr} [h]	N_α	N_{SF}	n_b(α-SF) (300 s)	n_b(α-α-SF) (2×300 s)	N_2	N_3	N_4
179.5	39	$5.74 \cdot 10^{17}$	93	351	6	$1.6 \cdot 10^{-2}$	$4.6 \cdot 10^{-3}$	0	0	0
193.5	51	$1.03 \cdot 10^{18}$	149	732	13	$4.6 \cdot 10^{-2}$	$1.7 \cdot 10^{-3}$	1	0	0

From the comparison it is clear, that the one single detected α-SF correlation cannot be of random origin, due to a very low random probability. The analysis of the search method and evaluation of expected random correlations is presented in Section 3.4. The number of expected random events (n_b) in Table 3.2 can be considered as an absolute upper limit, because very wide α-energy and time windows were taken, due to the decay properties of the different expected hassium isotopes and their daughter nuclides (see Table 4.4).

3.3 Overall efficiency

The overall efficiency denotes the probability, to detect the decay of an evaporation residue inside the detection unit, produced inside of the target. This probability consists of the chemical reaction- and gas jet yield, the in flight decay probability, and the detection efficiency.

3.3.1 Transport efficiency

The transport efficiency defines the probability, that a evaporation residue produced inside and recoiling out of the target is being transported to the detection system. This probability consists of:

Chemical reaction- and gas jet yield - This describes the probability, that the produced Hs nuclei form a volatile tetroxide and are being transported to the detector by the gas jet.

In flight decay probability - Probability, that the species does not decay during the transport to the detector.

The chemical reaction and gas jet efficiency was estimated in previous test experiments in the framework of [8]. α-decaying, short lived Os isotopes were produced under the same experimental conditions as in the Hs chemistry experiments. The Os yield was maximized by changing the temperature in the recoil chamber, the temperature of the quartz filter, the He to O_2 mixing ratio and the gas flow rate. These determined optimum experimental conditions were used in the Hs chemistry experiments to achieve maximum yield. From the calculated production cross section of the nuclear reaction and from the Os yield, the chemical reaction and gas jet efficiency was estimated to be about 80%.

The survival probability, which is clearly dependent on the half-life of the investigated Hs isotopes, can easily be calculated from the known transport time in the gas flow. The transport time was measured in the aforementioned test experiments with short-lived Os isotopes. In the experiments on the reaction $^{36}S + ^{238}U$, searching for Hs isotopes with expected half-lives of at least around 10 seconds [8], a transport time of two to three seconds was estimated, resulting in survival probabilities of at least 81% and 87%, respectively.

The transport efficiency can be calculated by multiplying the chemical reaction and gas jet efficiency by the survival probability. In the case of this experiment, transport efficiencies of 64% to 70% were reached for 10 s Hs nuclei.

3.3.2 Detection efficiency of COMPACT

COMPACT, consists of two detector arrays of 32 PIN diodes each, facing each other resulting in a close to 4π geometry. This arrangement yields a high efficiency for the detection of α-decays and SF of species deposited on the active surface of the PIN diodes. Nevertheless, also inactive surfaces in the detector panel are available for adsorption of species, like the metal sides of the detector channel or the vacuum feedthroughs. Hence, a precise calculation of the detection efficiency is necessary to estimate the probability of an α-particle escaping a decay chain. The following assumptions were made for the calculation of the detection efficiency:

1. The deposition probability is the same on all types of surfaces.
2. An α-particle emitted from a decaying nucleus can be emitted by any angle with the same probability.
3. The two fragments emitted by a spontaneously fissioning nucleus are flying in opposite directions under 180°.
4. If an α-particle emitted from a decaying nucleus hits the active surface of a PIN diode, it is detected.
5. To exclude signals from α-particles that enter the detector under very shallow angles, only signals from neighboring detectors are accepted for the detection of genetically linked decay chains.

Deposition efficiency

Detailed dimensions of the detector channel and of a single PIN diode are shown in Figure 3.2. The deposition of a species is only possible on the surfaces inside the detector channel. These can be divided as follows:

Active surface - A species is deposited on the active surface of a PIN diode.

Nonactive surface - A species is deposited on the nonactive detector surface or on the side of the channel, but an emitted particle can reach it the active detector surface. Hence, there are two kinds of nonactive surface in the detector channel:

- Nonactive surface of a PIN diode.
- Side of the channel.

Dead surface - A species deposited on the dead surface cannot be detected. This corresponds to the contact place of vacuum feedthroughs. These form cavities which can only be reached by diffusion of the species. An emitted particle cannot reach the active detector surface. Hence, the species is considered to be lost, if it reaches the opening of the vacuum feedthrough cavity facing the detector channel. Therefore, the dead surface area is equal to the areas of openings of vacuum feedthroughs.

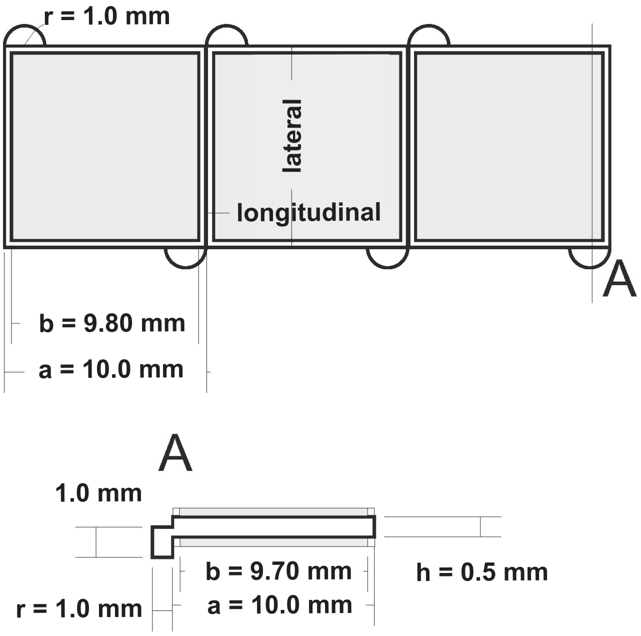

Figure 3.2: Top view and cross section view of the detector channel. Dimensions and directions, used in the calculations discussed below are shown.

The probability of deposition on a surface is proportional to the area of this surface. The probability that a species will be lost on the dead surface is given by the area of the opening of the cavity of a vacuum feedthrough. Relative areas of all surfaces inside the detector channel per one PIN diode are presented in Table 3.3.

Table 3.3: Relative areas of different surfaces inside the detector channel per one PIN diode and the probability of deposition on these surfaces.

	Active surface	Nonactive surface		Dead surface
		Detector	Side	
Area of surface in mm^2	95.55	4.46	4.35	0.65
Deposition probability	91.00 %	4.24 %	4.14 %	0.62 %

Geometrical detection efficiency

The geometrical detection efficiency defines the probability, that a particle emitted by a radioactive decay of a mother nucleus will hit the active detector surface. Due to the geometry of the detector, it depends on the type of surface on which the nucleus is deposited.

Active surface:

If an α-particle is emited by a species towards the active surface, on which it is deposited, this particle is detected. For particles emitted in the opposite hemisphere, the probability is calculated as a normalized integral over all possible positions and emittance angles. Integration in the 3 dimensional space is decomposed into two orthogonal directions - longitudinal and lateral, as shown in Figure 3.2.

Longitudinal direction - In longitudinal direction, particles can be detected in the detector directly opposite of the detector on which the species was deposited as well as in the neighboring detectors.

$$
\begin{aligned}
P_{Long} &= \frac{1}{\pi b}\int_{-\frac{b}{2}}^{\frac{b}{2}}\int_{0}^{\pi}\mathrm{d}\alpha\mathrm{d}x\\
P_{Long} &= \frac{1}{\pi b}\int_{-\frac{b}{2}}^{\frac{b}{2}}\left[\int_{\tan^{-1}\left(\frac{a+\frac{b}{2}-x}{h}\right)}^{\tan^{-1}\left(\frac{a-\frac{b}{2}-x}{h}\right)}\mathrm{d}\alpha + \right.\\
&\quad \left. + \int_{\tan^{-1}\left(\frac{\frac{b}{2}-x}{h}\right)}^{\tan^{-1}\left(\frac{-\frac{b}{2}+x}{h}\right)}\mathrm{d}\alpha + \int_{\tan^{-1}\left(\frac{-a+\frac{b}{2}+x}{h}\right)}^{\tan^{-1}\left(\frac{-a-\frac{b}{2}-x}{h}\right)}\mathrm{d}\alpha\right]\mathrm{d}x\\
P_{Long} &= \frac{1}{\pi b}\int_{-\frac{b}{2}}^{\frac{b}{2}}\left[\tan^{-1}\left(\frac{a-\frac{b}{2}-x}{h}\right) - \tan^{-1}\left(\frac{a+\frac{b}{2}-x}{h}\right) + \tan^{-1}\left(\frac{-\frac{b}{2}+x}{h}\right) - \right.\\
&\quad \left. - \tan^{-1}\left(\frac{\frac{b}{2}-x}{h}\right) + \tan^{-1}\left(\frac{-a-\frac{b}{2}-x}{h}\right) - \tan^{-1}\left(\frac{-a+\frac{b}{2}+x}{h}\right)\right]\mathrm{d}x\\
P_{Long} &= 96.45\ \%
\end{aligned}
\tag{3.1}
$$

Lateral direction - In lateral direction, only α-particles reaching the opposite detector are detected.

$$
\begin{aligned}
P_{Lat} &= \frac{1}{\pi b}\int_{-\frac{b}{2}}^{\frac{b}{2}}\left[\tan^{-1}\left(\frac{\frac{b}{2}-x}{h}\right) - \tan^{-1}\left(\frac{-\frac{b}{2}-x}{h}\right)\right]\mathrm{d}x\\
P_{Lat} &= 86.99\ \%
\end{aligned}
\tag{3.2}
$$

The probability to detect an α-particle emitted by the decay of a nucleus under a random angle from the active surface of the PIPS diode is:

$$
P_{AD}(\alpha) = 0.5 + 0.5 * P_{Long} * P_{Lat} = 0.5 + 0.5 * 0.9645 * 0.8699 = 91.95\% \tag{3.3}
$$

Since one SF fragment always hits the surface, where the species is deposited, and the other one flies in opposite direction, the geometrical detection probability for the first SF fragment is $P_{AD}(1.SFf) = 100\ \%$ and $P_{AD}(2.SFf) = P_{Long} * P_{Lat} = 83.9\ \%$ for the second one. Hence, the probability to detect both fragments, $P_{AD}(SF)$ is also 83.9 %.

Nonactive surface of a PIPS diode:

If an α-particle is emited by a species towards the nonactive surface, on which it is deposited, this particle is not detected. For α-particles emitted from this surface, the probability of detection is calculated similar to the case of the active surface. The nonactive surface of a PIPS diode is divided into two parts - longitudinal and lateral strips. Longitudinal strips have the area of $S^{Long} = 2 * b * \frac{a-b}{2} = 2.96\ mm^2$, lateral strips $S^{Lat} = 2 * a * \frac{a-b}{2} = 1.50\ mm^2$; the surface is divided in the ratio 66:34.

Longitudinal strip - Longitudinal direction The calculation is the same as for the active surface - longitudinal direction.

$$P_{Long}^{Long} = 96.45\ \% \tag{3.4}$$

Longitudinal strip - Lateral direction Since α-particles that are emitted under very shallow angles are neglected, only the two opposite detectors are taken into account in the calculations.

$$\begin{aligned} P_{Lat}^{Long} &= \frac{2}{\pi(a-b)} \int_{0}^{\frac{a-b}{2}} \left[\tan^{-1}\left(\frac{\frac{a-b}{2} - x}{h} \right) - \tan^{-1}\left(\frac{\frac{a+b}{2} - x}{h} \right) \right] \mathrm{d}x \\ P_{Lat}^{Long} &= 43.67\ \% \end{aligned} \tag{3.5}$$

Lateral strip - Longitudinal direction

$$\begin{aligned} P_{Long}^{Lat} &= \frac{2}{\pi(a-b)} \int_{-\frac{a-b}{2}}^{\frac{a-b}{2}} \left[\tan^{-1}\left(\frac{\frac{a+b}{2} - x}{h} \right) - \tan^{-1}\left(\frac{\frac{a-b}{2} - x}{h} \right) \right] \mathrm{d}x \\ P_{Long}^{Lat} &= 78.68\ \% \end{aligned} \tag{3.6}$$

Lateral strip - Lateral direction The calculation is the same as for the active surface - lateral direction.

$$P_{Lat}^{Lat} = 86.99\ \% \tag{3.7}$$

Hence, the final geometrical probabilities for species deposited on the nonactive surface of a PIPS diode are:

$$\begin{aligned}
P_{NAD}(\alpha) &= 0.5 * (0.64 * P_{Long}^{Long} * P_{Lat}^{Long} + 0.34 * P_{Lat}^{Long} * P_{Lat}^{Lat}) = 19.68\ \% \\
P_{NAD}(1.SFf) &= 0\ \% \\
P_{NAD}(2.SFf) &= (0.64 * P_{Long}^{Long} * P_{Lat}^{Long} + 0.34 * P_{Lat}^{Long} * P_{Lat}^{Lat}) = 50.39\ \%
\end{aligned} \tag{3.8}$$

Nonactive surface - side of channel:

Longitudinal direction - The calculation is similar as for the active surface, only the integration limits are changed to $-\frac{a}{2}, \frac{a}{2}$.

$$P_{Long} = 97.8\ \% \tag{3.9}$$

Lateral direction - An emitted α-particle from the decay of a nucleus can be detected in either one of the two bordering PIPS diodes.

$$\begin{aligned}
P_{Lat} &= \frac{2}{\pi h} \int_{-\frac{h}{2}}^{\frac{h}{2}} \left[\tan^{-1}\left(\frac{b + \frac{a-b}{2}}{\frac{h}{2} - x} \right) - \tan^{-1}\left(\frac{\frac{a-b}{2}}{\frac{h}{2} - x} \right) \right] \mathrm{d}x \\
P_{Lat} &= 56.01\ \%
\end{aligned} \tag{3.10}$$

Therefore, the final geometrical detection probabilities for the species deposited on the side of the channel are:

$$\begin{aligned}
P_{NAS}(\alpha) &= 0.5 * P_{Long} * P_{Lat} = 27.38\ \% \\
P_{NAS}(1.SFf) &= 0\ \% \\
P_{NAS}(2.SFf) &= 54.77\ \%
\end{aligned} \tag{3.11}$$

Dead surface:

If an α-particle is emitted by a decaying nucleus adsorbed on a dead surface, the probability to detect that α-particle (hit of an active surface of a PIPS diode) is assumed to be equal to zero.

Summary of geometrical detection probability:

The calculated geometrical probabilities for α-particles and SF fragments from a decaying mother nucleus being adsorbed on different surfaces before are summarized in the Table 3.4.

Table 3.4: Geometrical probabilities of different surfaces

	Active surface	Nonactive surface		Dead surface
		Detector	Side	
$P(\alpha)$	91.95 %	19.68 %	27.38 %	0 %
$P(1 \times SFf)$	100 %	50.39 %	54.77 %	0 %
$P(2 \times SFf)$	83.9 %	0 %	0 %	0 %

Detection efficiency

The detection efficiency is calculated from deposition probabilities (Table 3.3) and geometrical probabilities (Table 3.4). The probability to detect an α-particle, emitted from a species deposited somewhere in the detector channel, is about 84%. The probability to detect both fragments of a spontaneous fission decay is about 76%, to detect at least one fragment is about 94%. The detection probabilities for an α-α-SF decay chain are presented in Table 3.5. The abbreviation SFf stands for one fission fragment. The detection probabilities for an α-SF decay chain are presented in Table 3.6.

From the values in Tables 3.5 and 3.6 can be concluded, that the probability to identify an α-α-SF decay chain as a complete one (α-α-2 × SFf or α-α-1 × SFf is about 77% and to detect it as an at least two member correlation is about 92%. An α-SF chain will be identified in about 85% of all cases as complete.

Table 3.5: Detection probabilities for an α-α-SF decay chain.

	Active surface	Nonactive surface		Dead surface	Whole detector
		Detector	Side		
$\alpha-\alpha-2\times SFf$	70.94 %	0 %	0 %	0 %	64.56 %
$\alpha-\alpha-1\times SFf$	13.61 %	1.95 %	4.11 %	0 %	12.64 %
$\alpha-\alpha$	0 %	1.92 %	3.39 %	0 %	0.22 %
$\alpha-2\times SFf$	12.42 %	0 %	0 %	0 %	11.30 %
$\alpha-1\times SFf$	2.38 %	15.93 %	21.78 %	0 %	3.74 %
α	0 %	15.68 %	17.99 %	0 %	1.41 %
$2\times SFf$	0.54 %	0 %	0 %	0 %	0.49 %
$1\times SFf$	0.10 %	32.51 %	28.88 %	0 %	2.67 %
nothing	0 %	32.00 %	23.85 %	100 %	2.96 %

Table 3.6: Detection probabilities for an α-SF decay chain.

	Active surface	Nonactive surface		Dead surface	Whole detector
		Detector	Side		
$\alpha-2\times SFf$	77.15 %	0 %	0 %	0 %	70.20 %
$\alpha-1\times SFf$	14.80 %	9.92 %	15.00 %	0 %	14.51 %
α	0 %	9.76 %	12.38 %	0 %	0.93 %
$2\times SFf$	6.75 %	0 %	0 %	0 %	6.15 %
$1\times SFf$	1.30 %	40.47 %	39.77 %	0 %	4.54 %
nothing	0 %	39.95 %	32.85 %	100 %	3.67 %

Overall efficiency

The overall efficiency is calculated from the transport efficiency and the detection efficiency in COMPACT based on the decay properties reported from [8]. The overall efficiency for detection of ^{269}Hs ($T_{1/2}\sim 10$ s) in the ^{36}S + ^{238}U experiments is 54%, for detection of ^{270}Hs ($T_{1/2}\sim 23$ s) 60%, and for detection of ^{271}Hs ($T_{1/2}\sim 4$ s) 44% in case of an α-decay of ^{267}Sg and 48% in case of an SF-decay of ^{267}Sg. These overall efficiencies are significantly higher than those of kinematic separators for this type of reaction, which typically are $\sim 20-30\%$ and allow to measure products from a nuclear reaction with a production cross section on the level of a few picobarns. Especially for asymmetric nuclear fusion reactions, like ^{36}S + ^{238}U or ^{26}Mg + ^{248}Cm, chemistry experiments have a much higher efficiency than experiments with kinematic separators due to momentum systematics.

3.4 Time correlation search

Time differences between detected events can be used for the correlation search of the characteristic decay chain patterns in α and SF background, because a cascade of subsequent decays is the expected decay pattern of Hs nuclei. The background is considered to be stochastic and hence it can be treated mathematically by the use of a Poisson distribution. However, the possibility, that a correlated decay sequence is formed by random background of uncorrelated events has to be carefully considered.

The number of expected pseudo-correlated background events can be calculated by correlation search methods and parameters. Two correlation search methods can be found in the literature:

Subsequent time windows - After a start signal (detection of a first potential member of a decay chain), a time window is opened, large enough to include any following decay of the daughter nucleus. If in this time window a correlated event is observed, a next window is opened, starting immediately after the most recently found event, to search for another correlated event. The procedure is subsequently repeated, until no further event is detected. This method is described in [100].

Single time window - After a start signal (detection of a first potential member of a decay chain), a time window of defined length is opened and only correlated events within this window are searched for. This procedure was used in [79].

The two methods are compared in terms of the number of expected random correlations and search efficiency for a real decay chain in [8]. In the following, only the subsequent time windows method is used for estimating the number of pseudo correlated chains for the two parts of the experimental campaign conducted in the year 2008. In the irradiation, one correlated α-SF chain was observed, attributed to the decay of a ^{270}Hs nucleus. Experimental parameters are summarized in Table 3.7 (first part of the experiment) and Table 3.8 (second part of the experiment).

Table 3.7: Set of parameters from data obtained from an irradiation with an excitation energy of $E^* = 39 \pm 4$ MeV

Parameter	Value	Description
T_{exp}	93 h	Total time of irradiation
N_α^{Total}	351	Number of detected α-particles
N_{SF}	6	Number of detected SF events
N_{CD}	6	Number of PIPS diodes for pos. corr.
N_D	64	Total number of PIPS diodes
t_c	300 s	Correlation time window

Table 3.8: Set of parameters from data obtained from an irradiation with an excitation energy of $E^* = 51 \pm 3$ MeV

Parameter	Value	Description
T_{exp}	148.62 h	Total time of irradiation
N_α^{Total}	771	Number of detected α-particles
N_{SF}	13	Number of detected SF events
N_{CD}	6	Number of PIPS diodes for pos. corr.
N_D	64	Total number of PIPS diodes
t_c	300 s	Correlation time window

The COMPACT detector consists of two arrays of 32 PIPS diodes. Events are searched not only based on time correlation, but also on position correlation. Only events detected in the same or neighboring two detector pairs are considered to be position correlated. Hence, the average number of α-particles, which are in position correlation to a detected SF decay is reduced to:

$$N_\alpha = \frac{N_{CD}}{N_D} \times N_\alpha^{Total} \tag{3.12}$$

Mean count rates of α-decays and SF-events, are defined as:

$$\lambda_\alpha = \frac{N_\alpha}{T_{exp}}, \text{ and} \qquad \lambda_{SF} = \frac{N_{SF}}{T_{exp}} \tag{3.13}$$

3.4.1 Correlation search in subsequent time windows

For calculation of the number of expected random correlations, when the correlation is searched in subsequent time windows, several methods can be employed.

Method proposed in [100]:

This method is described in detail in reference [100]. The number of expected random correlations n_b for K different event groups is:

$$n_b = T_{exp} \frac{\prod\limits_{i=1}^{K} \lambda_i}{\left(\sum\limits_{i=1}^{K} \lambda_i\right)^{K-1}} \prod_{j=1}^{K-1} \left(1 - e^{-\sum_{i=1}^{K} \lambda_i \Delta t_{j,j+1}}\right) \tag{3.14}$$

where λ_i is the mean counting rate for event group i and Δt is the time interval between successive events. In our experiment, for an α-SF correlation $K = 2$ (α and SF).

$$n_b = T_{exp} \frac{\lambda_{SF} \cdot \lambda_\alpha}{\lambda_{SF} + \lambda_\alpha} \left[1 - e^{-t_c(\lambda_{SF} + \lambda_\alpha)}\right] \tag{3.15}$$

For an α-α-SF correlation ($K = 3$), where the α-particles have free order, the following formula was proposed:

$$n_b = T_{exp} \frac{\lambda_{SF} \cdot \lambda_\alpha^2}{(\lambda_{SF} + \lambda_\alpha)^2} \left[1 - e^{-t_c(\lambda_{SF} + 2 \cdot \lambda_\alpha)}\right]^2 \tag{3.16}$$

Finally, for an α-α-α-α correlation ($K = 4$) follows:

$$n_b = T_{exp} \frac{\lambda_\alpha^4}{64 \cdot \lambda_\alpha^3} \left[1 - e^{-t_c(4 \cdot \lambda_\alpha)} \right]^3 \tag{3.17}$$

As can be seen from equation (3.16), an exponential distribution of the time delay between two random events is expected. The two groups of events, α-decays and SF are considered to be independent and therefore they form two independent Poisson distributions in stochastic background.

Results obtained by the subsequent time window method:

With the set of parameters presented in Table 3.7 and Table 3.8 the number of expected random correlated events for the two parts of the experimental campaign in 2008 was calculated. Results are presented in Table 3.9.

Table 3.9: Number of expected randomly correlated background events forming chains of the type as given in the first column. The correlation time between two members of one decay chain in the correlation search using subsequent time windows is Δt. The used parameters from the experiment are presented in Table 3.7 and Table 3.8, for an excitation energy of $E^* = 39 \pm 4$ MeV and $E^* = 51 \pm 3$ MeV, respectively.

decay chain	E* = 39 MeV	E* = 51 MeV	Δt [s]
α-α-α-α	7.1×10^{-4}	3.1×10^{-3}	300
α-α-SF	4.6×10^{-3}	1.7×10^{-3}	300
α-SF	1.6×10^{-2}	4.6×10^{-2}	300
α-SF (^{270}Hs)	1.1×10^{-4}	1.1×10^{-4}	2

As can be seen, the probability, that the measured α-SF decay chain is of random origin, can be excluded. Especially, when a more realistic correlation time of 2 s is used, which corresponds to about six half-lives of ^{266}Sg [52].

3.4.2 Search efficiency of the subsequent time windows method

As the number of expected random correlations can be calculated precisely, the most striking question is, which is the optimal length of the time windows, in which almost all real decay chains could be found, but which contains only a small number of purely randomly correlated events formed by background. In the experiment, the real data form decay sequences, so that the time delay between the decay of chain members follows an exponential decay distribution. In the case of known half-lives of the members of a decay chain the probability to observe the decay chain in subsequent time windows can be calculated as:

$$P_{subseq} = \prod_{i=1}^{K} \left(1 - e^{-\Delta t_{i,i+1} \frac{ln(2)}{(T_{1/2})_i}}\right) \tag{3.18}$$

where K is the number of chain members after the initial decay, $\Delta t_{i,i+1}$ is the time window for the search of member i and $(T_{1/2})_i$ is the half-life of member i. The first α-decay is used as the starting signal for the correlation search in the experiment, because no information on the time of formation of a Hs atom is available. Resulting efficiencies for the search of decay chains in our experiments using 300 s time windows (as used in the actual data analysis) are shown in Table 3.10. A crucial point of the correlation search is the choice of a suitable time window. The choice of a 300 s time window for correlation search in the recent experiment is based on the observation from former experiments [8] about the decay properties of ^{267}Sg and ^{261a}Rf, which have half-lives that are relatively long in comparison to other decay products of $^{269-271}$Hs, resulting in only 92% and 93% search efficiency for the ^{271}Hs and ^{269}Hs decay chains, respectively. Clearly, a different time window length would be optimal for searches of different types of decay chains, but a single time window length (300 s) was used in our experiment for simplicity. Also a different choice of window lengths for decay members with different half-lives, that further decreases the chance of false identification of correlated decay chains of random origin, was not applied.

3.4.3 Conclusion on correlation search method

As shown in [8], the subsequent time window method is a powerful and useful tool to find correlated decay pattern in the data. The time window length is a critical parameter and has to be chosen carefully, to make an optimal trade-off between search efficiency and number of expected random correlations. With the calculation of search efficiencies, an optimal time window for every experiment can be found easily. In TUM experiments on Hs chemistry the method of search in subsequent windows with a fixed time window

Table 3.10: Decay chain search efficiency for the subsequent time windows method. For calculation purposes, real half-lives for Hs decays were used [51, 52, 63, 65, 79, 83, 99].

Decay	$T_{1/2}$		Decay chain search efficiency
	1st	2nd	$(2 \times 300$ s$)$
^{269}Hs → ^{265}Sg → ^{261a}Rf	15 s	78 s	0.93
^{269}Hs → ^{265}Sg → ^{261b}Rf	15 s	2.5 s	1.00
^{271}Hs → ^{267}Sg → ^{263}Rf	84 s	8.3 s	0.92

length of 300 s was chosen. Correlation search efficiencies for decay chains detected in the Hs experiments are presented in Table 3.10, numbers of expected random correlations for every irradiation are given in Table 3.2.

Chapter 4

Results and discussion

In this section, all experiments and their results are presented. The experiments treated in this thesis are, on the one hand, the TUM Hs chemistry experiment dealing with the reaction ^{36}S+ ^{238}U and on the other hand the DGFRS experiment about the reaction ^{48}Ca+ ^{226}Ra performed by the FLNR in collaboration with the institute of radiochemistry of the TUM. The results on the TUM Hs chemistry experiment is presented in Section 4.1. The results on the DGFRS experiment is presented in Section 4.2. A detailed discussion of the excitation functions obtained from nuclear fusion reactions containing the experiments performed in the framework of this thesis and the experiments performed in the framework of [8] can be found in Section 4.3. Finally new decay properties of Hs isotopes obtained from these experiments are presented in Section 4.4.

4.1 TUM chemistry experiments

During the irradiation of the first target, the first excitation energy of E* = (39 ± 4) MeV ($E_{lab} = (179.5 \pm 4.5)$ MeV) was investigated. The duration of the irradiation was 5 days with a typical beam intensity of 300 pnA and an integral of $5.74 \cdot 10^{17}$ ^{36}S ions was collected. This corresponds to an one event cross section limit of about 1.4 pb.

During the irradiation of the second target, the second excitation energy of E* = (51 ± 3) MeV ($E_{lab} = (193.5 \pm 3.5)$ MeV) was measured. This irradiation took 7 days with a typical beam intensity of 350 pnA. An beam integral of $1.03 \cdot 10^{18}$ ^{36}S ions was achieved corresponding to an one event cross section limit of 0.78 pb.

4.1.1 Results on experiments on the reaction ^{36}S+ ^{238}U

Correlated decay chains were searched for, which were defined as an α-decay ($8.0 < E_\alpha < 10.0$ MeV) followed within 300 s in the same or a neighboring detector pair by an α-decay in the same energy range or by a SF-decay with at least one detected fragment above a threshold of 15 MeV. The energy and time windows were chosen according to the reported decay properties of ^{269,270,271}Hs in [7, 51, 52] and ^{268}Hs in [69] shown in Figure 4.1 (b). Because of the background, pseudo-correlated chains can be found

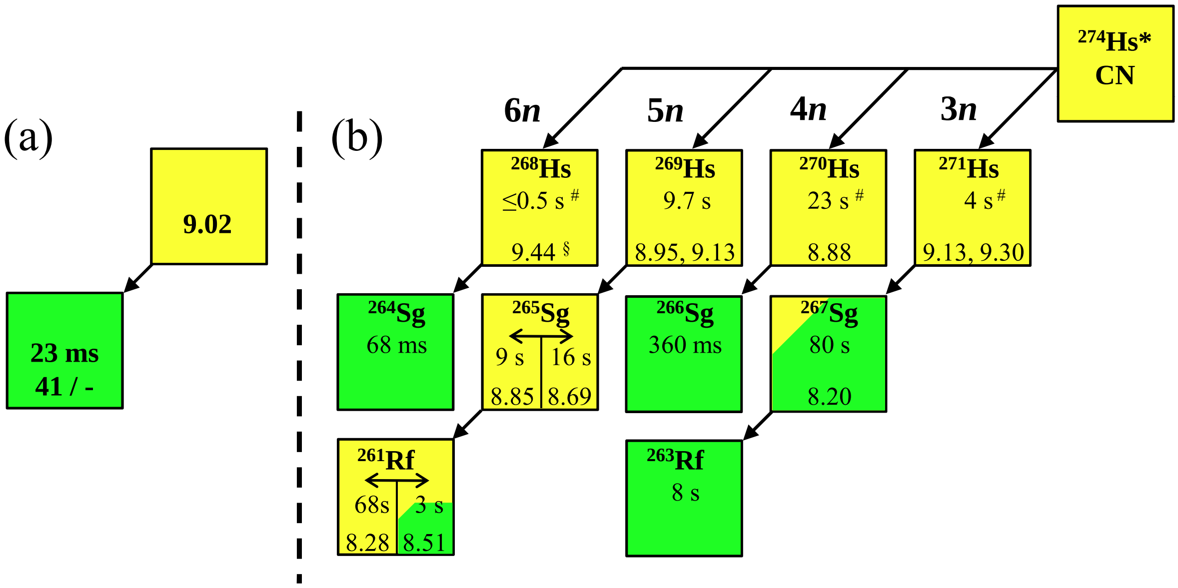

Figure 4.1: The observed decay chain (a) and known decay properties of the $^{268-271}$Hs isotopes and their daughters (b) [7, 51, 52, 69]. The half-lives of Hs isotopes marked with a sharp were calculated according to the formalism outlined in [56]. The α-decay-energy of ^{268}Hs marked with a paragraph sign is calculated from the Q_α-value of ^{268}Hs deduced from Q_α-systematics based on all known Hs-isotopes [69].

with non-zero probability. Based on our measured event rates in the energy regions of interest, we have calculated the probability to observe random decay chains of the types α-α-α-α, α-α-SF, and α-SF satisfying the energy and time criteria specified above. The results are summarized in Table 3.9. 351 and 771 α-particles have been registered in the above mentioned energy interval in the first and the second run, respectively. They originated mainly from α-decays of ^{212}Po, a daughter of ^{220}Rn. Also, 6 SF-fragment-like (SFf) events were registered in the first run and 13 SFf-like events in the second one. None of these were coincident with each other. The detection efficiency for at least one fragment is 94%, for both fragments, it is 76%.

Hence, the probability to register always only one fragment out of 6 or 13 SFf events was determined to be extremely low ($5 \cdot 10^{-5}$ and $5 \cdot 10^{-10}$, respectively). Thus, the SFf-like background originated mostly from background radiation induced by cosmic radiation or possibly electronic noise and not from real fission events. The data analysis revealed only one correlated decay chain at the higher excitation energy E*=51 MeV. A $9.02^{+0.05}_{-0.10}$ MeV α-particle was observed in the bottom detector #24 and was followed after 23 ms by one 41 MeV fission fragment measured in the top detector #24, as illustrated in Figure 4.1 (a). The temperature of that detector was around -60 °C, which situates in the temperature range, where hassium atoms have been deposited in former experiments [7, 51, 52]. Furthermore, no contaminations from non-volatile actinides and minor transactinides have been observed. Also the α-decay-energy of about 9 MeV points to a decay of Hassium. Measured events could also origin from a coincidental α-decay of ^{212}Po ($E_\alpha = 8.784$ MeV) and β^- decay resulting in a pile-up in the energy range of the measured α-event. However, due to the very low number of expected randomly correlated ^{270}Hs events (3.1×10^{-4} see Table 3.9), this chain is clearly attributed to a real decay of ^{270}Hs. The energy and energy resolution of detector pair #24 bottom where the relevant α-particle was observed was calibrated offline with ^{219}Rn-^{215}Po decay chains, measured in the same detector pair, occurring in a time window around this event.

At E* = (51 ± 3) MeV, ^{270}Hs, ^{269}Hs, and ^{268}Hs formed in the $4n$, $5n$, and $6n$ exit channels, respectively, are expected to be produced with significant cross sections. The observation of other exit channels at this excitation energy is highly unlikely. The SF following 23 ms after the α-emission may be attributed to the decay of ^{264}Sg, as it is well compatible with the reported half-life of ^{264}Sg of $T_{1/2} = 68^{+37}_{-18}$ ms [67, 68]. This assignment implies a preceding α-decay of ^{268}Hs, produced in the $6n$ evaporation channel. From Q-value interpolations of all known Hs isotopes, an α-decay-energy of about 9.44 MeV can be deduced [69]. Because of the significant deviation between this value and the measured α-particle-energy of $9.02^{+0.05}_{-0.10}$ MeV, ^{268}Hs can quite certainly be excluded as the correct assignment. From results of a chemical search experiment for this nuclide follows that its half-life is most likely ≤ 0.5 s [69], which is short compared to the transport time of the experimental set-up ($\tilde{2}$ s). This significantly reduces the overall efficiency for such short-lived species. Hence, assignment to ^{268}Hs would imply the cross section for the $6n$ evaporation channel to be much higher than that for the $5n$ evaporation channel, in contrast to expectations based on hot fusion excitation function systematics. The measured α-decay could thus be attributed to the decay of ^{269}Hs or

^{270}Hs. The well known decay of ^{269}Hs, produced in the $5n$ exit channel, consists of two successive α-decays from ^{269}Hs and ^{265}Sg followed by either an α-decay or SF of ^{261}Rf [51, 66]. Assuming, that we have only detected the first α-decay of ^{269}Hs and SF of ^{261b}Rf, while missing the α-decay of ^{265}Sg, the measured α-particle-energy is consistent with a reported α-particle-energy of ^{269}Hs, namely of 8.95 MeV [52]. However, the observed correlation time is much shorter than expected for such an incomplete ^{269}Hs decay chain based on the known half-lives of ^{265}Sg and ^{261b}Rf. In addition, due to the high detection probability of a single α-particle, the probability to miss an α-particle within a decay chain is low. The last possibility is the decay of ^{270}Hs, produced via the $4n$ exit channel. The measured α-decay energy again fits quite well with the reported value of 8.88 ± 0.05 MeV from chemistry experiments [52]. In addition, the observed correlation time is compatible with the reported half-life of ^{266}Sg of about 360 ms [52]. In conclusion, we tentatively associate the presently observed decay chain with the decay of a ^{270}Hs nucleus and its daughter ^{266}Sg. According to this assignment, the measured lifetime of ^{266}Sg is several orders of magnitude lower than the time window of 300 seconds, which was chosen for the event search for all possible decay chains from $^{268-271}$Hs. A more realistic calculation of the number of expected randomly correlated chains using a time window of five ^{266}Sg half-lives (2 s) can also be found in Table 3.9. Therefore, the probability that the observed α-SF decay chain is of random origin is negligible. At E* = 39 MeV, no event has been observed; the upper cross section limit for the $3n$, $4n$, and $5n$ evaporation channels at this energy is 2.9 pb. The cross section for the $4n$ channel at E* = 51 MeV based on the one observed event is $0.8^{+2.6}_{-0.7}$ pb and the cross section limit for the $3n$ and $5n$ channel is 1.5 pb. Errors and limits of measured cross sections correspond to the 68% confidence level [100].

4.1.2 Excitation function of the complete fusion reaction ^{36}S+^{238}U

The cross section limits for the ^{238}U(^{36}S, $5n$)^{269}Hs reaction at 51 MeV and 39 MeV excitation energy are comparable to or even lower than the cross section of the ^{248}Cm(^{26}Mg, $5n$)^{269}Hs reaction [52]. However, our results are in contrast to the predictions of [43]. The measured cross section and cross section limits are more than one order of magnitude lower than the predicted peak cross section of 24 pb derived in [43]. For the ^{248}Cm(^{26}Mg, $4n$)^{270}Hs reaction, Liu *et al.* [43] predicted a peak cross section of about 12 pb, half that of the ^{238}U(^{36}S, $4n$)^{270}Hs reaction. According to Liu *et al.* [43], the higher peak cross section for the latter reaction compared with the former one should be driven by Q-value effects. Our measurement excludes such a trend and furthermore contradicts quantitatively and qualitatively the predictions and conclusions made by Liu *et al.* [43], they better agree with HIVAP calculations within a factor of 2-3. A summary of experimental results in comparison with theoretical predictions is provided in Figure 4.2.

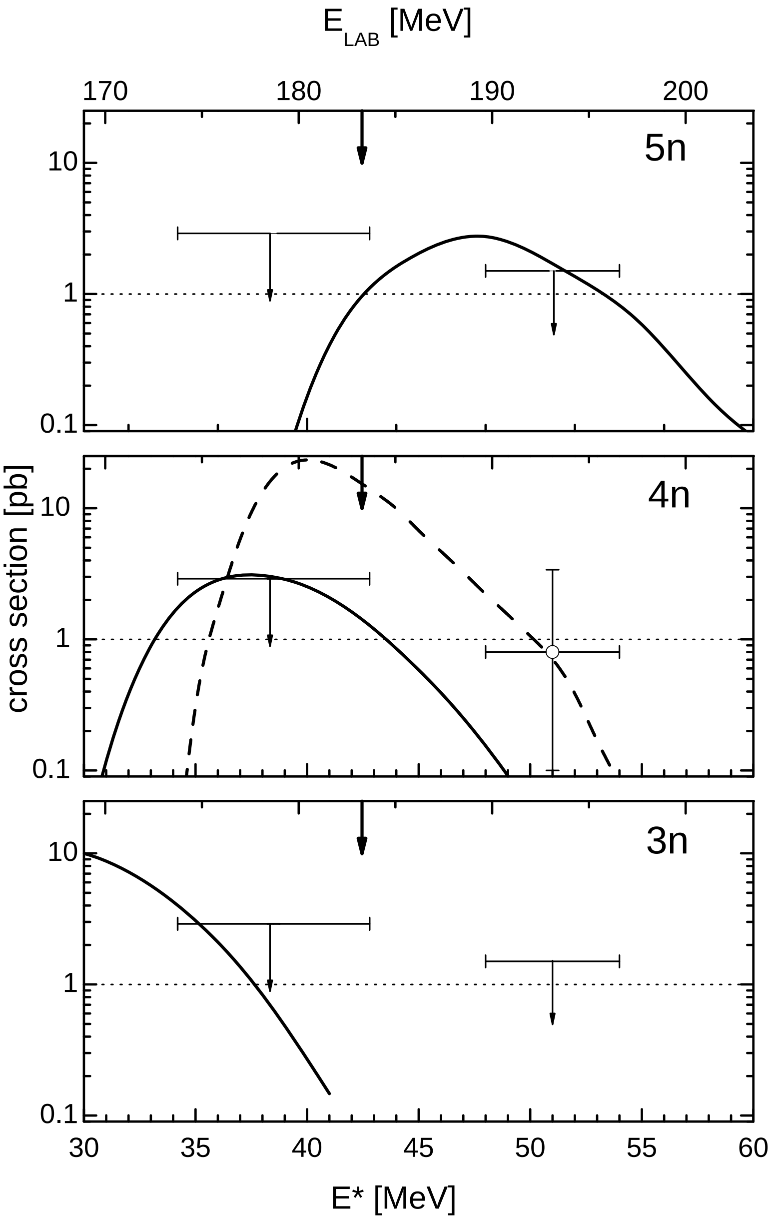

Figure 4.2: Production cross sections and limits measured for the reaction ^{238}U(^{36}S, xn)$^{274-x}$Hs in comparison with HIVAP calculations (solid line) and predictions from [43] (dashed line). Arrows indicate the location of the Bass fusion barrier.

4.2 FLNR separator experiments

4.2.1 Results

Results at the highest excitation energy [97]

At the excitation energy of 46 MeV a relatively high background of α-particles in an energy range of $E_\alpha \approx 8.2$ - 9.4 MeV originating from decays of ^{213}Po ($E_\alpha = 8.376$ MeV) and ^{212}Po ($E_\alpha = 8.785$ MeV) [101] (see Figure 4.3) was observed in this experiment.

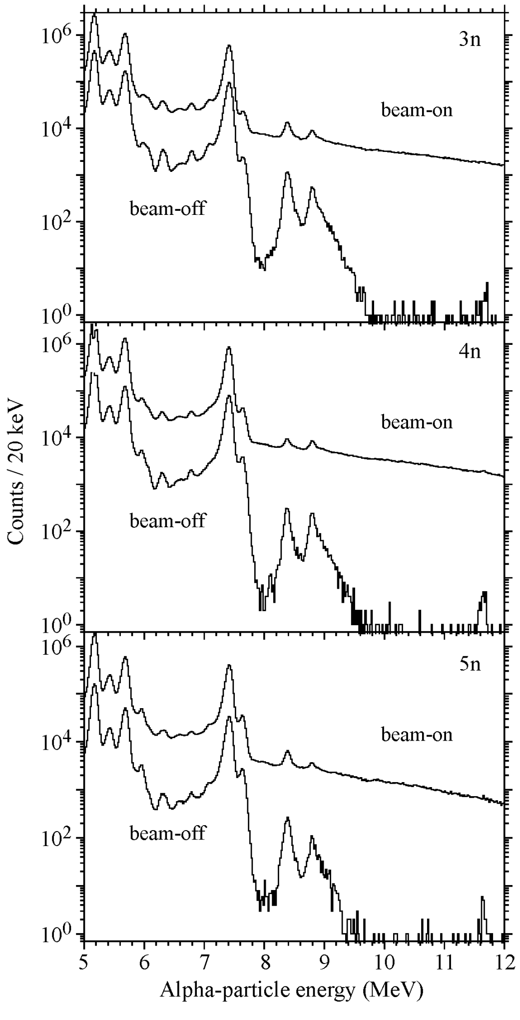

Figure 4.3: Total beam-on and beam-off α-particle energy spectra of events registered by the focal-plane detector in the ^{226}Ra+^{48}Ca reaction. In both spectra we observed peaks originating from the isotopes ^{222}Rn and ^{218,214}Po, the decay products of ^{226}Ra, and ^{212,213}Po, transfer-reaction products of ^{48}Ca with ^{210}Pb contained in the target material. Adapted from [97].

These isotopes were detected also in previous ^{48}Ca experiments dealing with ^{238}U-^{249}Cf target nuclei, but with lower rates (see e.g., [102]). ^{210}Pb is created as a decay product by successive α-decays of ^{226}Ra. Therefore, the isotopes ^{212,213}Bi can be produced in the +p+n- and +p+2n-transfer reactions on ^{210}Pb, as the target impurity. The expected α-particle-energy interval for the decay of ^{265}Sg [66], the daughter-product of the ^{226}Ra(^{48}Ca,n)^{269}Hs reaction is E_α = 8.5 - 9.0 MeV. The average counting rate of α-particles within this energy interval was $5 \cdot 10^{-3}$ per minute within a 3-mm position window of each strip during the beam-off intervals. However, because of the relatively long half-life of ^{269}Hs ($T_{1/2}$ = 9.7 s [64, 103]), a relatively long time interval between EVR-like and α-like events for switching the beam off had to be used, resulting overall in a long beam-off period and hence a lower collected beam integral. Thus, over the whole experiment, about five random beam-off α-particles within the energy interval could follow random ER-α correlations in the same position within one minute. Six such ER-α-α_{off} events were found in the data which is in good agreement with the number of expected random correlated events. No further α-particles with E_α = 8.0 - 8.7 MeV in the same strip and position within the 3-min beam-off interval have been found.

The shorter decay branch of ^{269}Hs [66] that should be ended by spontaneous fission of ^{261}Rf was used to estimates the upper limit of the production cross section for the ^{226}Ra(^{48}Ca,5n)^{269}Hs reaction. The α-decay of the isotope ^{269}Hs leads to spontaneous fission of ^{261}Rf in 80% of all cases [63, 66], with an energy release of more than 100 MeV in most fissions. Also in SHE experiments of ^{48}Ca-induced complete fusion reactions with ^{238}U-^{249}Cf targets [104] the released energies during the SF exceeded 135 MeV in 81 of 84 cases observed. Furthermore, symmetric SF with a high energy release could be expected, because the products of the ^{226}Ra+^{48}Ca reaction are located near the neutron shell closure at N = 162. 20 high-energy events with E > 135 MeV have been registered, but only one of them was detected by both the focal-plane and the box detectors. Only a few of them should originate from SF, due to the 40%-detection efficiency of both SF fragments. Most of these high-energy events can be explained by scattered projectiles that were not registered by the TOF system. A lighter and faster particle compared with the EVR, passing the TOF, is losing less energy and creating less ionization and hence the TOF signal is much lower, sometimes less than the threshold.

In this experiment decay chains of the type EVR-α-SF (E_{EVR} = 7.5 - 16.5 MeV, E_α = 8.8 - 9.45 MeV, $\Delta t_{EVR-\alpha} \leq 60$ s, $E_{SF} > 135$ MeV, $\Delta t_{\alpha-SF} \leq 150$ s) were searched for to find decay chains of ^{269}Hs. Such chains were not found which results in an upper limit of the cross section for the 5n channel of the ^{48}Ca+^{226}Ra reaction of $\sigma_{5n} \leq 5.0$ pb. Also, concerning the $4n$ evaporation channel, no decay chains of ^{270}Hs were found. The upper cross section limit of the ^{226}Ra(^{48}Ca,$4n$)^{270}Hs reaction at that energy is $\sigma_{4n} \leq$ 3.6 pb.

Results at the intermediate excitation energy [97]

At the excitation energy of 40 MeV, two experiments were performed. This beam energy corresponds to the position of the calculated maximum of the $4n$ channel. A higher beam integral has been collected during the first experiment (see Table 3.1) and the magnetic rigidity of the separator was 2.29 Tm, which was about 1.8% larger than in all other experiments. Due to a three times larger beam integral but a 33% thinner target, the product of beam dose and target thickness (sensitivity) was about two times higher than that of the second one. In good agreement, four correlated decay chains of the type EVR-α-SF were observed in the first run and two in the second run. The measured parameters of the observed events are shown in Figure 4.4. The four decay chains on the left side were from the first run, the two on the right side were observed in the second series of runs. Energies of events detected by both the focal-plane and the box detectors are shown in brackets. For each α-particle the energy resolution (ΔE) is given.

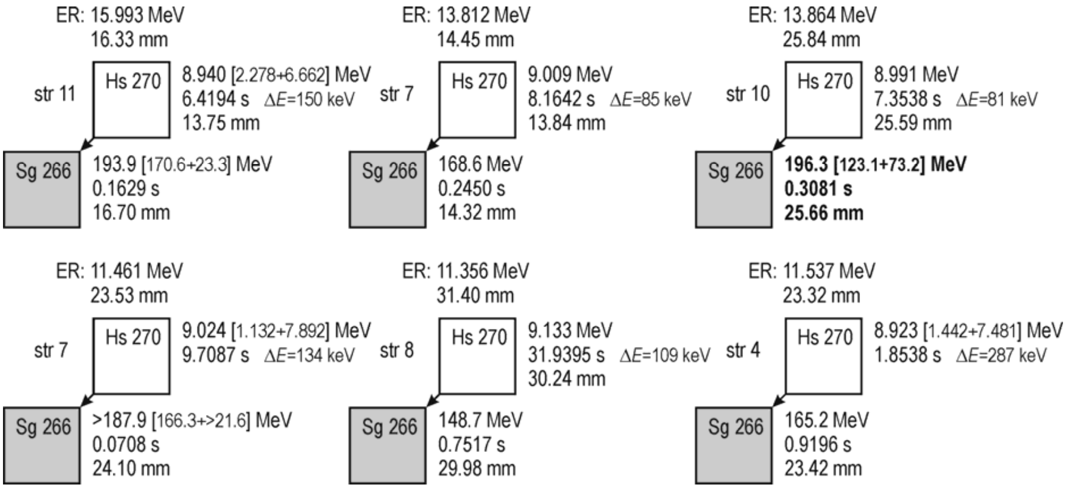

Figure 4.4: Decay chains observed in the ^{226}Ra+^{48}Ca reaction. Adapted from [97].

The larger part of the first experiment was performed without beam-off periods. In one decay chain observed in the second run the α-particle, escaping the focal-plane detector deposited an energy lower than the electronic threshold. Thus, that EVR-α chain did not switch the beam off. In another decay chain, the fission event was detected during the beam-off interval (right top). In one case (left bottom) the fission fragments were registered by both detectors. The energy of the fragment, detected in the side detector, exceeded the α-energy-scale interval but was not detected in the high-energy-scale interval. Hence, the fragment energy registered by the side detector was larger than 21.6 MeV, which is the upper limit of the α-energy-scale and hence, the total measured energy was larger than 187.9 MeV.

In the analysis of the data, seven chains of the type EVR-α-SF (E_{EVR} = 7.5 - 16.5 MeV, E_α = 8.7 - 9.5 MeV, $\Delta t_{EVR-\alpha} \leq 60$ s, $\Delta t_{\alpha-SF} \leq 400$ s) were revealed within position windows. One of these differs from the rest by a quite long α-SF correlation time of about 285 s, while all other chains exhibit correlation times of less than one second. This seventh EVR-α-SF decay chain (E_{EVR} = 15.3 MeV; E_α = 9.23 Mev, $\Delta t_{EVR-\alpha}$ = 40 s; E_{SF} = 137 MeV, $\Delta t_{\alpha-SF}$ = 285 s), could be considered as a candidate for the decay of ^{271}Hs. The half-life concerning an α-decay of ^{271}Hs, deduced from Q_α-systematics using the formalism reported in [56], should be of the order of four seconds [52] which is much lower than the measured value of 40 seconds. In addition, by increasing the EVR-SF position deviation up to ± 5 mm, five additional similar chains are observed which is in agreement with the number of expected randomly correlated events. Hence, at this ^{48}Ca projectile energy, an upper cross section limit for the ^{226}Ra(^{48}Ca,3n)^{271}Hs reaction of $\sigma_{3n} \leq 5.7$ pb (assuming $T_{1/2} \leq 10$ s for ^{271}Hs) can be deduced.

From the other six measured decay chains, an α-particle energy and half-life of the parent nucleus of $E_\alpha = 9.02 \pm 0.08$ MeV and $T_{1/2} = 7.6^{+4.9}_{-2.2}$ s can be deduced. The half-life of the spontaneously fissioning daughter nucleus corresponds to $0.28^{+0.19}_{-0.08}$ s. The decay chains were observed at an excitation energy of the compound nucleus (^{274}Hs) corresponding to the calculated maximum for the ^{226}Ra(^{48}Ca,4n)^{270}Hs reaction (see Figure 4.6 [41]). The decay properties of the observed nuclei agree very well with those reported for ^{270}Hs measured in the ^{248}Cm(^{26}Mg,4n)^{270}Hs reaction [51, 52]. ^{270}Hs should decay via α-decay with an α-particle energy of $E_\alpha = 8.88 \pm 0.05$ MeV followed by a SF of ^{266}Sg with a half-life of $T_{SF} = 0.36^{+0.19}_{-0.10}$ s. Therefore, the six observed decay chains were attributed to the decay of the nucleus ^{270}Hs. From both runs combined, an average cross section of $\sigma_{4n} = 8.3^{+6.7}_{-3.7}$ pb was obtained for the ^{226}Ra(^{48}Ca,4n)^{270}Hs reaction at an excitation energy of 40 MeV.

The total number of randomly correlated EVR-α-SF ($\Delta t \leq 1.4$ s, corresponding to five half-lives of the daughter nucleus) decay chains is less than 0.025. The doubly logarithmic distribution (number of events vs. time interval) for all EVR-like events followed by α-decays shown in Figure 4.4 and registered within two EVR-α or EVR-SF position resolutions is presented in Figure 4.5. For all measured six decay chains, 54 EVR-like events were found within a 4000-s time window, indicating that the total number of random EVR-like events detected during five half-lives of the parent nucleus is about 0.4. In the experiments also EVR-SF chains were found. There are two possible explanations for such chains, an escaping α-particle of the decay of ^{270}Hs or a SF decay branch for ^{270}Hs.

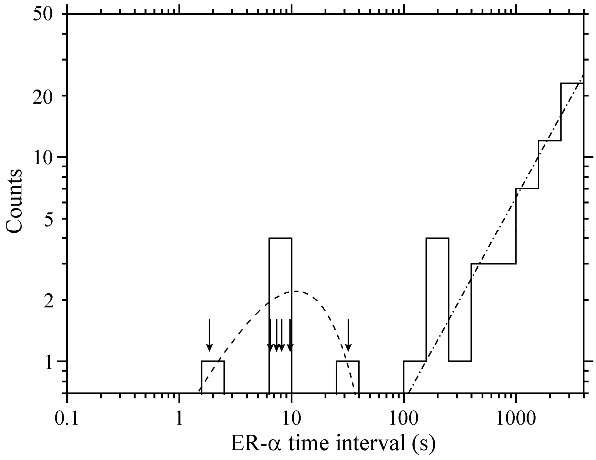

Figure 4.5: Time intervals between α-particles shown in Figure 4.4 and all the preceding ER-like events observed within two ER-α or ER-SF position resolutions ($\pm$ 2.35 standard deviations). Time intervals for the nearest ER events assigned to implantation of ^{270}Hs in detectors in Figure 4.4 are shown by arrows. The dashed line shows the distribution of dN/d(lg$_{10}$ t) for $T_{1/2}$=7.6 s. The dash-dotted line shows a linear fit for random ER-like events. Adapted from [97].

Concerning the first possibility, α-particles escaping from the focal-plane detector and entering into the box detector were registered by the focal-plane detector with an efficiency of 67% as determined for ^{217}Th produced in the calibration reaction ^{nat}Yb+^{48}Ca. Hence, in addition to the six observed decay chains of ^{270}Hs about three more decays could be detected without registration of the escaping α-particle in the focal-plane detector as EVR-SF chain. These α-particles can be detected in the side detector only. Due to the relatively long half-life of ^{270}Hs and the huge number of random α-like events in the energy range of α-particles emitted in the decay of ^{270}Hs, it is not possible to distinguish between the background and these real ^{270}Hs α-particles during beam-on periods.

A second explanation for the appearance of EVR-SF chains could be spontaneous fission of the even-even isotope ^{270}Hs. A SF half-life of 1.8 h is predicted in [54]. For Rf isotopes, these calculations are in good agreement with experimental T_{SF} values. For ^{256}Rf for example, the calculated value of $T_{SF} = 9.1$ ms is in very good agreement with the experimental value of $T_{SF} = 6.70 \pm 0.09$ ms. The calculated half-lives for Sg and Hs isotopes with N = 156-162 are similar but become gradually longer than those for Rf isotopes. The experimental values for Sg isotopes with N = 152-158 are lower than those for Rf isotopes. Also the T_{SF} value for ^{264}Hs, is lower by a factor of 20 than its lighter isotone ^{262}Sg. Hence, due to SF half-lives, systematically decreasing with increasing proton number, it cannot be excluded that the T_{SF} value for ^{270}Hs will be comparable with its partial α-decay half-life. In addition to six SF events shown in Figure 4.4, 40 additional high-energy events with $E > 135$ MeV were found in the data. Four of them were detected in the focal-plane as well as by the box detectors. From a 40%-detection efficiency of both SF fragments one can expect that about a quarter of these 40 events originates from SF. Hence, randomly correlated EVR-SF chains can be created by these SF-like events in combination with random recoils. Nevertheless, from an analysis concerning the time intervals between EVR-like and SF-like events according to [105] including all events attributed to the decay of ^{270}Hs, the existence of a SF activity of 4 - 12 events with a half-life of $3.5^{+4.3}_{-1.8}$ s can be assumed. The origin of this activity can be assigned most likely to ^{252}No which is producted from ^{48}Ca induced fusion reactions with ^{206}Pb impurities contained in the target. Due to the age of the target material, the FLNR has received the radium (^{226}Ra) more than 50 years ago, it had to be purified before a preparation of the target took place. This was done by the coprecipitation with iron hydroxide and ion-exchange chromatography to separate admixtures of different elements. Unfortunately, the separation from lead did not exceed a factor of 10. About 1% of ^{226}Ra atoms decayed to ^{206}Pb. The consequence is a quite high yield of byproducts from nuclear reactions with ^{206}Pb, especially products from the complete nuclear fusion reaction ^{48}Ca+^{206}Pb.

Results at the lowest excitation energy [97]

Finally, one experiment was performed at an excitation energy of 36 MeV. As mentioned before, due to a lead contamination of the target material, created by the radioactive decay of ^{226}Ra, up to 1% of the target material consisted of ^{206}Pb. The cross section of the $2n$ evaporation channel of the reaction ^{206}Pb(^{48}Ca,$2n$)^{252}No at $E^* = 36$ MeV is about 30 nb [106], which is quite high compared with the expected cross sections of the reaction ^{48}Ca+^{226}Ra, which should be of the order of some pb. However, the higher magnetic rigidity in the present experiment (Bρ = 2.335 Tm) compared with the optimal value for the ^{206}Pb+^{48}Ca reaction (Bρ = 2.12 Tm), is reducing the collection efficiency for ^{252}No by a factor of 4 to 5. Hence, one could expect more than five SF decays of ^{252}No in the data. In agreement with these estimations 5 - 15 SF events with a half-life of $4.2^{+4.0}_{-2.1}$ s [105] were found in the data.

53 high energy events with E > 135 MeV have been observed in this experiment, 16 of them were detected by the focal-plane detector, as well as by the box detectors. Hence, due to the efficiency, about 40 events could originate from SF. The total yield of SF events increases with decreasing projectile energy. Hence, these events could be assigned to SF of lower-Z nuclei produced in reactions of ^{48}Ca with target impurities like the aforementioned ^{206}Pb.

Similar to the experiments at an excitation energy of E* = 40 MeV, correlated chains of the type EVR-α-SF (E$_{EVR}$ = 7.5 - 16.5 MeV; E$_\alpha$ = 8.7 - 9.5 MeV, Δt$_{EVR-\alpha}$ $\leq$ 60 s; Δt$_{\alpha-SF}$ $\leq$ 400 s) within position windows were searched for to identify decaying ^{271}Hs. Four correlated events were found with decay properties similar to those measured for the decay of ^{271}Hs [52]. By increasing the position deviation of EVR-SF correlations up to ± 5 mm an increase in the number of similar chains can be observed. Hence, all these chains cannot be statistically separated from randomly correlated events and have to be discarded. At the same time, no chains with fission events registered during beam-off periods have been observed and hence, only an upper cross section limit can be given for the ^{226}Ra(^{48}Ca,3n)^{271}Hs reaction. Due to the unknown half-life of ^{271}Hs, the upper limit differs according to the chosen half-lives of ^{271}Hs. An EVR-α time interval of 8 s for beam off periods has been applied in the experiment, which corresponds to two half-lives of ^{271}Hs estimated in [52]. For T$_{1/2}$(^{271}Hs) = 4 s the upper cross section limit is σ_{3n} $\leq$ 4.2 pb. If the half-life of ^{271}Hs is lower than T$_{1/2}$(^{269}Hs), similar to the neighboring Ds isotopes with N = 161 and 163 (T$_{1/2}$(^{271}Ds) = 1.63 ms [101], T$_{1/2}$(^{273}Ds) = 0.17 ms [64, 103]), a half-life of T$_{1/2}$(^{271}Hs) = 1 s would result in an upper cross section limit of σ_{3n} $\leq$ 3.2 pb. If the half-life of ^{271}Hs would be larger than that for ^{269}Hs like ten seconds or more the upper cross section limit increases to σ_{3n} $\leq$ 6.9 pb.

Also at this measured excitation energy, no EVR-α-SF decay chains of ^{270}Hs have been observed. An upper cross section limit of the ^{226}Ra(^{48}Ca,4n)^{270}Hs reaction of σ_{4n} $\leq$ 1.6 pb can be deduced.

4.2.2 Excitation function of the complete fusion reaction ^{48}Ca+^{226}Ra

The excitation function of the nuclear reaction ^{226}Ra(^{48}Ca,3-5n)$^{269-271}$Hs (see Figure 4.6) has been measured at three different excitation energies of E* = 36 MeV, 40 MeV, and 46 MeV. Only the 4n channel corresponding to the production of ^{270}Hs has been observed at E* = 40 MeV by measuring six decay chains of ^{270}Hs. Neither the 3 n nor the 5n evaporation channel has been found during the two experimental campaigns. At the highest and the lowest examined excitation energies no decay chains of any of these Hs isotopes have been found.

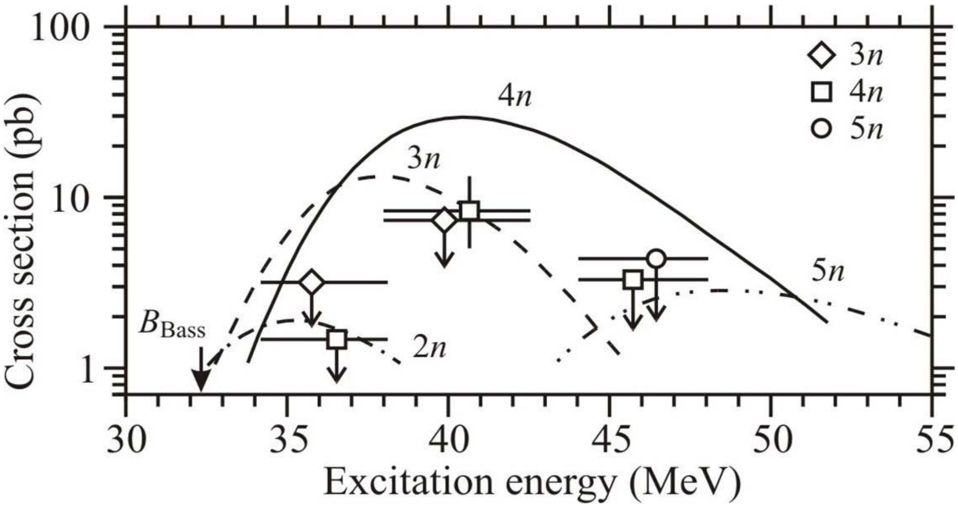

Figure 4.6: Excitation functions for the 2n- to 5n-evaporation channels of the complete-fusion reaction ^{226}Ra+^{48}Ca. The Bass barrier B_{Bass} [28] is shown by an arrow. Lines show results of calculations [41]. Error bars correspond to statistical uncertainties. Adapted from [97].

The measured cross section for the 4n evaporation channel at E* = 40 MeV of σ_{4n} = $8.3^{+6.7}_{3.7}$ pb, as well as both 4n cross section limits of $\sigma_{4n} \leq 1.6$ pb (E* = 36 MeV) and $\sigma_{4n} \leq 3.6$ pb (E* = 46 MeV) are much smaller than calculations predicted before [43, 41]. Also the measured cross section limits for the 3n channel of $\sigma_{3n} \leq 5.7$ pb (E* = 40 MeV) and $\sigma_{3n} \leq 3.2$ pb (E* = 36 MeV) are significantly lower than the predicted values. The cross section limit of the 5n evaporation channel is higher than the predicted values.

4.3 Discussion of the measured excitation functions

As described in Section 1.3.2, the cross section for evaporation residue production in nuclear fusion reactions can be described as the sum over all partial waves of the product of the penetrability of the multidimensional Coulomb barrier, the probability of compound nucleus formation and the survival probability during the de-excitation of the compound nucleus via successive neutron evaporation. While the first two terms of the product reflect the formation process (entrance channel), the third term depends on the properties of the CN and members of the evaporation cascade. As all fusion reactions, ^{36}S + ^{238}U, ^{48}Ca+^{226}Ra, and ^{26}Mg + ^{248}Cm result in the same CN (^{274}Hs), the exit channel is nearly identical for all these reactions at the same excitation energy (neglecting small differences in angular momentum of the compound nucleus after its formation) and could not explain possible differences in the cross sections. Hence, they must be due to the entrance channel. Since the incident energy of the projectile is above the fusion barrier, the production cross section only depends on the compound nucleus formation probability (P$_{CN}$). As described in Section 1.3, this mainly depends on the reaction asymmetry and the Q-value. Bass barrier, $(B-Q)$-values and reaction asymmetry $(Z_1 \cdot Z_2)$ for all aforementioned reactions leading to the CN ^{274}Hs are displayed in Table 4.1.

Table 4.1: Bass barrier, Q-value, $(B-Q)$-values, $Z_1 \cdot Z_2$ and measured maximum cross section for various reactions leading to the CN ^{274}Hs

Reaction	B [MeV]	Q [MeV]	(B-Q) [MeV]	$Z_1 \cdot Z_2$	$\sigma_{4n\ max}$ [pb]	$\sigma_{5n\ max}$ [pb]
^{26}Mg + ^{248}Cm	126.9	-82.2	44.7	1152	2.8 (E*=40 MeV)	6.9 (E*=49 MeV)
^{30}Si + ^{244}Pu	144.0	-98.0	46.0	1316	-	-
^{36}S + ^{238}U	159.1	-116.7	42.4	1472	0.8 (E*=51 MeV)	$<$ 2.9 (E*=51 MeV)
^{48}Ca + ^{226}Ra	187.0	-153.9	33.1	1760	8.3 (E*=40 MeV)	$<$ 5.0 (E*=46 MeV)

The aim of this work was to find an answer to the question which of the two parameters dominating P$_{CN}$ has the largest impact on the production of SHE and in which energy range. Including both reactions examined in this work, excitation functions of the three reactions listed in Table 4.1 have been measured so far. The excitation function for the reaction ^{26}Mg + ^{248}Cm has been measured at five different beam energies in the framework of [8] and can be found in Figure 4.7.

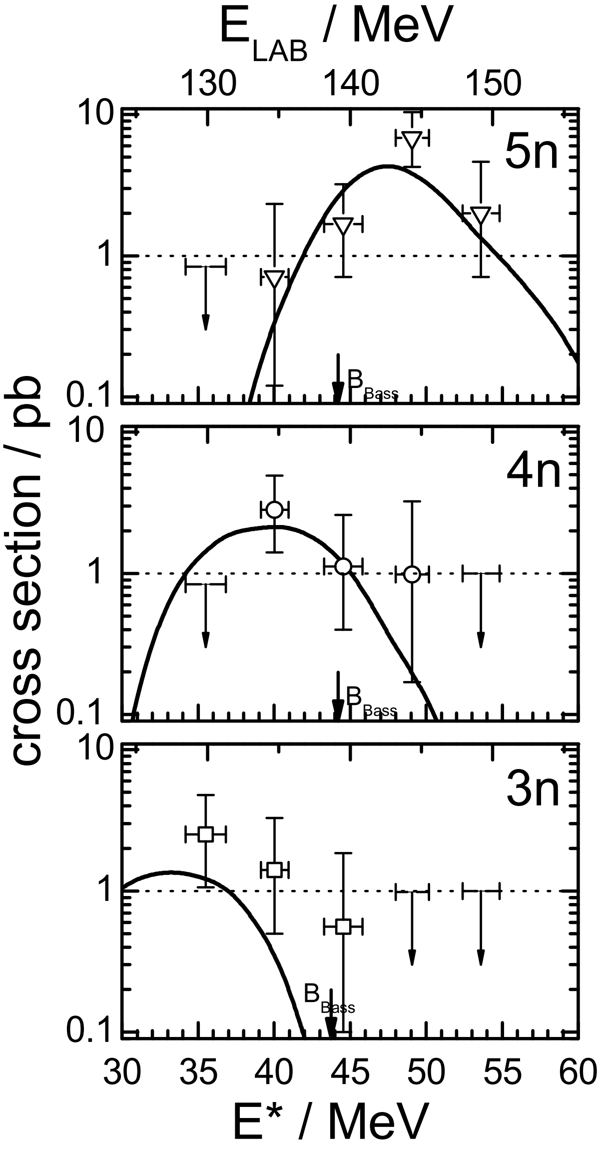

Figure 4.7: Excitation functions for the $3n$- to $5n$-evaporation channels of the complete-fusion reaction ^{248}Cm+^{26}Mg. The Bass barrier B_{Bass} [28] is shown by an arrow. Lines show results of HIVAP calculations [44]. Error bars correspond to statistical uncertainties. Adapted from [8].

The largest cross section maximum was measured for the $5n$ channel with 7 pb. The measured maximum cross section of the $3n$ channel is comparable with that of the $4n$ channel, both about 3 pb. This fact is remarkable, since the $3n$ channel is usually significantly suppressed in hot fusion reactions. Surprisingly, the maximum of the $3n$ channel situates about 8 MeV below the Bass barrier ($E_{Bass} = 44.7$ MeV). This effect of large production cross sections for incident energies below the barrier is caused by large sub-barrier fusion enhancement, which has not only been observed in the reaction ^{26}Mg + ^{248}Cm [52] but also in recent experiments concerning orientation and coupled channels effects on the production of superheavy elements in fusion reactions with ^{238}U targets [68, 107, 108]. Several theoretical calculations predicted such a significant enhancement of sub-barrier fusion cross sections [25, 109, 110]. The subbarrier fusion enhancement is caused by nuclear deformations of projectile and target nuclei and results in two different modes of fusion, polar and equatorial configurations for strongly deformed fusioning nuclei. As shown in [107], near polar orientations of the target nucleus concerning the projectile do not contribute to fusion, they mainly lead to quasi-fission and hence to a suppression. On the other side sub-barrier fusion enhancement is caused by coupled channel effects of collective excitations of projectile and target nucleus.

Due to the measured sub-barrier enhancement for fusion reactions dealing with ^{16}O and ^{30}Si projectiles and ^{238}U targets, such effects could be also expected for the reaction $^{36}\mathrm{S} + ^{238}\mathrm{U}$. This was not observed in our experiment. During the experimental campaign on the reaction $^{36}\mathrm{S} + ^{238}\mathrm{U}$, one ^{270}Hs event at $E^* = 51$ MeV has been observed, above the Coulomb barrier, where the difference in the CN formation probability, which depends mainly on the asymmetry of the projectile - target combination, is expected to be the dominant factor. The measured cross section and cross section limits in combination with HIVAP calculations can be found in Figure 4.2. The cross section of the $4n$ evaporation channel for this event is about 0.8 pb. The one event cross section limits (68% confidence interval) for the $3n$, $4n$, and $5n$ evaporation channels at $E^* = 39$ MeV are 2.9 pb, while the cross section limits of the $3n$ and $5n$ channel at $E^* = 51$ MeV are 1.5 pb. These are comparable ($4n$) or even lower ($5n$) than the cross sections of the $^{26}\mathrm{Mg}+^{248}\mathrm{Cm}$ reaction at a similar excitation energy. For the reaction $^{48}\mathrm{Ca} + ^{226}\mathrm{Ra}$, no sub-barrier enhancement was expected, due to nearly spherical projectile and target nucleus. This is also confirmed by the experiments. At $E^* = 36$ MeV, neither a $3n$ channel nor a $4n$ channel event has been measured resulting in upper limits for the EVR production cross section of $\sigma_{3n} \leq 1.6$ pb and $\sigma_{4n} \leq 3.2$ pb. At $E^* = 40$ MeV, the $4n$ evaporation channel is dominant (see Figure 4.6) with a very high cross section of $\sigma_{4n} = 8.3^{+6.7}_{-3.7}$ pb, which is about a factor of three times higher than the cross section for the same channel and energy for the reaction $^{26}\mathrm{Mg} + ^{248}\mathrm{Cm}$ and even higher than for the reaction $^{36}\mathrm{S} + ^{238}\mathrm{U}$. The latter exhibits the lowest cross section of all three reactions at $E^* = 40$ MeV. According to Table 4.1, that energy is situated below but near the barrier for the reactions ^{26}Mg + ^{248}Cm (ΔE = E*-(B-Q) = -4.7 MeV) and ^{36}S + ^{238}U (ΔE = E*-(B-Q) = -2.4 MeV). Due to its large Q-value, the reaction ^{48}Ca + ^{226}Ra situates above the barrier (ΔE = E*-(B-Q) = +6.9 MeV) providing the largest cross section. Hence at lower energies near the barrier, the (B-Q)-value and therefore the Q-value becomes the dominant parameter for the production cross section.

At higher excitation energies, this picture has completely changed. At E* $\approx$ 50 MeV, the reaction ^{26}Mg + ^{248}Cm has the highest production cross section of all three reactions with a maximum of about σ_{5n} = 7 pb. In both reactions, ^{36}S + ^{238}U as well as ^{48}Ca + ^{226}Ra, only upper cross section limits could be established $\sigma_{5n} \leq 1.5$ pb and $\sigma_{5n} \leq 5.0$ pb, respectively. Again, it seems that the reaction ^{36}S + ^{238}U exhibits the lowest cross section of all three reactions, but since we have only estimated upper limits for the production cross sections for both reactions, this conclusion cannot be made in this case. The dominant conclusion for this energy is, that at higher excitation energies, the compound nucleus formation probability and hence the production cross section is mainly driven by the reaction asymmetry, because of the large measured cross section for the most asymmetric reaction ^{26}Mg + ^{248}Cm.

Both these main conclusions for hot fusion reactions on the dependence of the compound nucleus formation probability are qualitatively in good agreement with measurements and theoretical predictions for cold fusion reactions [41]. Zagrebaev [41] reports, as described in Section 1.3.3, that the compound nucleus formation probability has on the one hand a strong energy dependence, which is proportional to the position of the barrier and therefore to the (B-Q)-value and, on the other hand, is strongly dependent on the reaction asymmetry ($Z_1 \cdot Z_2$ in [41]). Qualitatively, this relation is also valid for hot fusion reaction [42], which is reproduced by the comparison of all three fusion reactions.

In general, if the position of the fusion barrier is neglected, the maximum production cross section for the evaporation of an additional neutron decreases by one order of magnitude. This is caused by the competition between neutron evaporation and fission of the excited nucleus for any further evaporated neutron, as long as the excitation energy is higher than the fission barrier. The survival probability of the EVR during each single neutron evaporation is determined by the ratio of the decay width for neutron evaporation (Γ_n) and the total decay width (Γ_{tot}), which is mainly influenced by the decay width for SF (Γ_f) [26]:

$$P_{sur}({}^{\mathrm{A}}_{\mathrm{Z}}\mathrm{X} \rightarrow {}^{\mathrm{A-1}}_{\mathrm{Z}}\mathrm{X} + n) \sim \frac{\Gamma_n}{\Gamma_{tot}} \sim \frac{\Gamma_n}{\Gamma_f} \qquad (4.1)$$

This ratio amounts for most reactions to 1/10. Hence, each step of neutron evaporation reduces the EVR cross section by about a factor of 10.
If two fusion reactions with different reaction asymmetries ($Z_1 \cdot Z_2$ low, $Z_1 \cdot Z_2$ high) are compared in this frame, the production cross section at a certain excitation energy for a certain channel is always about the same factor lower for the more symmetric reaction (see Figure 4.8).

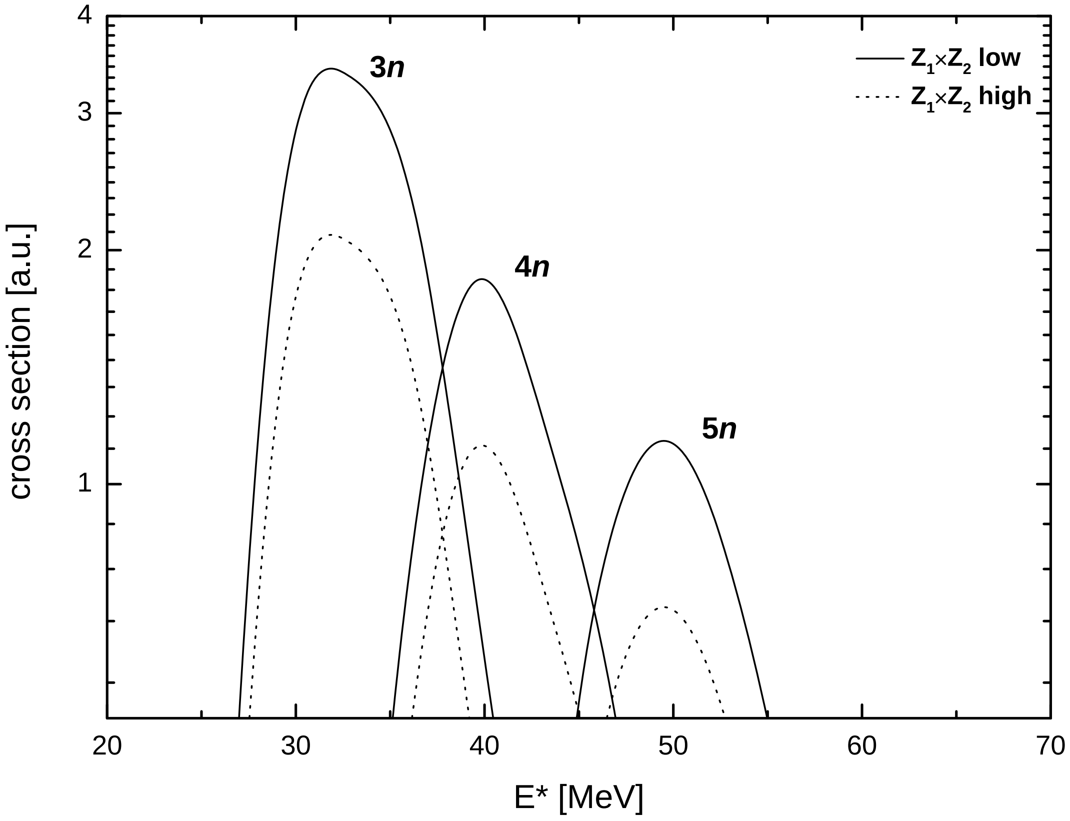

Figure 4.8: Comparison of the excitation functions of two different reaction with different reaction asymmetries ($Z_1 \cdot Z_2$ low, $Z_1 \cdot Z_2$ high)

This is caused by the reduced fusion probability in the latter case, which depends on the reaction asymmetry (see equation (1.28)). The fusion probability (P_{CN}) increases exponentially with increasing excitation energy (see equation (1.27)) to a saturation plateau, which is situated a few MeV above the barrier (see Figure 4.9). According to equation (1.28), the saturation level of P_{CN} and hence the maximum fusion cross section depends on the asymmetry of the reaction ($Z_1 \cdot Z_2$).

The second main factor on the fusion probability is the excitation energy at the barrier (E^*_B), which corresponds to the (B-Q)-value. This value defines at which excitation

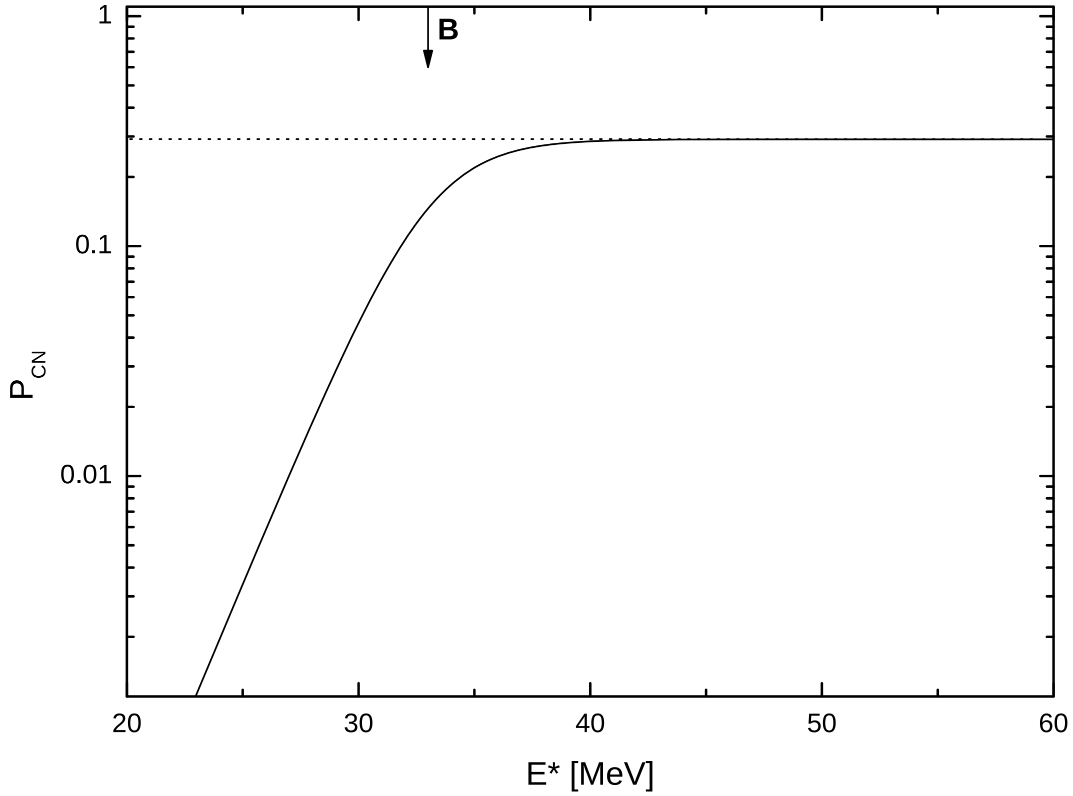

Figure 4.9: Fusion probability dependence on the excitation energy. The barrier is indicated by an arrow, the dotted line represents the saturation level.

energy the aforementioned saturation takes place. If for example the barrier position is high (E* = 40-50 MeV), maximum cross sections of lower evaporation channels (e.g. $3n$) are significantly lower, due to a reduced fusion probability. At the maximum of such an excitation function, the saturation of the fusion probability has not been reached, decreasing the production cross section. Hence, by comparing two reactions, one very asymmetric with a high (B-Q)-value and one more symmetric with a lower (B-Q)-value, it is possible, that the latter is dominant for the energetically lower lying evaporation channels (e.g. $3n$ or $4n$) since the former is dominant for higher evaporation channels (e.g. $5n$). Such a comparison can be found in Figure 4.10.

At lower excitation energies (E* $\approx$ 40 MeV), the $4n$ channel excitation function for the more asymmetric reaction ($Z_1 \cdot Z_2$ low) is cut off by the barrier, the fusion probability is not saturated and the more symmetric reaction ($Z_1 \cdot Z_2$ high), where the fusion probability is saturated, is dominant. At higher excitation energies (E* $\approx$ 50 MeV) for the $5n$ channel, an opposite trend can be observed. At that energy the fusion probability of the more asymmetric reaction has reached the saturation level, which is much higher, than that of the more symmetric reaction.

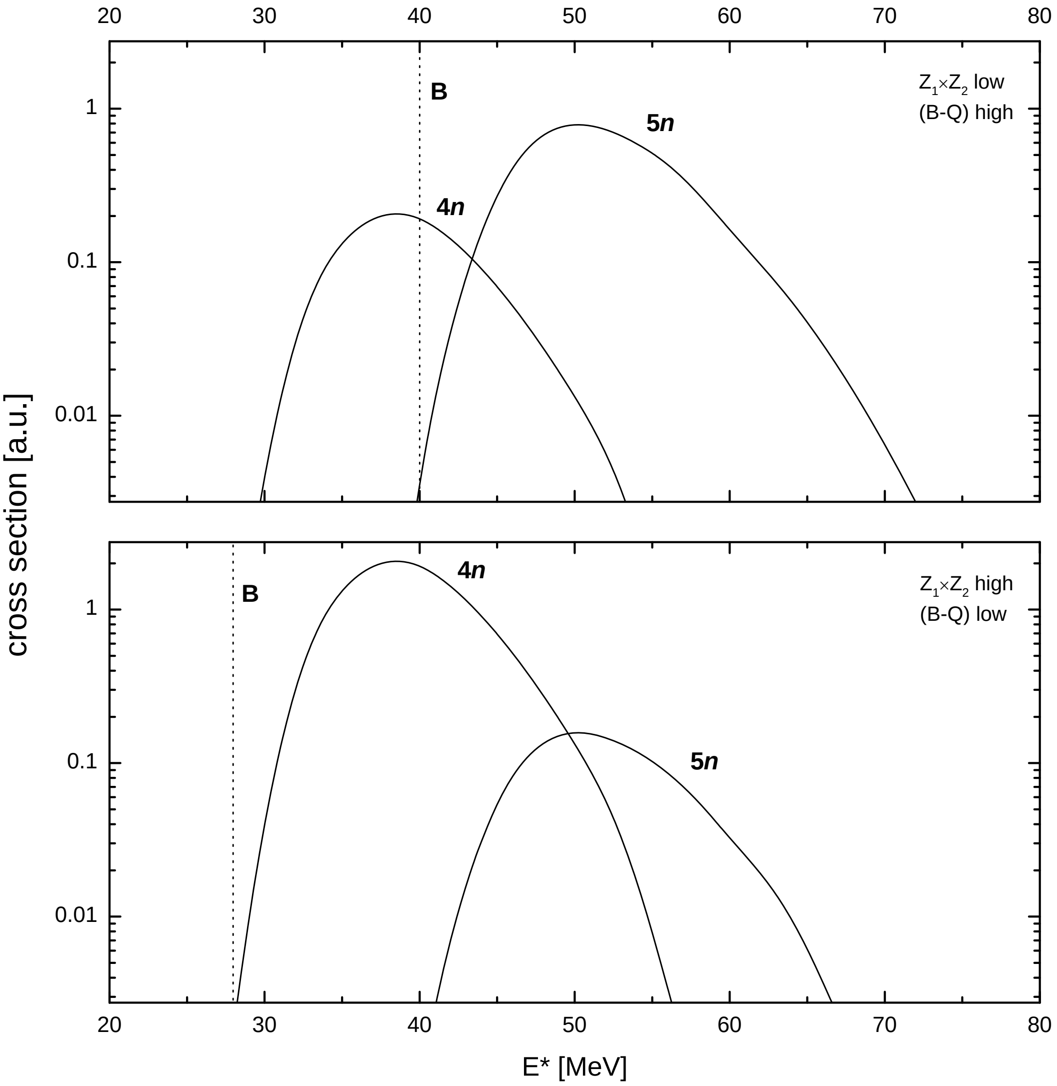

Figure 4.10: Comparison of the excitation functions of two different reaction with different reaction asymmetries ($Z_1 \cdot Z_2$ low, $Z_1 \cdot Z_2$ high) and different (B-Q)-values

The impact of the reaction asymmetry on the one side and the (B-Q)-value on the other side on the reactions investigated in this work can be seen in Figure 4.11. It should be mentioned, that this graph is only reproducing the systematic physical conclusions, but it is not reproducing the exact physical situation, e.g. exact values. While the saturation levels for higher excitation energies are proportional to the reaction asymmetry, the energy at which this level is reached is defined by the (B-Q)-value. Hence, the fusion probability near the excitation energy of E* = 40 MeV is largest for the reaction ^{48}Ca + ^{226}Ra, it is in the area of saturation. This is not the case for the other two reactions ^{26}Mg + ^{248}Cm and ^{36}S + ^{238}U, whose fusion probabilities are still increasing and much lower at E* = 40 MeV. Hence the production cross section of the $4n$ channel is largest for the reaction ^{48}Ca + ^{226}Ra, which is confirmed by the experiments.

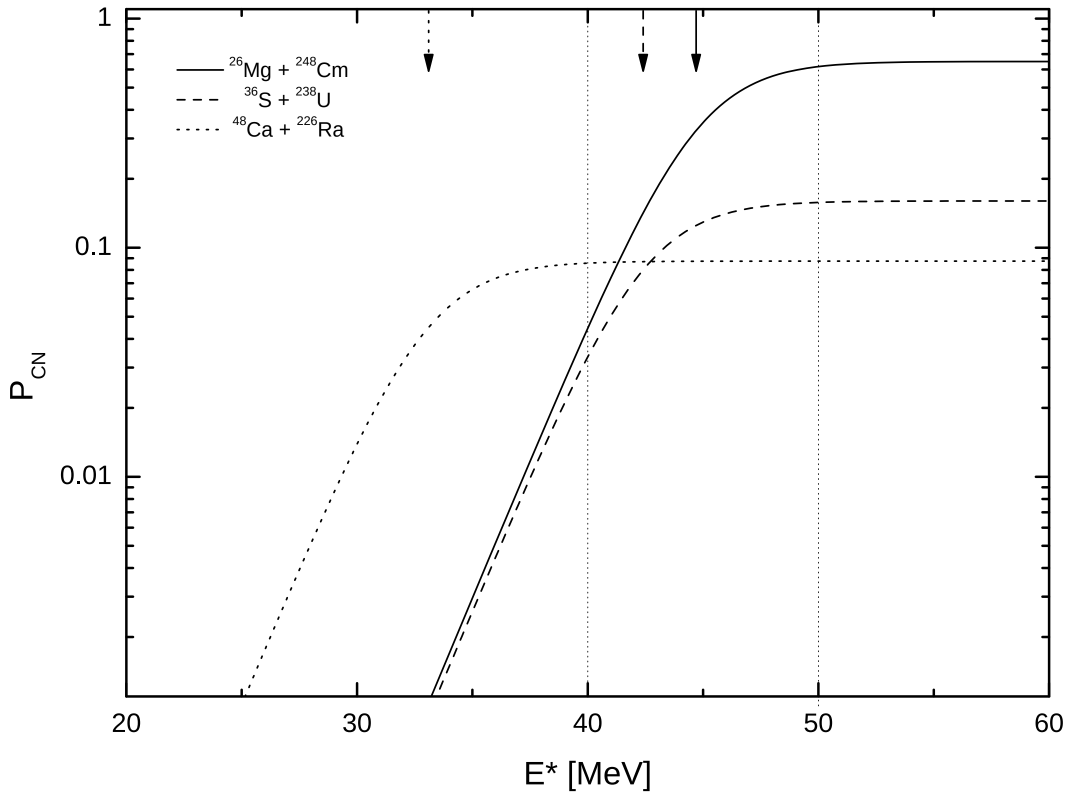

Figure 4.11: Systematic comparison of the fusion probability of all three different reaction with different reaction asymmetries and different (B-Q)-values. Arrows indicate the particular (B-Q)-values.

Near the excitation energy of E* = 50 MeV, this picture has changed and also the reactions ^{26}Mg + ^{248}Cm and ^{36}S + ^{238}U have reached the saturation level. Hence, the fusion probability is now only depending on the reaction asymmetry. Therefore, the reaction ^{26}Mg + ^{248}Cm provides now the largest production cross section, while that for the reaction ^{48}Ca + ^{226}Ra should be lowest. The yield for ^{36}S + ^{238}U should be in between both reactions. This correlation is also in agreement with the experiments.

In summary, for an excitation energy near the maximum of the $4n$ channel, the (B-Q)-dependence becomes the dominant effect concerning the production cross section.

Due to a very low (B-Q)-value of only 33.1 MeV, the reaction ^{48}Ca + ^{226}Ra provides the highest cross section for the $4n$ channel, since at that energy (E* ≈ 40 MeV) the energy of the system is about 6.9 MeV above the barrier resulting in a saturation of the fusion probability. By increasing the energy to a value near the maximum of the $5n$ evaporation channel, the reaction asymmetry is mainly influencing the production cross section, since the fusion probability is saturated for all reactions. Hence, the most asymmetric reaction ^{26}Mg + ^{248}Cm provides highest cross section in this energy range.

Another result of the analysis is the conclusion about the impact of small deviations of both parameters. Compared with the reaction ^{26}Mg + ^{248}Cm, ^{36}S + ^{238}U has a slightly better (B-Q)-value, but a much worse asymmetry as can be seen from Table 4.1. In contrast to calculations from Liu *et al.* [43] the impact of the reaction asymmetry is much stronger, than small differences in (B-Q)-values. While Liu *et al.* [43] predicted ^{36}S + ^{238}U to have cross sections of the order of the reaction ^{48}Ca + ^{226}Ra, with a two times higher maximum production cross section than the reaction ^{26}Mg + ^{248}Cm, this is not confirmed by our measurements. The reaction ^{26}Mg + ^{248}Cm has at least the same or even larger cross section for any channel compared to the reaction ^{36}S + ^{238}U. Also sub-barrier fusion enhancement does not take place in the reaction ^{36}S + ^{238}U resulting in the lowest measured cross section for all measured channels for this reaction. ^{48}Ca + ^{226}Ra on the other hand has the worst asymmetry of all examined reactions. But due to the very low (B-Q)-value, which is more than 10 MeV lower than for the other two reactions, this reaction offers highest cross section in the medium energy range.

A third factor influencing the production cross section is the deformation of projectile and target, which are very important for energies below the barrier. In the case of strongly deformed nuclei, large sub-barrier fusion enhancement has been observed in recent experiments. This effect is responsible for the large $3n$ channel cross sections of the reaction ^{26}Mg + ^{248}Cm. For the two other reactions, with spherical projectiles, such effects have not been observed.

4.4 New results on decay properties of hassium isotopes near N=162 and their daughters

The investigation of the decay properties of the Hs isotopes $^{269-271}$Hs and their daughter nuclei was conducted in the framework of [8]. The decay properties of ^{269}Hs and its daughters ^{265}Sg and ^{261}Rf were remeasured and reassigned, while the decay properties of ^{270}Hs and its daughter ^{266}Sg as well as ^{271}Hs and daughters ^{267}Sg and ^{263}Rf were measured and assigned for the first time. A summary of these decay properties obtained in former experiments can be found in Table 4.4. In the framework of the current thesis, seven additional decay chains of ^{270}Hs have been measured. One chain in the experiment on the reaction $^{36}\mathrm{S}+{}^{238}\mathrm{U}$ (see Figure 4.1) and six in the two experiments on the reaction $^{48}\mathrm{Ca}+{}^{226}\mathrm{Ra}$ (see Figure 4.4). In addition, in the latter experiment, the half-life of ^{270}Hs has been measured for the first time.

Table 4.2: Decay properties derived from the decay chains detected in former TUM experiments on Hs chemistry in comparison with previously known experimental decay properties. Adapted from [8].

Nuclide	Data from previous exp.			Data from TUM Hs chem. exp.		
	Dec. mode, branching[a]	$T_{1/2}$	E_α [MeV]	Dec. mode, branching[a]	$T_{1/2}$	E_α [MeV]
^{269}Hs	α	9.7 s	9.23	α		9.13 ± 0.05
			9.18			8.95 ± 0.05
^{270}Hs	α	~3.6 s	9.16	α	~23.0 s[b]	8.88 ± 0.05
^{271}Hs				α		9.30 ± 0.04
						9.13 ± 0.05
^{265}Sg	α	8 s	8.69-8.94	α	$15.3^{+7.1}_{-3.7}$ s	8.69 ± 0.04
^{266}Sg	α	18.8 s	8.52-8.77	SF	359^{+248}_{-104} ms	
^{267}Sg				α/SF: 0.17/0.83	$84.3^{+58.1}_{-24.2}$ s	8.20 ± 0.03
^{261b}Rf	α/SF: 0.60/0.40	5 s	8.52	α/SF: 0.09/0.91	$2.5^{+1.1}_{-0.6}$ s	8.51 ± 0.03
^{261a}Rf	α	78 s	8.28	α	22^{+106}_{-10} s[c]	8.29 ± 0.03
^{263}Rf	SF	11 m		SF	$8.3^{+39.8}_{-3.8}$ s	

---

[a] Branching is not shown, if only one decay mode was observed.

[b] Half-life calculated from the measured E_α values using [56]

[c] Derived from 1 event, in agreement with known $T_{1/2} = 78$ s [111, 112].

From all six measured ^{270}Hs decays, using the formalism described in [100], a half-life for ^{270}Hs of $T_{1/2} = 7.6^{+5.3}_{-2.2}$ s is derived. Former chemical experiments were not able to measure the half-life, it could only be calculated according to the formula presented in [56]. All measured chains consisted of an α-decay of ^{270}Hs followed by a SF of the daughter nuclide ^{266}Sg. For the α-decay of ^{270}Hs an α-particle energy of $E_\alpha = 8.88 \pm 0.05$ was determined in [8]. In our chemistry experiment we measured for the one single event of ^{270}Hs an α-particle energy of $E_\alpha = 9.02^{+0.50}_{-0.1}$ MeV which is slightly higher, but in good agreement with the results reported from the ^{26}Mg + ^{248}Cm experiment. The results from the experiments on the reaction ^{48}Ca + ^{226}Ra, where an α-particle energy of $E_\alpha = 9.00 \pm 0.14$ MeV has been measured, fit quite perfectly with the results obtained from the ^{36}S+^{238}U reaction and also agree with the ^{26}Mg+^{248}Cm experiment. Taking all 13 ^{270}Hs decays from all three reactions into account, an α-particle-energy of $E_\alpha = 8.95 \pm 0.10$ MeV can be deduced. In all experiments the daughter nucleus ^{266}Sg decays via SF. The half-life of that isotope obtained from the ^{36}S+^{238}U measurement of $T_{1/2}(^{266}\text{Sg}) = 23$ ms is relatively short compared with the value of $T_{1/2}(^{266}\text{Sg}) = 359^{+248}_{-104}$ ms reported from [8]. The half-life observed in experiments on the reaction ^{48}Ca + ^{226}Ra of $T_{1/2}(^{266}\text{Sg}) = 284^{+196}_{-83}$ ms (error corresponding to a 1σ interval see [100]) agrees very well within error limits with the results from [8]. Using the formalism described in [100], the results from all three experiments can be combined and a half-life for ^{266}Sg of $T_{1/2} = 298^{+115}_{-65}$ ms is obtained.

The results on the decay properties of ^{270}Hs from both experiments examined in this thesis confirm the properties reported in [8]. A summary can be found in Table 4.3. The Hs isotopes ^{269}Hs and ^{271}Hs have not been observed in the framework of this thesis. Hence, there are no new results on their decay properties.

Table 4.3: Updated decay properties of ^{270}Hs and its daughter ^{266}Sg

Nuclide	decay mode	$T_{1/2}$	E_α [MeV]
^{270}Hs	α	$7.6^{+5.3}_{-2.2}$ s	8.95 ± 0.10
^{266}Sg	SF	298^{+115}_{-65} ms	

Chapter 5

Conclusions and outlook

The aim of the research performed in the framework of this thesis was to study the influence of the reaction Q-value on the yield of SHE producted in complete nuclear fusion reactions. This was accomplished by studying three fusion reactions leading to ^{274}Hs as compound nucleus. The $4n$ evaporation channel is leading to the doubly magic nucleus ^{270}Hs. Since for one of the three reactions the excitation function has been measured in the framework of [8], excitation functions of both reactions ^{48}Ca + ^{226}Ra as well as ^{36}S + ^{238}U were investigated in this thesis and compared with theoretical predictions from [43]. These reactions have been measured at two and three different excitation energies, respectively. While the reaction ^{36}S + ^{238}U was investigated using our well established chemical separation and detection system COMPACT, the reaction ^{48}Ca + ^{226}Ra was measured in a separator experiment at the DGFRS in collaboration with the FLNR, Dubna, Russia. In total seven decay chains of ^{270}Hs have been measured, one in the experimental campaign on the first reaction and six in the two experimental campaigns on the second reaction. In the DGFRS experiment, the half-live of ^{270}Hs could be measured for the first time and was derived to be $T_{1/2} = 7.6^{+5.3}_{-2.2}$ s [97]. Other known decay properties of ^{270}Hs and its daughter ^{266}Sg [51] were confirmed.

In agreement with predictions from [43], the reaction ^{48}Ca + ^{226}Ra offers a large maximum $4n$ evaporation cross section of more than 8 pb. The reaction ^{26}Mg + ^{248}Cm provides a lower value of about 3 pb and an upper cross section limit of <3 pb was estimated for the reaction ^{36}S + ^{238}U, in contrast to predictions. For the $5n$ channel this picture changed, the reaction ^{26}Mg + ^{248}Cm has the largest cross section with about 7 pb, while only cross section limits could be estimated for both other reactions.

These experimental results are in a good agreement with explanations presented in Section 4.3 concerning the (B-Q)- and asymmetry influence on the production cross sections. In general at energies close to the maximum of the $5n$ channel, for all (B-Q)-values and barrier positions, the fusion probability (P_{CN}) has reached its maximum value (see e.g.Figure 4.11) since it is saturated, independent of the excitation energy and only depends on the asymmetry of the reaction. It is very important to note that P_{CN} and hence the production cross section for the $5n$ channel is independent of the (B-Q)-value, since the excitation energy is about several MeV above the barrier (see equation (1.27)). This was confirmed by the measurements. The most asymmetric reaction ^{26}Mg + ^{248}Cm provides much larger cross sections than the more symmetric reactions ^{36}S + ^{238}U and ^{48}Ca + ^{226}Ra. The very low (B-Q)-value of the latter reaction is not affecting the production cross section at all in this energy range.

In contrast to the $5n$ channel, for energies close to the maximum of the $4n$ channel, the barrier position, or (B-Q)-value (Q-value effect) has a deep impact on the fusion probability and hence on the production cross section. Hence, the (B-Q)-value changes the $\frac{\sigma_{4n}}{\sigma_{5n}}$ ratio. For "hot" fusion reactions the $4n$ channel is cut-off due to large (B-Q)-values and P_{CN} resides in the region of strongly increasing values and far away from its maximum value. For "warm" fusion reactions (^{48}Ca-based), the (B-Q)-value is low and the fusion probability has already reached its maximum value (saturation). This correlation is well reproduced by our measurements, since the reaction ^{48}Ca + ^{226}Ra offers the largest measured production cross section compared with both other reactions, whose cross sections are significantly lower.

As our studies revealed, if the barrier is situated below the maximum of the $4n$ channel of $E^* \approx 40$ MeV and hence the (B-Q)-value is low, strong Q-value effects occur. This effect affects the $4n$ channel to become the dominant channel and to provide a much larger production cross section than that of "hot" fusion reactions, because these are cut-off by the barrier. This cut is caused by the fusion probability which has not reached its maximum value.

If the barrier is situated at higher excitation energies ($B > E^*(4n)$), which is the case for "hot" fusion reactions, the Q-value effect is minor, the $4n$ channel is suppressed and only the asymmetry plays an important role and has a deep impact on the production cross section.

The results about the mechanism of fusion reactions and the impact of the (B-Q)-value and asymmetry on the production cross section, especially for the $5n$ channel need more statistics for a more detailed understanding.

In general, a reaction providing a low (B-Q)-value as well as large reaction asymmetry will provide largest cross sections, especially for the $4n$ channel. If the fusion probability of such a reaction is already saturated for the $4n$ channel, the production cross section will of course be much larger than that of the $5n$ channel, since one neutron less has to be evaporated to cool down the nucleus.

The conclusions of this thesis are extremely important, especially for the first synthesis of new elements (e.g. element 119 and 120). For synthesis up to element 118, doubly magic ^{48}Ca could be used as projectile with various actinide targets, providing relatively large production cross sections for SHE due to strong Q-value effects. ^{249}Bk and ^{249}Cf are the heaviest target materials which can be used in SHE synthesis experiments. Heavier targets made from Es or Fm isotopes can not be produced in sufficient quantities in breeding reactors. Hence, new projectile-target combinations have to be chosen to discover the next elements of the periodic table. This is very important, since the production cross sections decrease very strongly with increasing proton number of the CN and are expected to be of the order of some hundreds of fb or less, depending on the reaction. Such one event cross section limits can only be reached experimentally in experiments that last many months to more than one year. Hence, the optimal reaction with the largest expected cross section has to be chosen to have a chance to discover a new element. The most promising reactions with relevant reaction parameters are shown in Table 5.1 and Table 5.2.

Table 5.1: Comparison of fusion reactions leading to element 119

Beam	Target	CN	$Z_p \cdot Z_t$	(B-Q) [MeV]	fissility
^{45}Sc	^{249}Cf	^{294}119	2058	41.7	0.904
^{50}Ti	^{249}Bk	^{299}119	2134	32.4	0.911
^{51}V	^{248}Cm	^{299}119	2208	36.8	0.913
^{54}Cr	^{243}Am	^{297}119	2280	31.5	0.923
^{55}Mn	^{244}Pu	^{299}119	2350	37.7	0.922
^{58}Fe	^{237}Np	^{295}119	2418	29.9	0.934
^{59}Co	^{238}U	^{297}119	2484	36.7	0.933

Since the result of this thesis reveals the deep impact of the (B-Q)-value as well as

Table 5.2: Comparison of fusion reactions leading to element 120

Beam	Target	CN	$Z_p \cdot Z_t$	(B-Q) [MeV]	fissility
^{50}Ti	^{249}Cf	^{299}120	2156	31.7	0.919
^{51}V	^{249}Bk	^{300}120	2231	35.9	0.923
^{54}Cr	^{248}Cm	^{302}120	2304	33.0	0.926
^{55}Mn	^{243}Am	^{298}120	2375	34.5	0.934
^{58}Fe	^{244}Pu	^{302}120	2444	33.9	0.934
^{59}Co	^{237}Np	^{296}120	2511	32.9	0.945
^{64}Ni	^{238}U	^{302}120	2576	27.3	0.945

the reaction asymmetry, its very important to find a reaction which offers a low (B-Q)-value as well as a low $Z_p \cdot Z_t$-value. As can be seen from Table 5.1 and Table 5.2, for the synthesis of element 119, the reaction ^{50}Ti + ^{249}Bk should provide the largest production cross section. For the synthesis of element 120, the reaction ^{50}Ti + ^{249}Cf should be the most promising one.

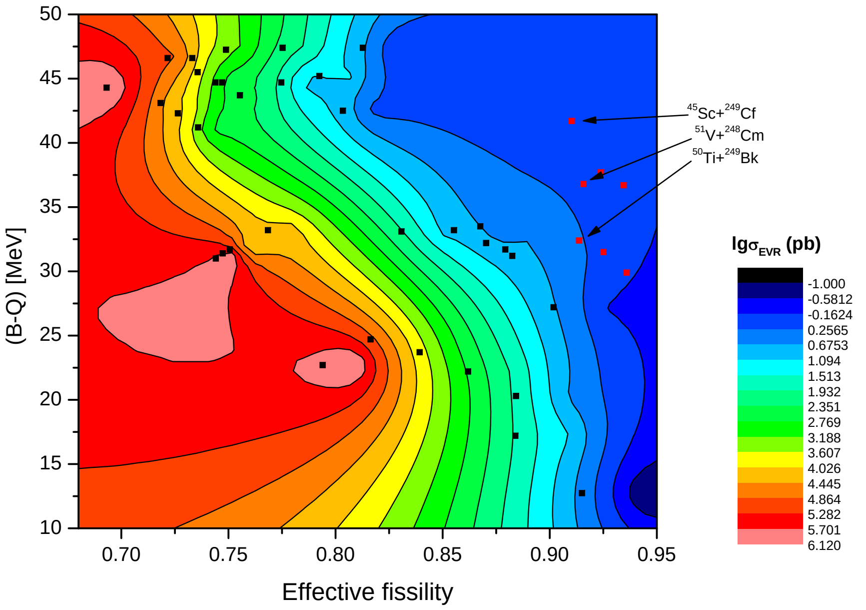

Figure 5.1: Contour plot showing the dependence between the EVR cross section from the fissility parameter and the (B-Q)-value concerning production of element 119.

To estimate the production cross section of a certain fusion reaction, a contour plot can be generated (Figure 5.1 and Figure 5.2), presenting experimental cross section values in dependence of the fissility (proportional to the asymmetry) and the (B-Q)-value for heavy nuclides (Z > 100) produced in complete fusion reactions. The calculated values of (B-Q) and the fissility for some reactions leading to element 119 and 120 are also shown and indicated by arrows. As can be seen, the "warm fusion" of heavy actinide targets with neutron-rich heavy ions are the most promising reactions towards the synthesis of heaviest elements.

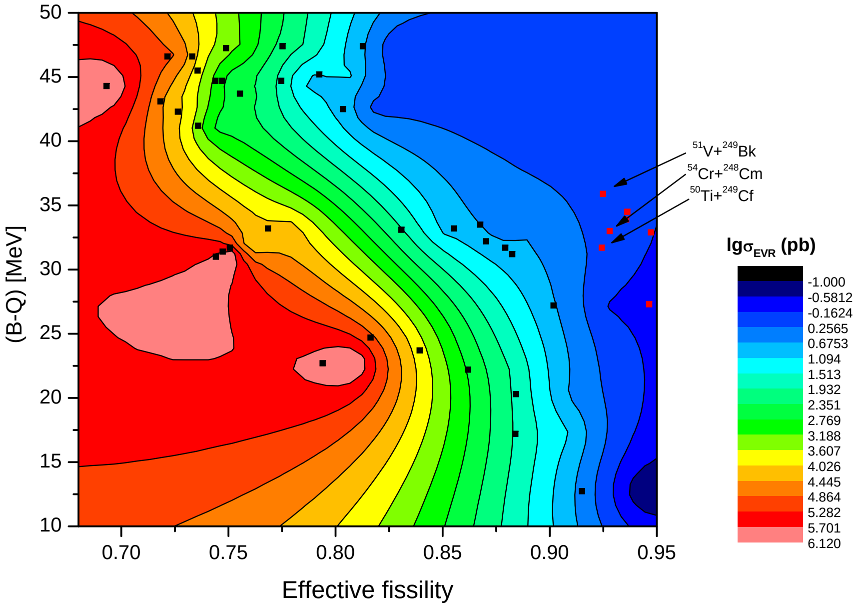

Figure 5.2: Contour plot showing the dependence between the EVR cross section from the fissility parameter and the (B-Q)-value concerning production of element 120.

As can also be seen from both plots the reactions ^{50}Ti + ^{249}Bk and ^{50}Ti + ^{249}Cf should provide largest production cross sections for the synthesis for element 119 and 120, respectively.

Bibliography

[1] Sigurd Hofmann. *On Beyond Uranium - Journey to the end of the Periodic Table*, volume 2 of *Science Spectra Book Series*. Taylor and Francis, London and New York, 2002. ISBN 0-415-28495-3.

[2] S. Cwiok, J. Dobaczewski, P. H. Heenen, P. Magierski, and W. Nazarewicz. Shell structure of the superheavy elements. *Nuclear Physics A*, 611(2-3):211–246, December 1996.

[3] W. D. Myers and W. J. Swiatecki. Nuclear properties according to the thomas-fermi model. *Nuclear Physics A*, 601(2):141–167, May 1996.

[4] A. Sobiczewski. Structure of heaviest nuclei. *Acta Physica Polonica B*, 29(9):2191, 1998.

[5] K. Rutz, M. Bender, T. Bürvenich, T. Schilling, P.-G. Reinhard, J. A. Maruhn, and W. Greiner. Superheavy nuclei in self-consistent nuclear calculations. *Phys. Rev. C*, 56(1):238–, July 1997.

[6] Zygmunt Patyk and Adam Sobiczewski. Ground-state properties of the heaviest nuclei analyzed in a multidimensional deformation space. *Nuclear Physics A*, 533(1):132–152, October 1991.

[7] Ch. E. Düllmann, W. Brüchle, R. Dressler, K. Eberhardt, B. Eichler, R. Eichler, H. W. Gäggeler, T. N. Ginter, F. Glaus, K. E. Gregorich, D. C. Hoffman, E. Jäger, D. T. Jost, U. W. Kirbach, D. M. Lee, H. Nitsche, J. B. Patin, V. Pershina, D. Piguet, Z. Qin, M. Schädel, B. Schausten, E. Schimpf, H.-J. Schott, S. Soverna, R. Sudowe, P. Thorle, S. N. Timokhin, N. Trautmann, A. Türler, A. Vahle, G. Wirth, A. B. Yakushev, and P. M. Zielinski. Chemical investigation of hassium (element 108). *Nature*, 418(6900):859–862, August 2002.

[8] Jan Dvořák. *Decay properties of nuclei close to $Z = 108$ and $N = 162$*. PhD thesis, Technische Universität München, 2006.

[9] Glenn T. Seaborg and Walter D. Loveland. *The Elements Beyond Uranium*. Wiley, New York, 1990.

[10] C. F. von Weizsäcker. Zur Theorie der Kernmassen. *Z. Phys. A*, 96(7):431 – 458, 07 1935.

[11] H. A. Bethe and R. F. Bacher. Nuclear Physics A. Stationary States of Nuclei. *Reviews of Modern Physics*, 8:82–229, April 1936.

[12] M. G. Mayer. Nuclear Configurations in the Spin-Orbit Coupling Model. I. Empirical Evidence. *Physical Review*, 78:16–21, April 1950.

[13] M. G. Mayer. Nuclear Configurations in the Spin-Orbit Coupling Model. II. Theoretical Considerations. *Physical Review*, 78:22–23, April 1950.

[14] M. G. Mayer. On Closed Shells in Nuclei. II. *Physical Review*, 75:1969–1970, June 1949.

[15] O. Haxel, J. H. Jensen, and H. E. Suess. On the "Magic Numbers" in Nuclear Structure. *Physical Review*, 75:1766–1766, June 1949.

[16] J. R. Nix. Calculation of fission barriers for heavy and superheavy nuclei. *Annual Review of Nuclear Science*, 22(1):65–120, 1972.

[17] P. Möller and J. R. Nix. In *Third International Atomic Energy Symposium on Physics and Chemistry of Fission*, volume 1, page 103. Rochester, New York, IAEA, Vienna, 1973. Paper SM-174/202.

[18] P. Möller, J.R. Nix, P. Armbruster, S. Hofmann, and G. Münzenberg. Single-particle enhancement of heavy-element production. *Zeitschrift für Physik A Hadrons and Nuclei*, 359(3):251–255, November 1997.

[19] V. M. Strutinsky. Shell effects in nuclear masses and deformation energies. *Nuclear Physics A*, 95(952):420–442, April 1967.

[20] V. M. Strutinsky. "shells" in deformed nuclei. *Nuclear Physics A*, 122(1):1–33, December 1968.

[21] Niels Bohr and John Archibald Wheeler. The mechanism of nuclear fission. *Phys. Rev.*, 56(5):426–, September 1939.

[22] Zygmunt Patyk, Adam Sobiczewski, Peter Armbruster, and Karl-Heinz Schmidt. Shell effects in the properties of the heaviest nuclei. *Nuclear Physics A*, 491(2):267–280, January 1989.

[23] Zygmunt Patyk, Janusz Skalski, Adam Sobiczewski, and Stefanl Cwiok. Potential energy and spontaneous-fission half-lives for heavy and superheavy nuclei. *Nuclear Physics A*, 502:591–600, October 1989.

[24] P. Armbruster. On the production of superheavy elements. *Annual Review of Nuclear and Particle Science*, 50(1):411–479, 2000.

[25] V. I. Zagrebaev, Y. Aritomo, M. G. Itkis, Yu. Ts. Oganessian, and M. Ohta. Synthesis of superheavy nuclei: How accurately can we describe it and calculate the cross sections? *Physical Review C (Nuclear Physics)*, 65(1):014607–, December 2001.

[26] V. I. Zagrebaev. Synthesis of superheavy nuclei: Nucleon collectivization as a mechanism for compound nucleus formation. *Physical Review C (Nuclear Physics)*, 64(3):034606–, August 2001.

[27] A. B. Yakushev. Chemical charaterization of element 108, hassium and synthesis of new hassium isotopes. Habilitation Thesis in the Field of Radiochemistry at the Department of Chemistry of the Technical University of Munich, 2009.

[28] R. Bass. Fusion of heavy nuclei in a classical model. *Nuclear Physics A*, 231(1):45–63, October 1974.

[29] W J Swiatecki. The dynamics of nuclear coalescence or reseparation. *Physica Scripta*, 24(1B):113–122, 1981.

[30] S. Bjørnholm and W. J. Swiatecki. Dynamical aspects of nucleus-nucleus collisions. *Nuclear Physics A*, 391(2):471 – 504, 1982.

[31] J. P. Blocki, H. Feldmeier, and W. J. Swiatecki. Dynamical hindrance to compound-nucleus formation in heavy-ion reactions. *Nuclear Physics A*, 459(1):145–172, October 1986.

[32] C. E. Aguiar, V. C. Barbosa, and R. Donangelo. Thermal fluctuations in heavy-ion fusion reactions : (ii). multidimensional models. *Nuclear Physics A*, 517(1):205 – 220, 1990.

[33] Y. Arimoto, T. Wada, M. Ohta, and Y. Abe. In Yu. Ts. Oganessian and V. I. Zagrebaev, editors, *Proceedings on Fusion Dynamics at the Extremes, Dubna 2000*, page 123. World Science, Singapore, 2001.

[34] Y. Arimoto. In *International Conference on Nuclear Physics at Border Lines*, page 8, Lipari (Messina), Italy, 2001.

[35] N. V. Antonenko, E. A. Cherepanov, A. K. Nasirov, V. P. Permjakov, and V. V. Volkov. Competition between complete fusion and quasi-fission in reactions between massive nuclei. the fusion barrier. *Physics Letters B*, 319(4):425 – 430, 1993.

[36] G. G. Adamian, N. V. Antonenko, W. Scheid, and V. V. Volkov. Treatment of competition between complete fusion and quasifission in collisions of heavy nuclei. *Nuclear Physics A*, 627(2):361 – 378, 1997.

[37] E. A. Cherepanov. In Yu. Ts. Oganessian and V. I. Zagrebaev, editors, *Proceedings on Fusion Dynamics at the Extremes, Dubna 2000*, page 186. World Science, Singapore, 2001.

[38] V. I. Zagrebaev. In Yu. Ts. Oganessian and V. I. Zagrebaev, editors, *Proceedings on Fusion Dynamics at the Extremes, Dubna 2000*, page 215. World Science, Singapore, 2001.

[39] A. V. Ignatyk. *Statistical Properties of Excited Atomic Nuclei*. Energoatomazidat, Moscow, 1983.

[40] K.E. Gregorich, T.N. Ginter, W. Loveland, D. Peterson, J.B. Patin, C.M. Folden, D.C. Hoffman, D.M. Lee, H. Nitsche, J.P. Omtvedt, L.A. Omtvedt, L. Stavsetra, R. Sudowe, P.A. Wilk, P.M. Zielinski, and K. Aleklett. Cross-section limits for the $^{208}\mathrm{Pb}(^{86}\mathrm{Kr}, n)^{293}118$ reaction. *The European Physical Journal A - Hadrons and Nuclei*, 18(4):633–638, December 2003.

[41] Valery Zagrebaev and Walter Greiner. Synthesis of superheavy nuclei: A search for new production reactions. *Physical Review C (Nuclear Physics)*, 78(3):034610, 2008.

[42] V. I. Zagrebaev. private communication.

[43] Z. H. Liu and Jing-Dong Bao. Q-value effects on the production of superheavy nuclei. *Physical Review C (Nuclear Physics)*, 74(5):057602, 2006.

[44] W. Reisdorf and M. Schädel. How well do we understand the synthesis of heavy elements by heavy-ion induced fusion? *Zeitschrift für Physik A Hadrons and Nuclei*, 343(1):47–57, March 1992.

[45] H. Esbensen. Fusion and zero-point motions. *Nuclear Physics A*, 352(1):147–156, January 1981.

[46] C. H. Dasso, S. Landowne, and A. Winther. Channel-coupling effects in heavy-ion fusion reactions. *Nuclear Physics A*, 405(2):381–396, August 1983.

[47] W. Reisdorf, F. P. Heßberger, K. D. Hildenbrand, S. Hofmann, G. Münzenberg, K. H. Schmidt, J. H. R. Schneider, W. F. W. Schneider, K. Sümmerer, G. Wirth, J. V. Kratz, and K. Schlitt. Fusion near the threshold: A comparative study of the systems $^{40}\mathrm{Ar} + {}^{112,116,122}\mathrm{Sn}$ and $^{40}\mathrm{Ar} + {}^{144,148,154}\mathrm{Sm}$. *Nuclear Physics A*, 438(1):212 – 252, 1985.

[48] S. Liran and N. Zeldes. A semiempirical shell-model formula. *Atomic Data and Nuclear Data Tables*, 17(5-6):431 – 441, 1976.

[49] Ch. E. Düllmann. private communication.

[50] Z. Patyk and A. Sobiczewski. Main deformed shells of heavy nuclei studied in a multidimensional deformation space. *Physics Letters B*, 256(3-4):307–310, March 1991.

[51] J. Dvořák, W. Brüchle, M. Chelnokov, R. Dressler, Ch. E. Düllmann, K. Eberhardt, V. Gorshkov, E. Jäger, R. Krücken, A. Kuznetsov, Y. Nagame, F. Nebel, Z. Novackova, Z. Qin, M. Schädel, B. Schausten, E. Schimpf, A. Semchenkov, P. Thorle, A. Türler, M. Wegrzecki, B. Wierczinski, A. Yakushev, and A. Yeremin. Doubly magic nucleus $^{270}_{108}\mathrm{Hs}_{162}$. *Physical Review Letters*, 97(24):242501, 2006.

[52] J. Dvořák, W. Brüchle, M. Chelnokov, Ch. E. Düllmann, Z. Dvorakova, K. Eberhardt, E. Jäger, R. Krücken, A. Kuznetsov, Y. Nagame, F. Nebel, K. Nishio, R. Perego, Z. Qin, M. Schädel, B. Schausten, E. Schimpf, R. Schuber, A. Semchenkov, P. Thorle, A. Türler, M. Wegrzecki, B. Wierczinski, A. Yakushev, and A. Yeremin. Observation of the 3n evaporation channel in the complete hot-fusion reaction $^{26}\mathrm{Mg} + {}^{248}\mathrm{Cm}$ leading to the new superheavy nuclide $^{271}\mathrm{Hs}$. *Phys. Rev. Lett.*, 100(13):132503–4, April 2008.

[53] M. Schädel. *The chemistry of the Superheavy Elements.* Kluwer Academic Publishers Dordrecht/Boston/London, 2003.

[54] R. Smolanczuk, J. Skalski, and A. Sobiczewski. Spontaneous-fission half-lives of deformed superheavy nuclei. *Phys. Rev. C*, 52(4):1871–, October 1995.

[55] P. Möller, J. R. Nix, W. D. Myers, and W. J. Swiatecki. Nuclear ground-state masses and deformations. *Atomic Data and Nuclear Data Tables*, 59(2):185–381, March 1995.

[56] A. Parkhomenko and A. Sobiczewski. Phenomenological formula for α-decay half-lives of heaviest nuclei. *Acta Physica Polonica B*, 36:3095, 2005.

[57] I. Muntian, Z. Patyk, and A. Sobiczewski. Calculated masses of heaviest nuclei. *Physics of Atomic Nuclei*, 66(6):1015, 2003.

[58] A. Sobiczewski. private communication.

[59] R. B. Firestone and V. S. Shirley. *Table of Isotopes, 2 Volume Set.* Table of Isotopes, 2 Volume Set, by Richard B. Firestone, Virginia S. Shirley (Editor), pp. 3168. ISBN 0-471-33056-6. Wiley-VCH , December 1998., December 1998.

[60] S. Hofmann, F.P. Heßberger, D. Ackermann, S. Antalic, P. Cagarda, S. Cwiok, B. Kindler, J. Kojouharova, B. Lommel, R. Mann, G. Münzenberg, A.G. Popeko, S. Saro, H.J. Schött, and A.V. Yeremin. The new isotope $^{270}110$ and its decay products ^{266}Hs and ^{262}Sg. *European Physical Journal A*, 1:5, 2001.

[61] F.P. Heßberger, S. Hofmann, V. Ninov, P. Armbruster, H. Folger, G. Münzenberg, H.J. Schött, A.G. Popeko, A.V. Yeremin, A.N. Andreyev, and S. Saro. Spontaneous fission and alpha-decay properties of neutron deficient isotopes $^{257-253}104$ and $^{258}106$. *Zeitschrift für Physik A Hadrons and Nuclei*, 359(4):415–425, December 1997.

[62] K. Nishio, S. Hofmann, F.P. Heßberger, D. Ackermann, S. Antalic, Y. Aritomo, V.F. Comas, Ch.E. Düllmann, A. Gorshkov, R. Graeger, K. Hagino, S. Heinz, J.A. Heredia, K. Hirose, H. Ikezoe, J. Khuyagbaatar, B. Kindler, I. Kojouharov, B. Lommel, R. Mann, S. Mitsuoka, Y. Nagame, I. Nishinaka, T. Ohtsuki, A.G. Popeko, S. Saro, M. Schädel, A. Türler, Y. Watanabe, A. Yakushev, and A.V. Yeremin. Study of nuclear orientation in the reaction $^{34}S + ^{238}U$ and decay properties of the new isotope ^{268}Hs. *Physical Review C (to be published)*, 2010.

[63] A. Türler, Ch.E. Düllmann, H.W. Gäggeler, U.W. Kirbach, A.B. Yakushev, M. Schädel, W. Bräuchle, R. Dressler, K. Eberhardt, B. Eichler, R. Eichler, T.N.

Ginter, F. Glaus, K.E. Gregorich, D.C. Hoffman, E. Jäger, D.T. Jost, D.M. Lee, H. Nitsche, J.B. Patin, V. Pershina, D. Piguet, Z. Qin, B. Schausten, E. Schimpf, H.-J. Schött, S. Soverna, R. Sudowe, P. Thörle, S.N. Timokhin, N. Trautmann, A. Vahle, G. Wirth, and P.M. Zielinski. On the decay properties of ^{269}Hs and indications for the new nuclide ^{270}Hs. *The European Physical Journal A - Hadrons and Nuclei*, 17(4):505–508, August 2003.

[64] S. Hofmann, F.P. Heßberger, D. Ackermann, G. Münzenberg, S. Antalic, P. Cagarda, B. Kindler, J. Kojouharova, M. Leino, B. Lommel, R. Mann, A.G. Popeko, S. Reshitko, S. aro, J. Uusitalo, and A.V. Yeremin. New results on elements 111 and 112. *The European Physical Journal A - Hadrons and Nuclei*, 14(2):147–157, June 2002.

[65] K. Morita, K. Morimoto, D. Kaji, T. Akiyama, S. Goto, H. Haba, E. Ideguchi, H. Koura, H. Kudo, T. Ohnishi, A. Ozawa, T. Suda, K. Sueki, H. Xu, T. Yamaguchi, A. Yoneda, A. Yoshida, and Y.-L. Zhao. Experiments on synthesis of isotope ^{277}112 by ^{208}Pb + ^{70}Zn reaction. *RIKEN Accel. Prog. Rep.*, 38:69, 2005.

[66] Ch. E. Düllmann and A. Türler. $^{248}\mathrm{Cm}(^{22}\mathrm{Ne}, xn)^{270-\mathrm{x}}\mathrm{Sg}$ reaction and the decay properties of ^{265}Sg reexamined. *Physical Review C (Nuclear Physics)*, 77(6):064320, 2008.

[67] K. E. Gregorich, J. M. Gates, Ch. E. Düllmann, R. Sudowe, S. L. Nelson, M. A. Garcia, I. Dragojevic, C. M. Folden III, S. H. Neumann, D. C. Hoffman, and H. Nitsche. New isotope ^{264}Sg and decay properties of $^{262-264}$Sg. *Physical Review C (Nuclear Physics)*, 74(4):044611, 2006.

[68] K. Nishio, S. Hofmann, F. Heßberger, D. Ackermann, S. Antalic, V. Comas, Z. Gan, S. Heinz, J. Heredia, H. Ikezoe, J. Khuyagbaatar, B. Kindler, I. Kojouharov, P. Kuusiniemi, B. Lommel, R. Mann, M. Mazzocco, S. Mitsuoka, Y. Nagame, T. Ohtsuki, A. Popeko, S. Saro, H. Schött, B. Sulignano, A. Svirikhin, K. Tsukada, K. Tsuruta, and A. Yeremin. Measurement of evaporation residue cross-sections of the reaction ^{30}Si + ^{238}U at subbarrier energies. *The European Physical Journal A - Hadrons and Nuclei*, 29(3):281–287, September 2006.

[69] J. Dvořák, W. Brüchle, Ch. E. Düllmann, Z. Dvorakova, K. Eberhardt, R. Eichler, E. Jäger, Y. Nagame, Z. Qin, M. Schädel, B. Schausten, E. Schimpf, R. Schuber, A. Semchenkov, P. Thörle, A. Türler, M. Wegrzecki, and A. Yakushev. Cross

section limits for the ^{248}Cm(^{25}Mg$, 4n - 5n)^{268,269}$Hs reactions. *Phys. Rev. C*, 79(3):037602, Mar 2009.

[70] M. Leino. Gas-filled separators - an overview. *Nuclear Instruments and Methods in Physics Research Section B: Beam Interactions with Materials and Atoms*, 204:129 – 137, 2003. 14th International Conference on Electromagnetic Isotope Separators and Techniques Related to their Applications.

[71] H.-D. Betz. Charge states and charge-changing cross sections of fast heavy ions penetrating through gaseous and solid media. *Rev. Mod. Phys.*, 44(3):465–539, Jul 1972.

[72] A. Semchenkov, W. Brüchle, E. Jäger, E. Schimpf, M. Schädel, C. Mühle, F. Klos, A. Türler, A. Yakushev, A. Belov, T. Belyakova, M. Kaparkova, V. Kukhtin, E. Lamzin, and S. Sytchevsky. The transactinide separator and chemistry apparatus (tasca) at gsi - optimization of ion-optical structures and magnet designs. *Nuclear Instruments and Methods in Physics Research Section B: Beam Interactions with Materials and Atoms*, 266(19-20):4153 – 4161, 2008. Proceedings of the XVth International Conference on Electromagnetic Isotope Separators and Techniques Related to their Applications.

[73] T. Enqvist, P. Heikkinen, H. Kettunen, P. Kuusiniemi, M. Leino, A. P. Leppnen, C. Scholey, and J. Uusitalo. The design of a new gas-filled separator at jyfl. *Nuclear Instruments and Methods in Physics Research Section B: Beam Interactions with Materials and Atoms*, 204:138 – 140, 2003. 14th International Conference on Electromagnetic Isotope Separators and Techniques Related to their Applications.

[74] K. Subotic, Yu. Ts. Oganessian, V. K. Utyonkov, Yu. V. Lobanov, F. Sh. Abdullin, A. N. Polyakov, Yu. S. Tsyganov, and O. V. Ivanov. Evaporation residue collection efficiencies and position spectra of the dubna gas-filled recoil separator. *Nuclear Instruments and Methods in Physics Research Section A: Accelerators, Spectrometers, Detectors and Associated Equipment*, 481(1-3):71–80, April 2002.

[75] B.L. Zhuikov, H. Kruz, and I. Zvara. Possibilities of chemical identification of short-lived element 108 isotopes. In *Abstract School-Seminar on Heavy Ion Physics 1985*, Report P7-86-322, page 26, JINR, Dubna, 1986.

[76] V.I. Chepigin, B.L. Zhuikov, G.M. Ter-Akopian, and I. Zvara. Search of alpha-active isotopes of element 108 in the reaction ^{249}Cf+^{22}Ne with fast chemical isola-

tion. In *Abstract School-Seminar on Heavy Ion Physics 1985*, Report P7-86-322, page 15. JINR, Dubna, 1986. in Russian.

[77] R. J. Dougan, K. J. Moody, E. K. Hulet, and G. R. Bethune. OSCAR: An apparatus for on-line gas phase separations. Lawrence Livermore National Laboratory, FY87 Annual Report ULAR 10062/87, 1987. pp. 417.

[78] E.K. Hulet, K.J. Moody, R.W. Lougheed, J. F. Wild, R. J. Dougan, and G. R. Bethune. Search for $^{272}109$ in a new region of stability. Lawrence Livermore National Laboratory, FY87 Annual Report ULAR 10062/87, 1987. pp. 49.

[79] C. E. Düllmann, B. Eichler, R. Eichler, H. W. Gäggeler, D. T. Jost, D. Piguet, and A. Türler. IVO, a device for In situ Volatilization and On-line detection of products from heavy ion reactions. *Nuclear Instruments and Methods in Physics Research A*, 479:631–639, March 2002.

[80] L. K. Koopal. *Manual of symbols and terminology for physicochemical quantities and units. Appendix II, Part I. International Edition.* 2001.

[81] Ch. E. Düllmann, B. Eichler, R. Eichler, H. W. Gäggeler, and A. Türler. On the stability and volatility of group 8 tetroxides MO_4 (M = ruthenium, osmium, and hassium (Z = 108)). *J. Phys. Chem. B*, 106:6679–6684, 2002.

[82] V. Pershina, T. Bastug, B. Fricke, and S. Varga. The electronic structure and properties of group 8 oxides mo_4, where m=ru, os, and element 108, hs. *J. Chem. Phys.*, 115(2):792–799, July 2001.

[83] André von Zweidorf, W. Brüchle, S. Bürger, H. Hummrich, Jens Volker Kratz, B. Kuczewski, G. Langrock, U. Rieth, M. Schädel, N. Trautmann, K. Tsukada, and N. Wiehl. Evidence for the formation of sodium hassate(viii). *Radiochimica Acta*, 92:855–861, 2004.

[84] Michael Bender, Paul-Henri Heenen, and P. G. Reinhard. Self-consistent mean-field models for nuclear structure. *Rev. Mod. Phys.*, 75:121–180, 2003.

[85] M.G. Itkis, A.A. Bogachev, I.M. Itkis, J. Kliman, G.N. Knyazheva, N.A. Kondratiev, E.M. Kozulin, L. Krupa, Yu.Ts. Oganessian, I.V. Pokrovsky, E.V. Prokhorova, and A.Ya. Rusanov. The processes of fusion-fission and quasi-fission of superheavy nuclei. *Nuclear Physics A*, 787(1-4):150 – 159, 2007. Proceedings of the Ninth International Conference on Nucleus-Nucleus Collisions - (NN2006).

[86] V. Ninov, K. E. Gregorich, and C. A. McGrath. Proceedings of the enam98. In *Exotic Nuclei and Atomic Masses*, page 704, Bellaire, Michigan, 1998. AIP Conf. Proc. 455.

[87] Yu.A. Lazarev, Yu.V. Lobanov, A.N. Mezentsev, Yu.Ts. Oganessian, V.G. Subbotin, V.K. Utyonkov, F.Sh. Abdullin, V.V. Bechterev, S. Iliev, I.V. Kolesov, A.N. Polyakov, I.M. Sedykh, I.V. Shirokovsky, A.M. Sukhov, Yu.S. Tsyganov, and V.E. Zhuchko. In *Proceedings of the International School-Seminar on Heavy Ion Physics, Dubna, Russia*, volume 2, page 497, JINR, Dubna, 1993,.

[88] I. J. Zvára. *The Inorganic Radiochemistry of Heavy Elements: Methods for Studying Gaseous Compounds*. Springer-Verlag, 2007.

[89] I. Zvára. Thermochromatographic method of separation of chemical elements in nuclear and radiochemistry. *Isotopenpraxis*, 26:251–258, 1990.

[90] U. W. Kirbach, C. M. Folden, III, T. N. Ginter, K. E. Gregorich, D. M. Lee, V. Ninov, J. P. Omtvedt, J. B. Patin, N. K. Seward, D. A. Strellis, R. Sudowe, A. Türler, P. A. Wilk, P. M. Zielinski, D. C. Hoffman, and H. Nitsche. The Cryo-Thermochromatographic Separator (CTS): A new rapid separation and α-detection system for on-line chemical studies of highly volatile osmium and hassium (Z=108) tetroxides. *Nuclear Instruments and Methods in Physics Research A*, 484:587–594, May 2002.

[91] K. Tinschert, R. Lang, J.Mäder, J. Robach, P. Spädtke, and A.Yakushev. Ion beam production from rare isotopes with gsi ecr ion sources. In *Proceedings of ECRIS08, Chicago, IL USA*, 2008.

[92] G. Audi, A. H. Wapstra, and C. Thibault. The Ame2003 atomic mass evaluation (II). Tables, graphs and references. *Nuclear Physics A*, 729:337–676, December 2003.

[93] R. Eichler, W. Brüchle, R. Buda, S. Bürger, R. Dressler, Ch. E. Düllmann, J. Dvořák, K. Eberhardt, B. Eichler, C. M. Folden III, H. W. Gäggeler, K. E. Gregorich, F. Haenssler, D. C. Hoffman, H. Hummrich, E. Jäger, J. V. Kratz, B. Kuczewski, D. Liebe, D. Nayak, H. Nitsche, D. Piguet, Z. Qin, U. Rieth, M. Schädel, B. Schausten, E. Schimpf, A. Semchenkov, S. Soverna, R. Sudowe, N. Trautmann, P. Thörle, A. Türler, B. Wierczinski, N. Wiehl, P. A. Wilk, G. Wirth, A. B. Yakushev, and A. von Zweidorf. Attempts to chemically investigate element 112. *Radiochimica Acta*, 94(4):181–191, 2006.

[94] M. Schädel. Chemie superschwerer elemente. *Angewandte Chemie*, 118:378, 2006.

[95] J. Runke and K. Eberhardt. private communication.

[96] I. Zvara. Simulation of Thermochromatographic Processes by the Monte Carlo Method. *Radiochimica Acta*, 38:95–101, 1985.

[97] Yu.Ts.Oganessian. private communication.

[98] James F. Ziegler. Srim-2003. *Nuclear Instruments and Methods in Physics Research Section B: Beam Interactions with Materials and Atoms*, 219-220:1027 – 1036, 2004. Proceedings of the Sixteenth International Conference on Ion Beam Analysis.

[99] S. Hofmann. Status and prospects of synthesizing superheavy elements. *The European Physical Journal A - Hadrons and Nuclei*, 15(1):195–200, September 2002.

[100] K. H. Schmidt, C. C. Sahm, K. Pielenz, and H. G. Clerc. Some remarks on the error analysis in the case of poor statistics. *Zeitschrift für Physik A Hadrons and Nuclei*, 316(1):19–26, February 1984.

[101] Experimental Unevaluated Nuclear Data List (XUNDL). Evaluated Nuclear Structure Data File (ENSDF). http://www.nndc.bnl.gov/ensdf.

[102] Yu. Ts. Oganessian, V. K. Utyonkov, Yu. V. Lobanov, F. Sh. Abdullin, A. N. Polyakov, R. N. Sagaidak, I. V. Shirokovsky, Yu. S. Tsyganov, A. A. Voinov, G. G. Gulbekian, S. L. Bogomolov, B. N. Gikal, A. N. Mezentsev, S. Iliev, V. G. Subbotin, A. M. Sukhov, K. Subotic, V. I. Zagrebaev, G. K. Vostokin, M. G. Itkis, K. J. Moody, J. B. Patin, D. A. Shaughnessy, M. A. Stoyer, N. J. Stoyer, P. A. Wilk, J. M. Kenneally, J. H. Landrum, J. F. Wild, and R. W. Lougheed. Synthesis of the isotopes of elements 118 and 116 in the ^{249}Cf and ^{245}Cm + ^{48}Ca fusion reactions. *Physical Review C (Nuclear Physics)*, 74(4):044602, 2006.

[103] K. Morita, K. Morimoto, D. Kaji, T. Akiyama, S. Goto, H. Haba, E. Ideguchi, K. Katori, H. Koura, H. Kudo, T. Ohnishi, A. Ozawa, T. Suda, K. Sueki, F. Tokanai, K. Yamaguchi, K. Yoneda, and A. Yoshida. Experiment on Synthesis of an Isotope ^{277}112 by ^{208}Pb+^{70}Zn Reaction. *Journal of the Physical Society of Japan*, 76(4):043201, April 2007.

[104] Yuri Oganessian. Heaviest nuclei from ^{48}Ca-induced reactions. *Journal of Physics G: Nuclear and Particle Physics*, 34(4):R165–R242, 2007.

[105] V. B. Zlokazov. *Nuclear Instruments and Methods in Physics Research*, 151:303, 1978.

[106] Yu. Ts. Oganessian, V. K. Utyonkov, Yu. V. Lobanov, F. Sh. Abdullin, A. N. Polyakov, I. V. Shirokovsky, Yu. S. Tsyganov, A. N. Mezentsev, S. Iliev, V. G. Subbotin, A. M. Sukhov, K. Subotic, O. V. Ivanov, A. N. Voinov, V. I. Zagrebaev, K. J. Moody, J. F. Wild, N. J. Stoyer, M. A. Stoyer, and R. W. Lougheed. Measurements of cross sections for the fusion-evaporation reactions ^{204,206,207,208}Pb+ ^{48}Ca and ^{207}Pb+ ^{34}S: Decay properties of the even-even nuclides ^{238}Cf and ^{250}No. *Phys. Rev. C*, 64(5):054606–, October 2001.

[107] K. Nishio, H. Ikezoe, Y. Nagame, M. Asai, K. Tsukada, S. Mitsuoka, K. Tsuruta, K. Satou, C. J. Lin, and T. Ohsawa. Evidence of complete fusion in the sub-barrier ^{16}O+^{238}U reaction. *Phys. Rev. Lett.*, 93(16):162701–, October 2004.

[108] K. Nishio, H. Ikezoe, S. Mitsuoka, I. Nishinaka, Y. Nagame, Y. Watanabe, T. Ohtsuki, K. Hirose, and S. Hofmann. Effects of nuclear orientation on the mass distribution of fission fragments in the reaction of ^{36}S + ^{238}U. *Physical Review C (Nuclear Physics)*, 77(6):064607, 2008.

[109] S. P. Tretyakova, A. A. Ogloblin, R. N. Sagaidak, S. V. Khlebnikov, and W. Trzaska. Study of nucleus-nucleus potential by combined measurement of deep subbarrier fusion and cluster decay. *Nuclear Physics A*, 734(Supplement 1):E33–E36, April 2004.

[110] V. Yu. Denisov and S. Hofmann. Formation of superheavy elements in cold fusion reactions. *Physical Review C (Nuclear Physics)*, 61(3):034606–, February 2000.

[111] B. Kadkhodayan, A. Türler, K. E. Gregorich, P. A. Baisden, K. R. Czerwinski, B. Eichler, H. W. Gäggeler, T. M. Hamilton, D. T. Jost, C. D. Kacher, A. Kovacs, S. A. Kreek, M. R. Lane, M. F. Mohar, M. P. Neu, N. J. Stoyer, E. R. Sylwester, D. M. Lee, M. J. Nurmia, G. T. Seaborg, and D. C. Hoffman. On-line gas chromatographic studies of chlorides of rutherfordium and homologs Zr and Hf. *Radiochimica Acta*, 72:169, 1996.

[112] Albert Ghiorso, Matti Nurmia, Kari Eskola, James Harris, and Pirkko Eskola. New element hahnium, atomic number 105. *Phys. Rev. Lett.*, 24(26):1498–, June 1970.

List of Figures

List of Tables